I. CALCULATION OF SOL AND DIVERTOR PLASMA PROPERTIES

W. M. Stacey, Georgia Tech

Abstract

A complex variety of interacting phenomena determine the properties of the plasma in the scrape-off layer (SOL) and divertor of a tokamak[1]. These phenomena have been modeled in, two-dimensional plasma edge codes[2,3], which provide important insights into the physics of the SOL and divertor regions, but which are computationally intensive. In order to provide the means for routine analyses of SOL and divertor plasma properties, a computationally tractable model for the calculation of ion and impurity densities, temperature, currents, particle flows and electric fields along the separatrix in the divertor and scrape-off layer of tokamak plasmas has been developed. This model is described and applied to calculate the effects of particle drifts and the direction of the toroidal magnetic field on these calculated quantities. Several recently observed experimental phenomena—double reversal of the parallel ion velocity in the SOL[4], enhanced core penetration of argon injected into the divertor when the grad-B ion drift is into rather than away from the divertor[5]—and other interesting phenomena, such as the structure of the parallel current flowing in the SOL and the reversal of the sign of the electrostatic potential in the SOL when the toroidal field direction is reversed, are predicted.

A. Calculation Model

Geometrical model

The plasma outside the separatrix is modeled as "stack" of 2D strips, or "ribbons", that spiral about the core plasma (q times between X-points) following the magnetic field lines from the inner to the outer divertor target plate. A poloidal projection of this geometry is shown in Fig. 1. Non-uniformities in the magnetic geometry are represented by particle "drifts" to account for the effects of field gradients and curvature while retaining a simple computational geometry. The parameter ξ designates the distance along the field lines from the inner ($\xi = \xi_{in}$) to the outer ($\xi = \xi_{out}$) divertor targets.

Radial transport

The 2D transport problem in this strip is reduced to 1D by writing the divergence of the particle and heat fluxes as, e.g. for the particle flux $\nabla \mathbf{g}\Gamma = d\Gamma/d\xi + d\Gamma/dr$ and approximating the radial term by following experiment observation to assume that the density (and temperature) exponentially attenuate radially outward from the separatrix, $n = n_{sep}\exp\left(-r/\Delta_n\right)$ in the SOL. Requiring continuity across the separatrix of the ion particle flux $\Gamma_\perp^{sep}$ from the core into the SOL with a diffusive radial particle flux in the SOL $\Gamma_r = -D_\perp\, dn/dr$ identifies $\Delta_n = n_{sep}D_\perp/\Gamma_\perp^{sep}$. At the outer edge of the SOL, which is taken as a distance $\varepsilon\Delta_n$ outside the separatrix, the radially outward ion flux lost from the SOL plasma is $\Gamma_\perp^{sol} = D_\perp\Delta_n^{-1}n_{sep}e^{-\varepsilon}$. This leads to an

approximation $d\Gamma/dr \approx \left(\Gamma_{\perp}^{sol} - \Gamma_{\perp}^{sep}\right)/\Delta_n = -\left(\Gamma_{\perp}^{sep}/\Delta_n\right)\left(1-e^{-\varepsilon}\right) \equiv -\Gamma_{\perp}/\Delta_n$ for the radial contribution to the divergence of the particle flux. In this work, $\varepsilon = 1$ is used in the SOL (between X-points) and $\varepsilon = 3$ is used in the divertor channels to reflect the expansion of field line separation.

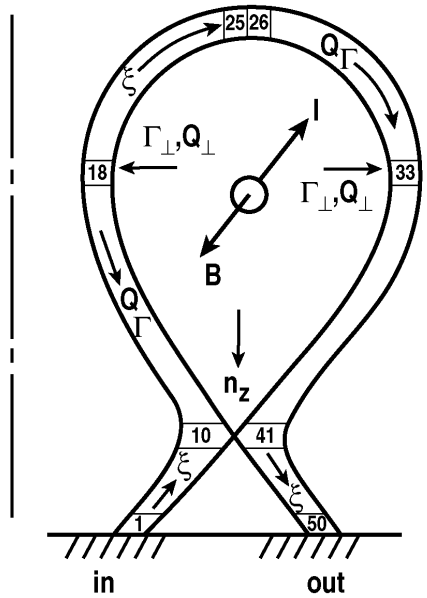

Figure 1 Geometric Model

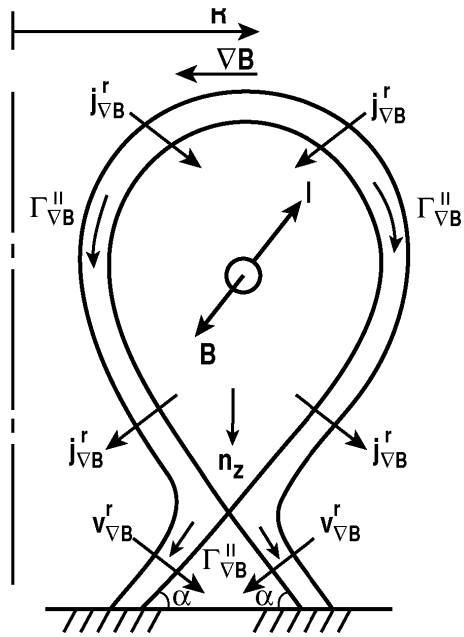

Figure 2 GradB Drifts

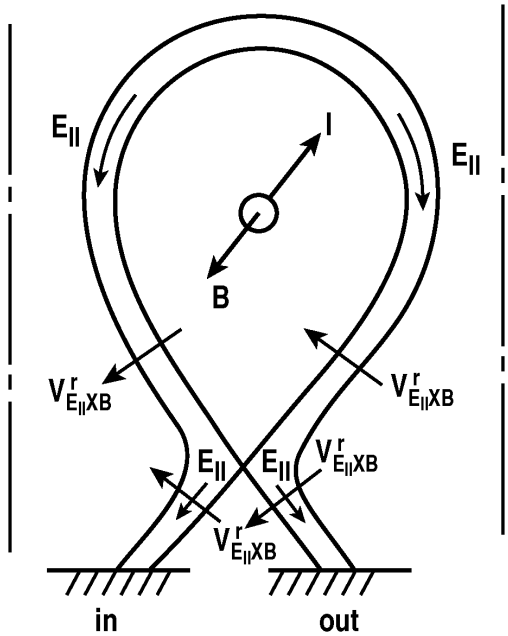

Figure 3 Radial ExB Drifts

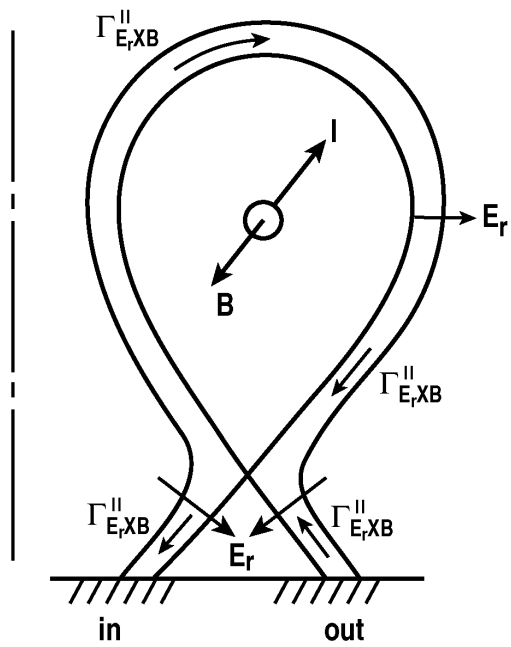

Figure 4 Parallel ExB Drifts

A similar argument can be used to approximate the radial component of the divergence of the heat flux, Q. When it is further assumed that parallel heat flux is dominated by electron heat conduction, $Q \approx \kappa_{\mathrm{P}} dT/d\xi = \kappa_0 T^{5/2}\, dT/d\xi$, the resulting approximation of radial transport is $dQ/dr \approx -\left(Q_\perp^{sep}/\Delta_E\right)\left(1-e^{\varepsilon}\right) \equiv -Q_\perp/\Delta_E$, where $\Delta_E = 2\chi_\perp n_{sep} T_{sep}/7Q_\perp^{sep}$, with $Q_\perp^{sep}$ representing the heat flux from the core flowing across the separatrix into the SOL. In the divertor channel only the transport loss term $-nT\chi_\perp/\Delta_E^2$ is present.

Temperature, density and flow distributions

The parallel energy balance equation solved for the heat flux Q in the SOL and divertor in a strip running from the inner divertor target plate around the plasma in a clockwise positive direction to the outer diver plate, as shown in Fig. 1, is

$$\begin{aligned}\frac{dQ}{d\xi} &= \frac{Q_\perp}{\Delta_E} - n_z n_e L_z - E_{ion} n_e n_o < \sigma\upsilon >_{ion} + f I_{ion} n_i n_e < \sigma\upsilon >_{rec} - \frac{3}{2} n_i n_o^c < \sigma\upsilon >_{cxel} \\ &+ j_{\mathrm{P}} \mathrm{E}_{\mathrm{P}} \equiv \frac{Q_\perp}{\Delta_E} - P_{rad} - P_{at} + P_\Omega\end{aligned} \tag{1}$$

where $Q_\perp$ is the perpendicular heat flux across the separatrix into the SOL (reduced by the radial transport heat loss), the second term represents impurity radiation (and bremsstrahlung) cooling, and the last three atomic physics terms represent ionization cooling, recombination heating, and charge-exchange plus elastic scattering cooling of the plasma. The sheath boundary conditions specify a heat flux into the inner and outer divertor plates

$$Q_{in} = -n_{in} c_{s,in} T_{in} \gamma_{in}\ ,\ Q_{out} = n_{out} c_{s,out} T_{out} \gamma_{out} \tag{2}$$

where

$$\gamma = \frac{2T_i}{T_e} + \frac{2}{1-\delta} + \frac{1}{2}\ln\left(\frac{(1-\delta)\, m_i/m_e}{2\pi\left(1+T_i/T_e\right)}\right) \tag{3}$$

is the sheath coefficient and δ is the secondary electron emission coefficient.

The parallel particle balance equation is

$$\frac{d\Gamma}{d\xi} = \frac{\Gamma_\perp}{\Delta_n} + n_e\left(n_o < \sigma\upsilon >_{ion} - n_i < \sigma\upsilon >_{rec}\right) \equiv \frac{\Gamma_\perp}{\Delta_n} + n_e\left(\nu_{ion} - \nu_{rec}\right) \tag{4}$$

where $\Gamma_\perp$ is the perpendicular particle flux from the core across the separatrix into the SOL (reduced by the radial particle loss) and "ion" and "rec" refer to ionization and recombination. The sheath boundary conditions specify that the particle fluxes into the target plates are

$$\Gamma_{in} = -n_{in} c_{s,in}\ ,\ \Gamma_{out} = n_{out} c_{s,out} \tag{5}$$

where c_s is the sound speed. In both Eqs. (2) and (5), the minus sign indicates that the flux is into the plate at the inner divertor target in the negative sense of the parallel coordinate ξ. These incident ions are recycled as neutral atoms and molecules, with the latter being dissociated immediately and transported as low energy atoms until they have a charge-exchange or elastic scattering collision, upon which they are combined with the higher energy reflected neutrals and transported throughout the divertor and SOL and inward across the separatrix.

Since both the particle and heat fluxes have inward flowing boundary conditions at both the inner and outer target plates, there must be stagnation points (not necessarily the same) in the particle and heat flows somewhere in the SOL (or divertor). Integrating Eq. (1) from the stagnation heat flux point ($Q_{stag} = 0$) to either target plate and using the boundary condition of Eq. (2) and integrating Eq. (4) from the particle flux stagnation point ($\Gamma = 0$) to either target plate and using the boundary condition of Eq. (5) then yields, for each target, a pair of equations which can be solved for the temperature just in front of the target plate

$$T_{out} = \frac{\int_{\xi_{stagQ}}^{\xi_{out}} (\frac{Q_\perp}{\Delta_E} - P_{rad} - P_{at}) d\xi}{\gamma_{out} \int_{\xi_{stag\Gamma}}^{\xi_{out}} (\frac{\Gamma_\perp}{\Delta_n} + n_e (\nu_{ion} - \nu_{rec})) d\xi}, \; T_{in} = \frac{\int_{\xi_{stagQ}}^{\xi_{in}} (\frac{Q_\perp}{\Delta_E} - P_{rad} - P_{at}) d\xi}{\gamma_{in} \int_{\xi_{stag\Gamma}}^{\xi_{in}} (\frac{\Gamma_\perp}{\Delta_n} + n_e (\nu_{ion} - \nu_{rec})) d\xi} \tag{6}$$

and for the density just in front of the target plates

$$n_{out} = \frac{\int_{\xi_{stag\Gamma}}^{\xi_{out}} (\frac{\Gamma_\perp}{\Delta_n} + n_e (\nu_{ion} - \nu_{rec})) d\xi}{\sqrt{\frac{2T_{out}}{m}}}, \; n_{in} = \frac{\int_{\xi_{stag\Gamma}}^{\xi_{in}} (\frac{\Gamma_\perp}{\Delta_n} + n_e (\nu_{ion} - \nu_{rec})) d\xi}{\sqrt{\frac{2T_{in}}{m}}} \tag{7}$$

These conditions are used in converging the iterative solution.

Solving Eqs. (1) and (2) for

$$Q(\xi) = -n_{in} c_{s,in} T_{in} \gamma_{in} + \int_{\xi_{in}}^{\xi} \left(\frac{Q_\perp}{\Delta_E} - P_{rad} - P_{at} \right) d\xi' \tag{8}$$

and assuming that parallel heat transport is dominated by classical electron heat conduction $Q(\xi) \approx q(\xi) = -\kappa_0 T^{5/2} dT/d\xi = -\frac{2}{7} \kappa_0 \, dT^{7/2}/d\xi$ leads to a solution for the temperature distribution in terms of the heat flux calculated from Eq. (8)

$$T^{7/2}(\xi) = T_{in}^{7/2} - \frac{7}{2\kappa_0} \int_{\xi_{in}}^{\xi} Q(\xi') d\xi' = T_{in}^{7/2} - \frac{7}{2\kappa_0} \int_{\xi_{in}}^{\xi} \left[-n_{in} c_{s,in} T_{in} \gamma_{in} + \int_{\xi_{in}}^{\xi'} \left(\frac{Q_\perp}{\Delta_E} - P_{rad} - P_{at} \right) d\xi'' \right] d\xi' \tag{9}$$

The parallel momentum balance equation can be written, neglecting viscosity, as

$$\frac{dM}{d\xi} \equiv \frac{d}{d\xi}\left(2p + nm\upsilon^2\right) = -m(\nu_{cxel} + \nu_{ion})\Gamma \equiv -m\nu_{mom}\Gamma \tag{10}$$

and integrated to solve for

$$M(\xi) = M(\xi_{in}) - \int_{\xi_{in}}^{\xi} m\nu_{mom}(\xi')\Gamma(\xi')d\xi' = 4n_{in}T_{in} - \int_{\xi_{in}}^{\xi} m\nu_{mom}(\xi')\Gamma(\xi')d\xi' \tag{11}$$

$M(\xi)$ can then be equated to $\left(2p + nm\upsilon^2\right)$ to obtain a quadratic equation in $n(\xi)$

$$\left(2p(\xi) + n(\xi)m\upsilon^2(\xi)\right) \equiv \left(2n(\xi)T(\xi) + m\Gamma^2(\xi)/n(\xi)\right) = M(\xi) \tag{12}$$

which yields a solution for the plasma ion density

$$n(\xi) = \frac{M(\xi)}{4T(\xi)}\left[1 \pm \sqrt{1 - 8mT(\xi)\Gamma^2(\xi)/M^2(\xi)}\right] \tag{13}$$

that can be used in the definition of Γ to obtain the plasma flow velocity

$$\upsilon(\xi) = \Gamma(\xi)/n(\xi) \tag{14}$$

The sheath boundary condition on the parallel flow velocity is

$$\upsilon(\xi_{in}) = -c_{s,in} \equiv -\sqrt{\frac{2T_{in}}{m}},\ \upsilon(\xi_{out}) = c_{s,out} \equiv \sqrt{\frac{2T_{out}}{m}} \tag{15}$$

In all calculations to date, the larger value obtained using the + sign in Eq. (13) has been of the magnitude observed in experiment, but the smaller value has not been physically unreasonable, perhaps implying the existence of a lower density divertor regime.

Equation (10) can be integrated from the inner divertor target plate to the outer divertor target plate to obtain

$$4n_{out}T_{out} - 4n_{in}T_{in} = -\int_{\xi_{in}}^{\xi_{out}} m\Gamma(\xi)\nu_{mom}(\xi)d\xi \tag{16}$$

demonstrating that a difference in pressure at the two divertor plates requires momentum dissipation (by atomic physics processes in this development) in the plasma flow between the two target plates. Equation (10) can also be integrated from the flow stagnation point to either

divertor plate to obtain a relation between for the pressure at the stagnation point and the pressure in front of the divertor target plate

$$\left(nT\right)_{stag\Gamma} = 2n_{in}T_{in} + \frac{1}{2}\int_{\xi_{stag\Gamma}}^{\xi_{in}} m\Gamma\left(\xi\right)v_{mom}\left(\xi\right)d\xi = 2n_{out}T_{out} + \frac{1}{2}\int_{\xi_{stag\Gamma}}^{\xi_{out}} m\Gamma\left(\xi\right)v_{mom}\left(\xi\right)d\xi \qquad (17)$$

The well-known "2-point" SOL-divertor model consists of the set of Eqs. (6) and (7) for the temperature and the density at the divertor target plus Eqs. (9) evaluated at the flow stagnation point and Eq.(17) for the temperature and density at the flow stagnation point.

Electrostatic potential

The electrostatic potential satisfies the electron parallel momentum balance equation

$$\frac{d\phi}{d\xi} = \frac{0.71}{e}\frac{dT}{d\xi} + \frac{1}{ne}\frac{dp}{d\xi} - \frac{j_{\mathrm{P}}}{\sigma_{\mathrm{P}}} \qquad (18)$$

which can be integrated to obtain

$$\phi\left(\xi\right) = \phi_{in} + \frac{1.71}{e}\left[T\left(\xi\right) - T_{in}\right] + \int_{\xi_{in}}^{\xi}\frac{T\left(\xi'\right)}{en\left(\xi'\right)}\frac{dn\left(\xi'\right)}{d\xi'}d\xi' - \int_{\xi_{in}}^{\xi}\frac{j_{\mathrm{P}}\left(\xi'\right)}{\sigma_{\mathrm{P}}\left(\xi'\right)}d\xi' \qquad (19)$$

where the potential just in front of the target plate is given by the current-potential sheath relation between the potential just in front of the plate $\left(\phi_{in,out}\right)$ and the current $\left(j_{pl}^{in,out}\right)$ into the plate

$$\phi_{in} = -\frac{T_{in}}{e}\ln\left[\frac{\sqrt{m_i/\pi m_e}\left(1-\delta\right)}{1 - j_{pl}^{in}/n_{in}ec_{si,in}}\right],\ \phi_{out} = -\frac{T_{out}}{e}\ln\left[\frac{\sqrt{m_i/\pi m_e}\left(1-\delta\right)}{1 - j_{pl}^{out}/n_{out}ec_{si,out}}\right] \qquad (20)$$

where $\sigma_{\mathrm{P}} = 2n_e e^2\tau_e/m_e,\ \tau_e = 3\sqrt{m_e}T^{3/2}/4\sqrt{2\pi}n_e\ln\Lambda e^4$.

Parallel current

The net current density into the target plates is given by the sum of the ion current density nec_{si} and the electron current density, $\frac{1}{4}n\left(-e\right)\bar{c}_e e^{e\phi/T}$ for a Maxwellian distribution,

$$j_{pl}^{in} = ne\left[c_{si} - \frac{1}{4}\bar{c}_e e^{e\phi/T_e}\right] \qquad (21)$$

where $\bar{c}_e = \left(8T_e/\pi m_e\right)^{1/2}$ is the average electron speed for a Maxwellian distribution.

The current density must be divergence-free

$$\nabla \mathrm{g}\mathbf{j} \equiv \frac{dj_{\mathrm{P}}}{d\xi} + \frac{dj_{\perp}}{d\mathrm{l}_{\perp}} + \frac{dj_r}{dr} = 0 \tag{22}$$

which may be solved for

$$j_{\mathrm{P}}(\xi) = -j_{pl}^{in} - \int_{\xi_{in}}^{\xi} \left[\frac{dj_{\perp}}{d\mathrm{l}_{\perp}} + \frac{dj_r}{dr} \right] d\xi' \tag{23}$$

The minus sign in front of the first term on the right results from the fact that Eq.(21) specifies the current into the inner divertor plate, while the positive sense of the current in this model is out of the inner divertor plate (but into the outer divertor plate); i.e. $j_{\mathrm{P}}(\xi_{in}) = -j_{pl}^{in}$.

These cross-field currents are driven by gradB and curvature drifts, as discussed in the following section. They are not driven by ExB drifts, which are the same for ions and electrons and hence do not produce currents, nor by diamagnetic currents which are almost divergence-free. Cross-field currents also may be driven by cross-field transport, viscosity and other mechanisms that have different effects on ions and electrons, but these mechanisms have been found[9,10] to be smaller and are not considered at present.

Grad-B and curvature drifts

The grad-B and curvature drifts are

$$\begin{aligned} &\upsilon_{\nabla B} = \frac{T}{e}\frac{\mathbf{B}\times\nabla B}{B^3} \approx \frac{T}{eRB}\mathbf{n}_z, \ \upsilon_c = -\frac{m\upsilon_{\mathrm{P}}^2}{e}\frac{\mathbf{B}\times\mathbf{R}}{B^2R^2} \approx \frac{m\upsilon_{\mathrm{P}}^2}{eRB}\mathbf{n}_z, \\ &\upsilon_B \equiv \upsilon_{\nabla B} + \upsilon_c \approx \frac{3T}{eRB}\mathbf{n}_z \end{aligned} \tag{24}$$

where $\mathbf{n}_z$ is a unit vector in the vertical direction, up or down depending on the direction of **B,** and $\upsilon_{\mathrm{P}} \approx \upsilon_{th}$. The drifts are in opposite directions for ions and electrons because of the charge sign difference, producing a current

$$\mathbf{j}_B = 2ne\boldsymbol{\upsilon}_B \approx \frac{6nT}{BR}\mathbf{n}_z \tag{25}$$

At this point, a specific current and magnetic field configuration is adopted, as shown in Figs. 1-4. For this configuration, the vertical unit vector $\mathbf{n}_z$ is directed downward. Thus, the radial drift currents are radially inward from the SOL into the core in the upper hemisphere $(0 \le \theta \le \pi)$ and radially outward from the core into the SOL in the lower hemisphere $(\pi \le \theta \le 2\pi)$, as indicated in Fig. 2.

The ion grad-B and curvature drifts also produce a parallel particle drift

$$\Gamma^{\mathrm{P}}_{\nabla B} = \left(\mathbf{n}_{\mathrm{P}} \cdot \mathbf{n}_z\right)\Gamma^{z}_{\nabla B} = \left(\frac{B_\theta}{B}\cos\theta\right)\frac{3nT}{eBR} \tag{26}$$

which is downward in both the inner and outer SOLs and divertors, as indicated in Fig. 2. Here, the angle θ is with respect to the outboard mid-plane. In the divertor, $\cos\theta$ is replaced by $\sin\alpha$, where α is the angle of incidence with respect to the horizontal of the separatrix, as illustrated in Fig. 2.

Using Eq. (25) to evaluate the radial drift current in Eq. (23) and adding the poloidal drift current from Eq. (26) provides an equation for the resulting parallel current in the SOL as a result of the divergence of the radial grad-B and curvature drift currents plus the parallel drift current

$$j_{\mathrm{P}}(\xi) = j_{\mathrm{P}}(\xi_{in}) + \int_{\xi_{in}}^{\xi}\left[\frac{6n(\xi')T(\xi')\left[\Delta_n^{-1}+\Delta_T^{-1}\right]}{RB}\left(\mathbf{n}_r \cdot \mathbf{n}_z\right)\right]d\xi' + 2e\Gamma^{\mathrm{P}}_{\nabla B} \equiv j_{\mathrm{P}}(\xi_{in}) + \Delta j_{\nabla B}(\xi) \tag{27}$$

The radial gradient scale lengths of temperature and density are defined in terms of the radial transport coefficients in the SOL $\Delta_n = n_{sep}D_\perp / \Gamma_\perp^{sep}$, $\Delta_T = n_{sep}T_{sep}\chi_\perp / Q_\perp^{sep}$, or they may be taken from experiment.

Solution for currents and potentials at target plates

Once the densities and temperatures are determined at the inner and outer divertor target plates (by solving Eqs. (1)-(17) in an iterative loop), Eqs.(19)-(27) can be solved for the electrostatic potentials and currents at the target plates. The current at the outer target can be evaluated from Eq. (27). Note that the integral of all the radial currents flowing from the core into the SOL plus all the radial currents flowing from the SOL into the core must vanish to maintain a neutral core plasma. The radial currents due to grad-B and curvature drifts are represented by the second term in Eq. (27), which will not vanish in general; i.e. other radial currents are needed. It is intended to include other radial currents in a future version of this model, but for now an 'ambipolarity' condition is imposed by adding or subtracting a constant to the term in square brackets in Eq. (27) that will cause the integral to vanish, in order to represent these other radial currents (which in effect represents the other radial currents as being distributed uniformly over the SOL). This 'ambipolarity-constrained' current integral is represented by $\Delta \$j_{\nabla B}(\xi)$. With this representation, Eq. (27) yields a relation between the currents into the plates at the inner and outer divertor targets

$$j_{pl}^{out} \equiv j_{\mathrm{P}}(\xi_{out}) = j_{\mathrm{P}}(\xi_{in}) + 2ne\Gamma^{\mathrm{P}}_{\nabla B}(\xi_{out}) = -j_{pl}^{in} + 2ne\Gamma^{\mathrm{P}}_{\nabla B}(\xi_{out}) \tag{28}$$

Equation (19) yields a relation between the potential just in front of the inner and outer plates

$$\phi_{out} = \phi_{in} + \frac{1.71}{e}\left[T_{out} - T_{in}\right] + \int_{\xi_{in}}^{\xi_{out}} \frac{T(\xi')}{en(\xi')}\frac{dn(\xi')}{d\xi'}d\xi' - \int_{\xi_{in}}^{\xi_{out}} \frac{\left[j_{\mathrm{P}}(\xi_{in}) + \Delta \$j_{\nabla B}(\xi')\right]}{\sigma_{\mathrm{P}}(\xi')}d\xi' \tag{29}$$

Using Eqs. (20) with $j_{pl}^{in} = -j_{\mathrm{P}}\left(\xi_{in}\right)$ and j_{pl}^{out} given by Eq. (28) in Eq. (29) yields an equation that determines $j_{\mathrm{P}}\left(\xi_{in}\right)$. Note that although the integral of the radial currents over the SOL must vanish, the current integral in Eq. (29) is weighted by $1/\sigma_{\mathrm{P}}$: $1/T^{3/2}$ and extends also over the divertor plasmas. This equation displays the well known result that the current in the SOL is driven by differences in potentials and temperatures at the target plates and by drifts due to the non-uniformity and curvature of the magnetic field (and other causes).

The above development has implicitly assumed that the target plates are at zero potential. If the plates are biased with respect to ground, then $\phi_{in,out} \Rightarrow \phi_{in,out} + \phi_{in,out}^{bias}$ in the above equations.

ExB drifts

Although ExB drifts do not produce currents, they do produce particle flows. The parallel variation of the electrostatic potential produces a parallel electric field and a corresponding radial ExB drift.

$$E_{\mathrm{P}} = -\left(\frac{d\phi}{d\xi}\right),\ \upsilon_{E_{\mathrm{P}}xB}^{r} = \frac{\mathbf{E}_{\mathrm{P}} \times \mathbf{B}}{B^2} = \frac{-\dfrac{d\phi}{d\xi}}{B} \tag{30}$$

directed as illustrated in Fig. 3 for the case in which the potential is negative in front of both target plates and increases to a maximum positive value at some point towards the top of the plasma in this model.

The "radial" *ExB* flows from the outboard divertor channel into the private flux region and from the private flux region into the inboard divertor channel will transfer ions from the outboard divertor channel across the private flux region beneath the plasma to the inboard divertor channel[13] .

The "radial drift" loss or gain of ions from both the SOL and the divertor channels can be represented by an *ExB* loss frequency

$$\nu_{E_{\mathrm{P}}xB}\left(\xi\right) = \frac{\upsilon_{E_{\mathrm{P}}xB}^{r}\left(\xi\right)}{\varepsilon \Delta_n} \tag{31}$$

where Δ_n is an estimate of the "radial width" of the SOL calculated as discussed for Eq. (6) and $\varepsilon \approx 3$ is a flux surface expansion factor taking into account the widening of the SOL into the divertor channel. Assuming that some fraction f_{ExB} of the ions lost into the private flux region from the outboard divertor channel flow into the inboard divertor channel, the source density of ions to the inboard divertor channel may be represented

$$S_{E_{\mathrm{P}}xB}^{in} = \frac{f_{ExB} \int_{\xi_{out}}^{\xi_{Xout}} \nu_{E_{\mathrm{P}}xB}(\xi) n(\xi) d\xi}{\int_{\xi_{in}}^{\xi_{Xin}} d\xi} \tag{32}$$

where $\xi_{Xout,in}$ denotes the location of the X-point in the outer SOL-divertor.

The particle balance Eq. (4) in the divertor channels now becomes

$$\frac{d\Gamma}{d\xi} = \frac{\Gamma_{\perp}}{\Delta_n} + n_e\left(\nu_{ion} - \nu_{rec}\right) + n_i(\nu_{E_{\mathrm{P}}xB} + \nu_B) + S_{E_{\mathrm{P}}xB}^{in} \tag{33}$$

where the source term $S_{E_{\mathrm{P}}xB}^{in}$ is only present in the inboard divertor channel, for the field configuration shown in Figs. 1-4. The quantity ν_B is a radial transport frequency defined by an expression like Eq. (29) but using the radial curvature and grad-B drifts given by Eq. (24). Positive radial drifts correspond to outward ion flow from the core into the SOL and constitute a source of ions to the SOL, while negative radial flows correspond to inward flows of ions from the SOL into the core and constitute a loss of ions in the SOL. In the divertor channels radial drifts in either direction constitute a loss of ions, and the radial drift frequencies in Eq. (33) are negative.

There is a radially outward directed electric field in the SOL produced by the radial temperature gradient in the SOL

$$E_r(\xi) = \frac{-d\phi}{dr} = -\phi\left(\frac{1}{\phi}\frac{d\phi}{dr}\right); \; -\phi\left(\frac{1}{T}\frac{dT}{dr}\right) \equiv \phi\Delta_T^{-1} \tag{34}$$

which produces poloidal clockwise ExB drifts and particle fluxes in the SOL

$$\upsilon_{E_r xB}^{\theta}(\xi) = \frac{\phi(\xi)\Delta_T^{-1}}{B}, \; \Gamma_{E_r xB}^{\theta}(\xi) = \frac{n(\xi)\phi(\xi)\Delta_T^{-1}}{B} \tag{35}$$

as illustrated in Fig. 4.

The component of this poloidal particle flux parallel to the field in the SOL constitutes a parallel drift particle flux

$$\Gamma_{E_r xB}^{\mathrm{P}}(\xi) = \frac{B_\theta}{B}\Gamma_{E_r xB}^{\theta}(\xi) = \frac{n(\xi)\phi(\xi)\Delta_T^{-1}B_\theta}{B^2} \tag{36}$$

which circulates clockwise around the SOL, as illustrated in Fig. 4.

The temperature distribution at the divertor target plate has been observed to peak somewhat outside the separatrix (i.e. to the right/left of the separatrix in the outer/inner divertor), causing the direction of the radial electric field along the separatrix to change from outward in the SOL to inward into the private flux region in the divertor channer. This produces a parallel

drift particle flux downward in the inner divertor and upward in the outer divertor, as illustrated in Fig. 4.

Both the parallel particle drift fluxes [Eqs. (27) and (34)] are additive to the particle flux due to particle sources calculated from Eq. (.31).

Diamagnetic drifts

The leading order local force balance on the plasma balances the pressure gradient with a *VxB* force, with the result that pressure gradients drive drift velocities orthogonal both to the field and the pressure gradient. In particular, a radial diamagnetic flow is driven by the pressure gradient in the direction perpendicular to the 2D strip in which the transport calculation of this paper is being carried out

$$\upsilon_{dia}^{r} = \frac{-1}{neB}\frac{\partial p}{\partial \mathrm{l}_{\perp}} \; ; \; \frac{-1}{neB}\frac{\partial p}{\partial \mathrm{l}_{\theta}} \; ; \; \frac{-1}{neB}\frac{B}{B_{\theta}}\frac{\partial p}{\partial \xi} \tag{37}$$

The radial pressure gradient also drives a diamagnetic drift velocity in the direction perpendicular to the 2D strip along the field lines of this calculation, but this drift is not considered in this calculation.

The radial diamagnetic drift of particles out of the core is treated as a particle source, and the inward drift is treated as a particle sink, in the continuity equation, in the same manner as discussed for the gradB and *ExB* drifts. However, the diamagnetic drift contribution to the plasma current is divergence-free except for small terms associated with the field non-uniformity, which effect has been represented by the gradB current contribution, so the diagmagnetic drift does not contribute to the parallel current in this calculation.

Total parallel ion flux

The total parallel ion flux is calculated by integrating the particle balance Eq. (33), including the radial transport and radial drift losses and sources, and adding the parallel grad-B and ExB drift fluxes of Eqs. (26) and (36)

$$\begin{aligned}\Gamma(\xi) = \Gamma_{in} + \int_{\xi_{in}}^{\xi} \left[\frac{\Gamma_{\perp}^{sep}}{\Delta_n} - \frac{D_{\perp} n}{\Delta_n^2} + n_e\left(\nu_{ion} - \nu_{rec}\right) + n_i(\nu_{E_{\mathrm{P}}xB} + \nu_B + \nu_{dia}) + S_{E_{\mathrm{P}}xB}^{in} \right] d\xi' \\ + \Gamma_{\nabla B}^{\mathrm{P}}(\xi) + \Gamma_{E_r \times B}^{\mathrm{P}}(\xi)\end{aligned} \tag{38}$$

with Γ_{in} given by the sheath boundary condition of Eq. (5) at the inner divertor target.

The integral balance Eqs. (7) are replaced by the following expressions for the densities just in front of the target plates

$$n_{out} = \frac{\int_{\xi_{stag\Gamma}}^{\xi_{out}} \left[\frac{\Gamma_{\perp}^{sep}}{\Delta_n} - \frac{D_{\perp} n}{\Delta_n^2} + n_e \left(\nu_{ion} - \nu_{rec} \right) + n_i (\nu_{E_{\mathrm{P}}xB} + \nu_B + \nu_{dia}) + S_{E_{\mathrm{P}}xB}^{in} \right] d\xi}{\sqrt{\frac{2T_{out}}{m}}},$$

$$n_{in} = \frac{\int_{\xi_{stag\Gamma}}^{\xi_{in}} \left[\frac{\Gamma_{\perp}^{sep}}{\Delta_n} - \frac{D_{\perp} n}{\Delta_n^2} + n_e \left(\nu_{ion} - \nu_{rec} \right) + n_i (\nu_{E_{\mathrm{P}}xB} + \nu_B + \nu_{dia}) + S_{E_{\mathrm{P}}xB}^{in} \right] d\xi}{\sqrt{\frac{2T_{in}}{m}}} \tag{39}$$

where, as before, the source term $S_{E_{\mathrm{P}}xB}^{in}$ only obtains in the inner divertor for the magnetic field geometry of Figs 1-4.

Impurities[6]

The momentum balance equation (neglecting viscosity) for each individual impurity ion species, k, in a multispecies plasma can be written

$$\frac{d}{d\xi}\left(p_k + n_k m_k \upsilon_k^2 \right) = z_k e n_k E_{\mathrm{P}} + R_{ke} + R_{ki} \tag{40}$$

where "e" refers to electrons and "i" refers to the main plasma ion species. A similar equation obtains for the main ion species, with "k" and "i" interchanged and the atomic physics momentum loss term $-n_i m_i \left(\nu_{el,i} + \nu_{cx,i} \right) \upsilon_i$ added to the right side. The momentum balance equation for the electrons (neglecting inertia and viscosity) is

$$\frac{d}{d\xi}\left(p_e \right) = -e n_e E_{\mathrm{P}} + R_{ei} + \sum_k R_{ek} \tag{41}$$

The collisional friction terms which appear in these equations are

$$R_{ke} = \frac{n_k z_k^2}{n_i} R_{ie} = \frac{n_k z_k^2}{n_i} \left[\frac{-\eta_{\mathrm{P}} n_i e}{z_{eff}} j_{\mathrm{P}} + c_e^{(2)} \frac{n_i}{z_{eff}} \frac{dT}{d\xi} \right] \tag{42}$$

where

$$\eta_{\mathrm{P}} = \left[\frac{0.457}{1.077 + z_{eff}} + 0.29 z_{eff} \right] 2\sigma_{\mathrm{P}}^{-1}, \; c_e^{(2)} = 1.5 \left(1 - \frac{0.6934}{1.3167^{z_{eff}}} \right) \tag{43}$$

and

$$R_{ki} = c_i^{(1)} n_i m_i \nu_{ik} \left(\upsilon_i - \upsilon_k \right) + c_i^{(2)} \frac{n_i}{z_{eff}} \frac{dT}{d\xi} \tag{44}$$

where

$$\nu_{ik} = \frac{m_i + m_k}{m_k} \frac{4\sqrt{2\pi} \ln \Lambda e^4 z_k^2 z_i^2 n_k}{3\sqrt{m_i} T^{3/2}}, \; c_i^{(1)} = \frac{(1+0.24 z_0)(1+0.93 z_0)}{(1+2.65 z_0)(1+0.285 z_0)}, \; z_0 = \frac{\sum_k n_k z_k^2}{n_i}$$
$$c_i^{(2)} = \frac{1.56\left(1+\sqrt{2} z_0\right)(1+0.52 z_0)}{(1+2.65 z_0)(1+0.285 z_0)} \frac{1}{z_0 + \sqrt{(1+m_i/m_k)/2}} \tag{45}$$

A particle continuity equation obtains for each ion species

$$\frac{d\Gamma_k}{d\xi} = S_k - \frac{D_{\perp k} n_k}{\Delta_n^2} + n_k (\nu_{E_{\mathrm{P}} x B,k} + \nu_{B,k} + \nu_{dia,k}) + S_{E_{\mathrm{P}} x B,k}^{in} \tag{46}$$

where the second term on the right represents transport loss perpendicular to the field lines and the first term represents the source of impurity particles, and the last two terms on the right represent the radial drifts of ions between the SOL and the core and the $E_{\mathrm{P}} \times B$ drifting of impurities from the outer to the inner divertor channel (in the geometry of this paper).. For injected impurities, this source is just the local injection rate. For intrinsic impurities (e.g. carbon) this source density is $S_k = \Gamma_{div,i} Y_{ik} / L_k$, where $\Gamma_{div,i}$ is the incident main ion flux on the divertor target plate, Y_{ik} is the sputtering yield for target material "k" for ions of species "i", and L_k is the distance along the field lines in front of the target plate over which the sputtered atoms become ionized (a few cm).

The boundary conditions for the impurity ions are the sheath boundary condition on impurity ion velocity into the target plate at the sound velocity, $\upsilon_k = c_{sk} = \sqrt{2T/m_k}$, and the integral particle balance condition of the particle flux incident on the divertor targets

$$\Gamma_{in,k} = -\left(1 - R_k^{in}\right) n_{k,in} \upsilon_{k,in} = -\left(1 - R_k^{in}\right) \int_{\xi_{in}}^{\xi_{stag\Gamma}} \left(S_k - \frac{D_{\perp k} n_k}{\Delta_n^2} + n_k (\nu_{E_{\mathrm{P}} x B,k} + \nu_{B,k} + \nu_{dia,k}) + S_{E_{\mathrm{P}} x B,k}^{in} \right) d\xi,$$
$$\Gamma_{out,k} = \left(1 - R_k^{out}\right) n_{k,out} \upsilon_{k,out} = \left(1 - R_k^{out}\right) \int_{\xi_{out}}^{\xi_{stag\Gamma}} \left(S_k - \frac{D_{\perp k} n_k}{\Delta_n^2} + n_k (\nu_{E_{\mathrm{P}} x B,k} + \nu_{B,k} + \nu_{dia,k}) + S_{E_{\mathrm{P}} x B,k}^{in} \right) d\xi \tag{47}$$

The incident impurity ions are assumed to be recycled with reflection coefficient R_k as a return flux of impurity ions (i.e. ionization is assumed to take place immediately).

The total parallel impurity particle flux is obtained by integrating Eq. (43) and adding the grad-B and $E_{\mathrm{P}} \times B$ drift particle fluxes calculated as discussed above for the main ions but taking into account the difference in mass and charge.

$$\Gamma_k(\xi) = \Gamma_{k,in} + \int_{\xi_{in}}^{\xi} \left(S_k - \frac{D_{\perp k} n_k}{\Delta_n^2} + n_k (\nu_{E_{\mathrm{P}} x B,k} + \nu_{B,k} + \nu_{dia,k}) + S_{E_{\mathrm{P}} x B,k}^{in} \right) d\xi + \Gamma_{\nabla B,k}^{\mathrm{P}}(\xi) + \Gamma_{E_r \times B,k}^{\mathrm{P}}(\xi) \tag{48}$$

The momentum balance Eq. (40) can be integrated to obtain an equation for the impurity density distribution

$$n_k(\xi)T(\xi)+m_k\upsilon_k(\xi)\Gamma_k(\xi)=n_{in,k}T_{in}+m_k\upsilon_{in,k}\Gamma_{in,k}+$$
$$\int_{\xi_{in}}^{\xi} n_k(\xi')\left[-z_k e\frac{d\phi}{d\xi}+z_k^2\left(\frac{c_e^{(2)}}{z_{eff}}+c_i^{(2)}\right)\frac{dT}{d\xi}-\frac{z_k^2\eta_P e}{z_{eff}}j_P+c_i^{(1)}m_k\nu_{ki}\left(\frac{\Gamma_i}{n_i}-\frac{\Gamma_k}{n_k}\right)\right]d\xi' \quad (49)$$

Integrating the electron momentum balance of Eq. (41) yields an expression for the electrostatic potential that now explicitly accounts for impurities

$$\phi(\xi)=\phi_{in}+\frac{\left[1+c_e^{(2)}\beta/z_{eff}\right]}{e}\left[T(\xi)-T_{in}\right]+\int_{\xi_{in}}^{\xi}\frac{T(\xi')}{en(\xi')}\frac{dn(\xi')}{d\xi'}d\xi'-\int_{\xi_{in}}^{\xi}\frac{\beta\eta_P}{z_{eff}}j_P(\xi')d\xi' \quad (50)$$

where $\beta=1+\sum_k n_k z_k^2/n_i \Big/ 1+\sum_k n_k z_k/n_i$, and ϕ_{in} is given by the sheath relation of Eq. (20)..

B. Effects of drifts on the divertor-SOL plasma distributions

As discussed above and as illustrated previously in a conglomerate way by calculations with the 2D fluid edge codes UEDGE[2,7] and SOLIPS[3], particle drifts due to magnetic field gradients and curvature, electric fields, and pressure gradients have a major impact on determining the distribution of ion densities, temperature, ion flows, currents, electric fields, etc. in the divertor and scrape-off layer of tokamaks. The calculation of the previous section provides an excellent means for isolating and elucidating these effects, to which purpose a series of model problem calculations have been performed.

In order to insure a realistic plasma edge regime, the model problem had machine and plasma core parameters of a DIII-D H-mode discharge, with two exceptions. The two divertor legs were symmetrized (i.e. made more like the figures above than the more asymmetric divertor configuration actually found in DIII-D) in order to avoid geometrical asymmetries that would otherwise additionally complicate the interpretation of the results of the calculations. In such a model problem, the solution in the absence of drifts should be symmetric. Secondly, the D-shape of the plasma was not retained in modeling the essentially vertical grad-B and curvature drifts, with the effect of making the radial and poloidal (parallel) components of these drifts of symmetric magnitude in the inner and outer SOL.

The model (R = 1.7 m, a = 0.6 m, κ = 1.8, B = 2.0 T, I = 1.2 MA, q_{95} = 4) represented a lower single null divertor plasma with the toroidal field such that the grad-B ion drift was down into the divertor; i.e. the configuration illustrated in Figures 1-4. Another calculation was made in which the toroidal magnetic field direction was reversed. The power and particle fluxes into the SOL from the core plasma were calculated to match experimental conditions for an H-mode discharge.

The equations of the previous section were numerically integrated over a grid structure along the field lines from the inner to the outer divertor plates. A small (5 cm in the parallel dimension, about 1 cm in the poloidal dimension normal to the target plates) recycling region in front of each divertor plate, a pre-recyling region of twice that length, and 8 other regions represented each divertor channel up to and including the X-point region (total length of each 2.95 m along field lines). The SOL plasma from inner to outer X-points (parallel distance 53.02

m) was divided into 30 equal regions. With reference to Fig. 1, the recycling regions are 1 and 50, the inner and outer X-points are in regions 10 and 41, the inner and outer mid-planes are in regions 18 and 33, and the "crown" at the top is regions 25 and 26. The symmetry point is between regions 25 and 26. All results will be plotted against region number. With the numerical integration scheme employed in this paper, the densities, temperature and quantities constructed from them, such as the grad-B drift velocities, were calculated as average values over each region (e.g. the density shown in the following figures for location "1" is an average density over the first, recycling region in front of the inner divertor, and the density shown for location "33" is an average over the region containing the outer SOL mid-plane). However, quantities such as the parallel particle fluxes and particle velocities, parallel currents, electrostatic potential and associated electric fields and *ExB* drift velocities were calculated at the interfaces between regions (e.g. the currents and velocities shown for location "1" are the values at the inner divertor target plate, the currents and velocities shown for location "26" are the values at the symmetry point between regions 25 and 26, and the currents and velocities shown for location "51" are the values at the outer divertor plate.

Particle sources were treated as follows. The gas fueling source for the deuterium ($1.5\text{x}10^{20}$ #/s into the upper outboard plasma chamber) was represented explicitly, and the resulting neutral atoms were transported through the edge region across the separatrix to fuel the core plasma. An average ion flux of $\Gamma_{\perp} = 1.6\text{x}10^{20}$ #/m^{2}s from the core plasma into the SOL was calculated, taking into account this neutral influx into this core, but consisting mostly of ions produced by the neutral beam particle source. The deuterium ions striking the target plates (consisting both of ions crossing the separatrix from the core and ions produced by ionization of neutral atoms in the SOL and divertor) were reflected as neutral atoms at about one-half their incident energy or re-emitted as molecules which were dissociated into 2 eV atoms in the recycling regions 1 and 50 and were then transported throughout the edge region until ionized in the divertor, SOL or plasma edge inside the separatrix.

Two impurity ion species were modeled, carbon which is an intrinsic impurity, and argon which is sometimes used to enhance radiation. The carbon source was the calculated sputtering of the deuterium ions incident on the divertor target plates and was distributed over the first two regions (i.e. 1 and 2, 49 and 50) in front of the target. Carbon was transported as a single ion species with an average charge state that varied with local electron temperature along the field lines. Carbon ions returning to the target plates were reflected with a coefficient R = 0.99, which included in an approximate manner also the effects of carbon self-sputtering. An argon source of $2\text{x}10^{19}$#/s injected in the private flux region was assumed to be pumped by the divertor plasma and was represented as a uniformly distributed particle source in the two divertor plasmas (regions 1-9 and 42-50). The argon ions incident on the divertor targets were reflected with coefficient R=0.99.

An average heat flux of $Q_{\perp} = 8.\ 8\text{x}10^4$ W/m^2 into the SOL from the core plasma was calculated from a core power balance, taking into account the 4.9 MW neutral beam heating, the small ohmic heating and the radiation from inside the separatrix. Both this heat flux and the above ion flux into the SOL from the core were uniformly distributed over the SOL regions 11-40.

Radial transport was represented by a gradient scale length of 2 cm for density and temperature.

Drifts

The total parallel particle flux, taking into account the gradB, ExB and diamagnetic drifts as well as the ion flux into the SOL from the core, was calculated. The diamagnetic drifts are very large just in front of the divertor plates where the parallel pressure gradients are large, but otherwise the gradB drifts are the most important.

Three different situations were calculated for the sake of comparison: i) with the grad-B, *ExB* and diagmagnetic drifts turned off, ii) with these drifts turned on and the toroidal magnetic field in the direction opposite to the plasma current shown in Figs. 1-4, denoted B(-), and iii) with the drifts turned on and the toroidal magnetic field reversed and aligned with the current opposite to the direction shown in Figs. 1-4, denoted B(+). The drifts for case ii) are shown in Figs. 5 and 6, and the drifts for case iii) are just the negative of these. For the B(-) field direction the grad-B and curvature drifts were downward into the divertor, while for the B(+) field direction these drifts were upward away from the divertor.

Density and temperature distributions

The calculated densities and temperatures are shown in Figs. 5 and 6, respectively. The drifts do not have much effect on the deuterium density and temperature distributions, except in the recycling regions 1 and 50, where the diamagnetic and *ExB* drifts are large. The *ExB* drifts of Eq. (30) are largest near the divertor target plates because the electrostatic potential increases most rapidly there, and the diagmagnetic drifts are also largest near the divertor target plates, but because the parallel pressure gradients are largest there. The effect of drifts on the carbon and argon density profiles is greater than on the deuterium density profile.

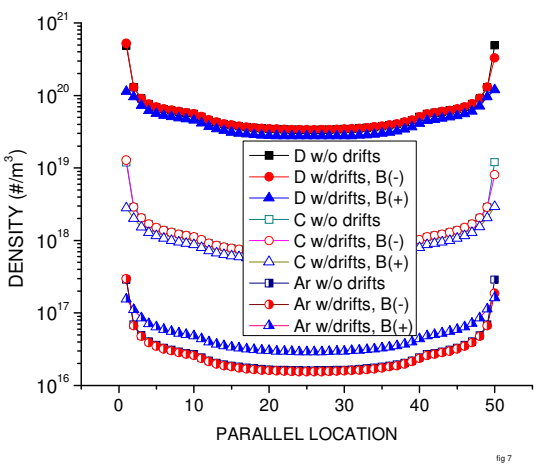

Figure 5 Ion Densities in SOL and Divertor (regions1-9 & 42-50)

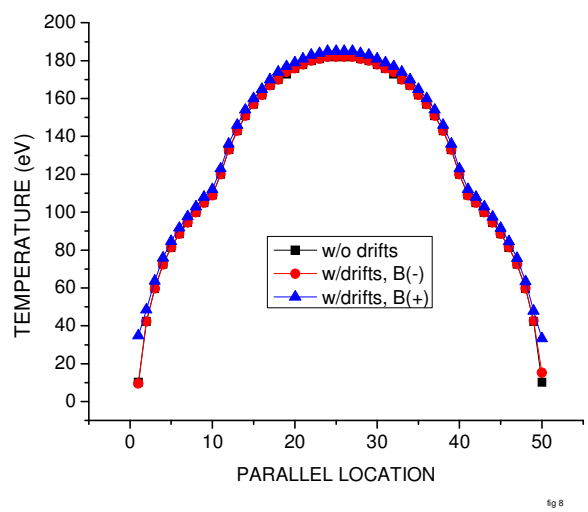

Figure 6 Temperatures in SOL and Divertor (regions1-9 & 42-50)

With respect to Eqs. (12) and (13), the density profile is determined by the force balance requirement that the pressure plus inertial forces are constant over the SOL and divertor except for the momentum dissipation, which takes place for the deuterium ions primarily via atomic

physics collisions with neutrals in the divertor. For the parameters of this calculation, for which the pressure in the SOL is almost 1000 Pa, the pressure term dominates the force balance, and the drift effects, which enter the density calculation via the inertial term in the force balance, have minimal effect except in the divertor, particularly in the recycling regions. The effect of drifts on the temperature profile is via the density profile and is correspondingly small in this problem, again except in the recycling regions. A greater sensitivity to drifts was found in a similar comparison[10] for which the pressure was an order of magnitude lower in the SOL; such a sensitivity would result in this calculation also if the pressure contribution to the *M* term in Eq. (13) was decreased by an order of magnitude.

Electrical current density, potential, and fields

The grad-B and curvature drifts produce radial currents proportional to the grad-B and curvature drifts given by Eqs. (24) and indicated in Fig. 2. Without drifts, the temperature distribution was symmetric and there was no thermoelectric current. With the B(-) drifts, there was a temperature asymmetry that drove a thermoelectric current and large radial gradB drift currents that drove parallel currents in order to maintain a divergence-free total current density. These radial grad-B currents and the compensating parallel currents were in opposite directions for the B(-) and B(+) field directions. Note that the grad-B currents integrated to zero over the SOL to maintain ambipolarity, as discussed in connection with Eq. (27). Scrape-off layer currents of comparable magnitude have been measured in DIII-D H-mode discharges, but we are unaware of any measurements of current profiles in the SOL.

With the drifts turned off, the symmetric temperature and density distributions shown in Figs. 6 and 5 produced the symmetric electrostatic potential distribution shown in Fig. 7, as calculated from Eq. (19) using Eqs. (20), (28) and (29). Turning on the grad-B drift and changing the direction of the toroidal magnetic field both produce a dramatic change in the parallel distribution of the electrostatic potential, primarily because to the differences in the parallel currents shown in Fig. 8.

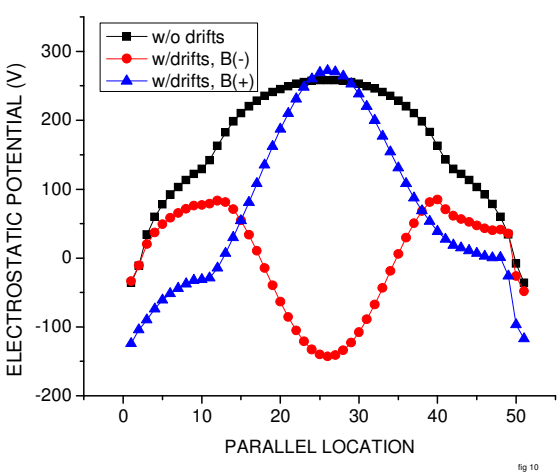

Figure 7 Electrostatic potential distribution in divertor (regions 1-9 and 42-50) and SOL.

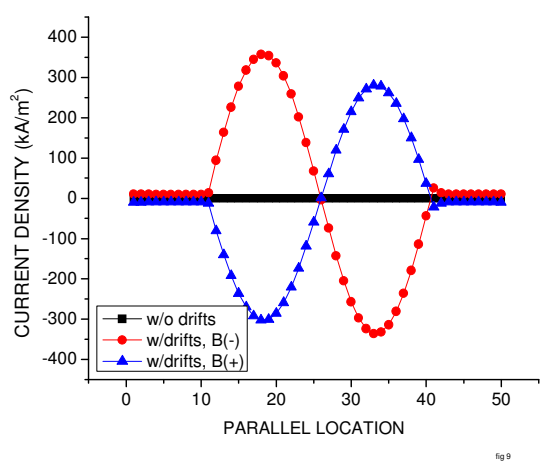

Figure 8 Parallel plasma current density in divertor (regions 1-9 and 42-50) and SOL.

Differentiation of the electrostatic potential profiles of Fig.10 produces the parallel electric fields of Eq. (30), which are shown in Fig. 11. These fields are generally small in the SOL but become quite large in the divertors, particularly in the vicinity of the target plates.

As discussed in connection with Eq. (34), the implication of Eq. (19) is that the radial gradient of the electrostatic potential (the radial electric field) should be approximately proportional to the radial temperature gradient, which is characterized by the parameter $\Delta_T^{-1} = -dT/Tdr$. Using $\Delta_T = 2$ cm and the temperature profiles of Fig. 8, Eq. (34) yields radial electric fields which are quite different with and without drifts and for the B(-) and B(+) toroidal field directions, primarily because of the difference caused in the electrostatic potentials of Fig. 7 by the differences in parallel current distributions shown in Fig. 8. For the B(-/+) field direction, the positive/negative radial electric field in the SOL corresponds to the temperature decreasing radially outward from the separatrix. In the divertor, the experimental evidence is that the peak in the temperature profile just in front of the target is somewhat outside the separatrix, so that at the separatrix there is a transition from a 'negative' temperature gradient in the SOL to a positive temperature gradient at the target plate, leading to an oppositely directed radial electric field into the private flux region.

Parallel flows

In the absence of drifts, because of the symmetry of the geometry and of the particle source from the core plasma into the SOL, the particle flows go symmetrically to the inner and outer divertor targets, as shown for D in Fig. 9. The sputtered particle sources in front of the divertor targets for C are also symmetric, and the resulting C particle fluxes are symmetric in the absence of drifts, as shown in Fig. 10. For D, the principle source of ions is the particle flux $\Gamma_\perp^{sep}$ from the core, although there is a smaller source due to ionization of neutrals (primarily in the divertor). Without drifts, flow stagnation is at the symmetry point (between regions 25 and 26) at the crown of the SOL, as shown for in Fig. 9. For C the source is the sputtered carbon from the divertor plates deposited uniformly in the first two regions (1 and 2, 50 and 49), which is basically entrained in the high deuterium flow towards the plates in these regions.

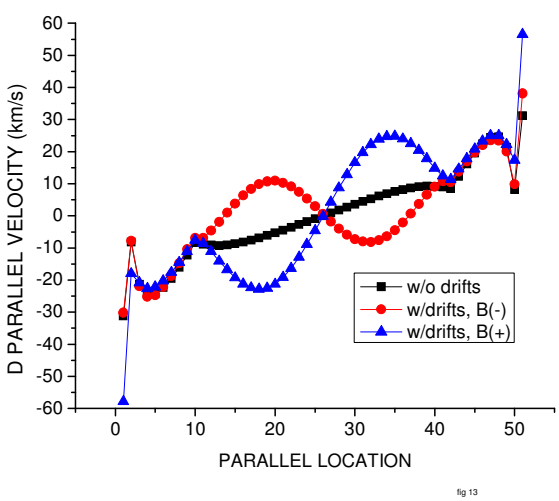

Figure 9 Parallel deuterium ion velocity in divertor (regions 1-9 and 42-50) and SOL.

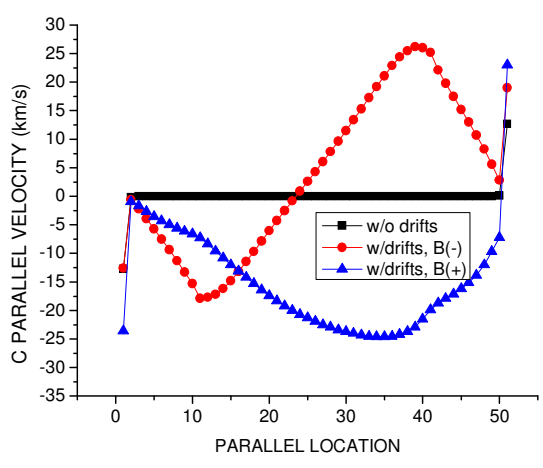

Figure 10 Parallel carbon ion velocity in divertor (regions 1-9 and 42-50) and SOL.

Turning the drifts on produces two types of effects. First, the parallel *ExB* and grad-B drifts of Eqs. (36) and (26) produce a local increase or decrease in particle parallel flow velocity. Second, the outward and inward radial particle drifts of Eqs. (24), (30) and (37) produce sources and sinks of particles in the SOL and divertor, which affect the parallel particle flux as indicated by Eqs. (38) and (50). The parallel deuterium ion flux must increase or decrease in response to this variation in ion sources and sinks to satisfy the continuity equation. The momentum balance equation is dominated by the pressure term in the SOL, which produces the relatively flat ion distribution over the SOL, so the variation in ion flux requires the variation in deuterium parallel velocity shown in Fig. 9.

With reference to Fig.5 for the B(-) field direction, both the grad-B and *ExB* radial drifts are out of the core, providing a particle source in the SOL between the X-point (region 10) and the mid-plane (region18) of the inner SOL. Between the mid-plane (region 18) and the crown (region (25) the grad-B drift is inward and the *ExB* drift is outward, providing a sink and a source of particles to the SOL. Between the crown (region 26) and the mid-plane (region 33) of the outer divertor both drifts are inward from the SOL into the core, providing a particle sink in the SOL. From the mid-plane (region 33) to the X-point (region 41) the grad-B drift is outward and the *ExB* drift is inward, proving a source and a sink, respectively, of particles to the SOL. The diagmagnetic drift is relatively smaller in the SOL. The particle flux variation in the SOL for deuterium for the B(-) field direction shown in Fig 13 reflects this variation in particle source and sink distributions. Note that there are three stagnation points in the deuterium parallel flow in the SOL for the B(-) drifts. Recent probe measurements of deuterium flow in a DIII-D L-mode discharge with the same B(-) field direction found a similar magnitude of deuterium flow in the crown region and also two flow stagnation points. When the field direction is changed from B(-) to B(+) all of the radial drift directions are reversed, reversing the particle source and sink distributions in the SOL and resulting in the deuterium velocity shown in Fig. 9

The calculated carbon parallel flow distributions are shown in Fig. 10. The same type of variation in particle sources and sinks because of the radial drifts also is present for carbon, but obviously other factors are dominant in the carbon force balance because the carbon parallel flows are of the opposite sign from the deuterium parallel flows in many locations.

Penetration of injected argon into the core plasma

It has been observed experimentally in DIII-D H-mode discharges that the penetration of the core plasma by argon injected into the private flux region of the divertor is significantly greater when the ion grad-B drift is towards the divertor [B(-)] than away from the divertor [B(+)]. In the model of this paper, the net penetration of argon from the SOL into the core can be characterized by the parameter $\int_{\xi_{Xin}}^{\xi_{Xout}} n_{Ar}\left(\upsilon^r_{E_{\mathrm{P}}xB,Ar}+\upsilon^r_{B,Ar}+\upsilon^r_{dia,Ar}\right)d\xi<0$, indicating a net radially inward (-) drift. This parameter is calculated to be < 0 for the B (-) field direction shown in the Figs. 1-4, with the ion grad-B drift direction into the divertor, and to be > 0 for the reversed B(+) field direction with the ion grad-B drift direction out of the divertor, in qualitative agreement with the experimental observation. The significantly lower argon density shown in the divertor and SOL in Fig. 7 for the B(-) than the B(+) magnetic field configurations is also indicative of this same trend; since both calculations were performed with the same argon source and

recycling coefficient, the lower argon concentration in the SOL for B(-) than for B(+) indicates a larger argon concentration in the core (by a factor 2-3).

II. Summary

A computationally tractable model has been developed for the calculation of density, temperature, flow, current, and electrostatic potential and fields along the separatrix in tokamak scrape-off layers and divertors. The calculation is carried out in a 2D strip following the magnetic field lines around the tokamak from the inner to the outer divertor targets. Cross-field transport and magnetic geometry effects are treated analytically, reducing the calculation to a coupled set of nonlinear equations along the field lines, which are integrated numerically.

The calculation model was applied to calculate the effects of drifts and toroidal magnetic field direction on flows, currents, electric fields, density and temperature distributions in a model problem with parameters characteristic of a DIII-D H-mode discharge. A number of interesting phenomena—multiple reversal of parallel flows and currents in the SOL, reversal of the sign of the electrostatic potential and electric fields with the reversal of the toroidal magnetic field direction, larger penetration of the core plasma by argon injected in the divertor when the ion gradB drift was towards than away from the divertor, etc.—were predicted, some of which have been experimentally observed.

Acknowledgement

The author would like to express his appreciation to R. Isler (ORNL), R. Groebner (GA), M. Groth (LLNL), T. Petrie (GA), M. Schaeffer (GA) and G. Staebler (GA) for discussion of various aspects of this work and to General Atomics for hosting him during much of it. The work was supported by the U. S. Department of Energy Grant No. DE-FG02-00-ER54538 with the Georgia Tech Research Corporation.

References

1. P. C. Stangeby, *The Plasma Boundary of Magnetic Fusion Devices*, IOP Press, Bristol (2000).
2. T. D. Rognlien, D. D. Ryutov, N. Mattor and G. D. Porter, Phys. Plasmas, 5, 1851 (1999); Contrib. Plasma Phys., 38, 152 (1998); Plasma Phys. Control. Fusion, 47, A283 (2005)
3. V. A. Rozhansky, S. P. Voskoboynikov, E. G. Kaveeva, D. P. Coster and R. Schneider, Nucl. Fusion, 41, 387 (2001);42, 1110 (2002); 43, 614 (2003); Contrib. Plasma Phys., 46,575 (2006).
4. M. Groth, G. D. Porter, J. A. Boedo, *et al.*, "Measurements and simulations of main scrape-off layer flows in DIII-D", Plasma Surface Interaction Conf. (Toledo, 2008), J. Nucl. Mater. (to be published).
5. T. W. Petrie, N. H. Brooks, M. E. Fenstermacher, *et al*., Nucl. Fusion, 48, (2008); also Plasma Surface Interaction Conf. (Toledo, 2008), J. Nucl. Mater. (to be published).
6. M. Keilhacker, R. Simonini, A. Taroni and M. L. Watkins, Nucl. Fusion, 31, 535 (1991).
7. G. D. Porter, S. L. Allen, M. Brown, *et al.*, Phys. Plasmas, 3, 1967 (1996).

.

2. COMPARISON OF THEORETICAL AND EXPERIMENTAL HEAT DIFFUSIVITIES IN THE DIII-D EDGE PLASMA

W. M. Stacey, Georgia Tech

Abstract

Predictions of theoretical models for ion and electron heat diffusivity have been compared against experimentally inferred values of the heat diffusivity profile in the edge plasma of two H-mode and one L-mode discharge in DIII-D [J. Luxon, Nucl. Fusion, 42, 614 (2002)]. Various widely used theoretical models based on neoclassical, ion temperature gradient modes, drift Alfven modes and radiative thermal instability modes for ion transport, and based on paleoclassical, electron temperature gradient modes, trapped electron modes, and drift resistive ballooning modes for electron transport were investigated.

A. Introduction

The structure of the density and temperature profiles in the edge of tokamak plasmas has long been an area of intense research, at least in part because of the apparent correlation of this structure to global plasma performance. Essential to an understanding of the structure in the edge density and temperature profiles, in the absence or in between edge-localized-modes (ELMs), is an understanding of the underlying transport mechanisms.

A methodology for inferring the underlying heat diffusivities from measurements of temperature and density profiles in the plasma edge, which takes into account convection, atomic physics and radiation cooling, ion-electron energy exchange and other edge phenomena, has recently been developed and applied to several different types of DIII-D[1] discharges[2-5]. While some comparisons with theoretical formulas have been included in this previous work, the emphasis was on the development of accurate fits of the measured data for use in the inference of experimental heat diffusivity profiles and the accurate calculation of heat and particle fluxes to be used in these inferences. The purpose of this paper is to report a comparison of several theoretical predictions of heat diffusivities with the experimentally inferred heat diffusivities, primarily to gain insight as to the more likely transport mechanisms in the plasma edge, and secondarily to compare some currently used transport models with experiment. To this end, a number of computationally tractable theoretical heat diffusivity models which are widely used for transport modeling have been evaluated using the same experimental data from which the experimental heat diffusivities were inferred.

We note the significant ongoing effort to model transport processes with large-scale gyro-kinetic or gyro-fluid computer simulations of turbulent transport (e.g. Ref. 6). Such calculations will in the future be able to provide a rigorous test of turbulent transport mechanisms against experiment. However, such calculations for the plasma edge (including the various atomic physics, radiation and other edge phenomena) are not yet widely available. Thus, we were motivated to undertake a comparison of experimentally inferred heat diffusivities in the edge of DIII-D with the predictions of computationally tractable theoretical models evaluated also using that experimental data, with the intent of obtaining qualitative and semi-quantitative physical insights that can

provide guidance for future work. Even so, some of the models that we use are state-of-the-art for the particular transport mechanism (e.g. the neoclassical and paleoclassical formulas) and all of them are representative of forms used today by transport modelers to represent heat diffusivities in transport simulations.

The various theoretical models for heat diffusivities are set forth in Section II, and the procedure used to infer experimental profiles of heat diffusivity in the edge plasma is briefly summarized in section III. The DIII-D shots used for the comparison are discussed in section IV, where the various experimental data important to the comparison are given. The comparison of the predictions of the theoretical models with the experimentally inferred heat diffusivity profiles is summarized in section V, and the details of the comparison are presented in an appendix. Finally, the work is summarized in section VI.

B. Theoretical thermal energy transport models

Ion transport

1. Neoclassical

The neoclassical Chang-Hinton (neo_ch) expression for the ion thermal conductivity is[7,8]

$$\chi_i^{neoch} = \varepsilon^{1/2} \rho_{i\theta}^2 \nu_{ii} \left[a_1 g_1 + a_2 (g_1 - g_2 \right] \tag{1}$$

where the a's account for impurity, collisional and finite inverse aspect ratio effects and the g's account for the effect of the Shafranov shift

$$\begin{aligned}
a_1 &= \frac{0.66(1+1.54\alpha) + \left(1.88\sqrt{\varepsilon} - 1.54\varepsilon\right)(1+3.75\alpha)}{1+1.03\sqrt{\mu_j^*} + 0.31\mu_j^*} \\
a_2 &= \frac{0.59\mu_j^*\varepsilon}{1+0.74\mu_j^*\varepsilon^{3/2}} \left[1 + \frac{1.33\alpha(1+0.60\alpha)}{1+1.79\alpha} \right] \\
g_1 &= \frac{1+\frac{3}{2}\left(\varepsilon^2 + \varepsilon\Delta'\right) + \frac{3}{8}\varepsilon^3\Delta'}{1+\frac{1}{2}\varepsilon\Delta'} \\
g_2 &= \frac{\sqrt{1-\varepsilon^2}\left(1+\frac{\varepsilon\Delta'}{2}\right)}{1+\frac{\Delta'}{\varepsilon}\left(\sqrt{1-\varepsilon^2}-1\right)}
\end{aligned} \tag{2}$$

where $\alpha = n_I Z_I^2 / n_i Z_i^2$, $\mu_i^* = \nu_{ii} qR/\varepsilon^{3/2} \upsilon_{thi}$ and $\Delta' = d\Delta/dr$, where Δ is the Shafranov shift. The impurity thermal conductivity is obtained by interchanging the i and I subscripts in the above expressions.

The Shafranov shift parameter may be evaluated from[9]

$$\Delta' \equiv \frac{d\Delta}{dr} = -\frac{1}{RB_\theta^2}\left(\frac{r^3}{a^2}\beta_\theta B_{\theta a}^2 + \frac{1}{r}\int_o^r B_\theta^2 r' dr'\right) \tag{3}$$

where $\beta_\theta = p/(B_\theta^2/2\mu_0)$ and $B_{\theta a}$ denotes the poloidal magnetic field evaluated at $r = a$. Since we need this quantity at $r \approx a$, we can take advantage of the definition of the internal inductance

$$l_i = \frac{2\int_o^a B_\theta^2 r' dr'}{a^2 B_{\theta a}^2} \tag{4}$$

where $\beta_{\theta a}$ denotes the quantity evaluated using the average pressure over the plasma and $B_{\theta a}$ is the poloidal magnetic field evaluated at the last closed flux surface (LCFS). Using a parabola-to-a-power current profile $j(r) = j_0(1 - (r^2/a^2))^v$, for which the ratio of the values of the safety factor at the edge to the center is $q_a/q_0 = v + 1$, and a fit[9] $l_i = ln(1.65 + 0.89v)$ leads to the simple expression

$$\begin{aligned}\Delta' &= -\frac{a}{R}\left(\bar{\beta}_{\theta a} + \frac{1}{2}l_i\right) \\ &= -\frac{a}{R}\left(\bar{\beta}_{\theta a} + \frac{1}{2}ln\left(1.65 + 0.89\left(\frac{q_a}{q_o} - 1\right)\right)\right)\end{aligned} \tag{5}$$

In the presence of a strong shear in the radial electric field, the particle banana orbits are squeezed, resulting in a reduction in the ion thermal conductivity by a factor of $S_E^{-3/2}$, where[10]

$$S_E = \left|1 - \rho_{i\theta}\left(\frac{d\ln E_r}{dr}\right)\left(\frac{E_r}{\upsilon_{thi}B_\theta}\right)\right| \tag{6}$$

Here $\rho_{i\theta}$ is the ion poloidal gyroradius.

The neoclassical transport phenomena are always present and are believed to constitute an irreducible minimum for transport.

2. *Ion temperature gradient (itg) modes*

The itg modes are believed to be among the most likely of several drift wave instabilities which could be responsible for anomalous thermal transport. For a sufficiently large ion temperature gradient $\left(L_{Ti} \equiv -T_i/(dT_i/dr) < L_{Ti}^{crit}\right)$ the toroidal ion temperature gradient (itg) modes become unstable. In the large aspect ratio, low beta limit, the critical temperature gradient for the destabilization of itg modes can be written[11]

$$\left(\frac{R}{L_{Ti}}\right)_{\text{crit}} = \max\begin{bmatrix} 0.8\, R/L_{ne}, or \\ \left(1 + 1/\tau\right)\left(1.33 + 1.91\frac{r}{q^2}\frac{dq}{dr}\right)(1 - 1.15\varepsilon) \end{bmatrix} \tag{7}$$

where $\tau \equiv Z_{eff}T_e/T_i$. For $R/L_{Ti} < (R/L_{Ti})_{crit}$, the toroidal etg modes are linearly stable, but for $R/L_{Ti} > (R/L_{Ti})_{crit}$ these modes are unstable and produce thermal ion transport.

Several early gyro-Bohm expressions (e.g. Ref. 12) for the heat diffusivity of the itg modes take the form

$$\chi_i^{itg} = \frac{5}{4}\left(\frac{1}{RL_{Ti}}\right)^{1/2}\left(\frac{\rho_i T_e}{e_i B}\right) H\left(R/L_{Ti} - \left(R/L_{Ti}\right)_{crit}\right) \tag{8}$$

where H is the Heaviside function, ρ_i is the ion gyroradius in the toroidal magnetic field B, and $k_\perp \rho_i = 2$ has been used.

More recently, Horton, et al.[13,14] combined semi-quantitative knowledge of microturbulence with information from experiments to develop an expression for the ion thermal diffusivity due to the itg modes. They argued that transport over a scale much larger than the radial correlation length λ_c of the turbulence but much less than the minor radius of the plasma must be governed by diffusive processes with a local thermal diffusivity that depends on the local features of the turbulence, i.e. $\chi_i = \left(\lambda_c^2/\tau_c\right) f\left(\upsilon_{ExB}\tau_c/\lambda_c\right)$, where τ_c is a characteristic time. They then combined the condition for marginal stability of the itg modes $\left(T_e/eB\right)\left(k_\theta/L_{Ti}\right) \approx c_s/qR$ with the fact that the propagation time for ion acoustic waves over the effective parallel distance qR of the system is qR/c_s to estimate the cutoff wavenumber $k_\perp^{cut} \approx \rho_s\left(qR/L_{Ti}\right)$. [The symbol ρ_s is widely used for the ion gyroradius, and we will use both this symbol and ρ_i.] Assuming that the radial and poloidal correlation lengths are the same, they then estimated the radial correlation length $\lambda_c \approx \rho_s\left(qR/L_{Ti}\right)$. The maximum value of the growth rate $\gamma \approx \upsilon_{thi}\left(k_\perp \rho_s\right)/\sqrt{RL_{Ti}}$ occurs for $\left(k_\perp \rho_s\right) \approx 1/2$. Estimating the characteristic time as the inverse of the maximum growth rate then yields[13]

$$\chi_i^{itg} = C_i q^2 \left(\frac{T_e}{eB}\right)\left(\frac{\rho_s}{L_{Ti}}\right)\left(\frac{R}{L_{Ti}}\right)^{3/2} \tag{9a}$$

where C_i was interpreted to be a measure of the fraction to which the turbulence reached the full mixing length level $1/L_T$; $e\phi/T$ and was determined $C_i = 0.014$ by fitting the above formula to experimental data from Tore Supra[14]. We will use this value of C_i. Equation (9a) predicts a stronger dependence on the ion temperature gradient than does Eq. (8). If instead the characteristic time was estimated as the inverse of the linear growth rate with $k_\perp \approx 1/2\rho_s$ the estimate of the ion thermal diffusivity is instead[13]

$$\chi_i^{itg} = C_i q \left(\frac{T_e}{eB}\right)\left(\frac{\rho_s}{L_{Ti}}\right)\left(\frac{R}{L_{Ti}}\right)^{1/2} \tag{9b}$$

A more complete treatment of the transport due to toroidal itg modes was developed by Weiland[15]. The model was developed from a linear stability analysis of the continuity, momentum and energy balance equations, resulting in a dispersion relation that must be calculated numerically. In this paper we will use the wave number at which the maximum transport for itg modes occurs, $k_\perp = 0.3/\rho_s$, rather than solving the dispersion relation. The resulting ion transport is derived from the quasilinear approximation and can be considered a version of itg, and the electron transport can be considered a version of tem.

The onset (instability) condition for this toroidal itg mode is

$$\eta_i > \eta_{ith} = \frac{2}{3} - \frac{\tau}{2} + \varepsilon_n \left(\frac{\tau}{4} + \frac{10}{9\tau} \right) + \frac{\tau}{4\varepsilon_n}$$
$$- \frac{k_\perp^2 \rho_s^2}{2\varepsilon_n} \left[\frac{5}{3} - \frac{\tau}{4} + \frac{\tau}{4\varepsilon_n} - \left(\frac{10}{3} + \frac{\tau}{4} - \frac{10}{9\tau} \right) \varepsilon_n + \left(\frac{5}{3} + \frac{\tau}{4} - \frac{10}{9\tau} \right) \varepsilon_n^2 \right] \tag{10}$$

where

$$\eta_{i,e} \equiv \frac{L_n}{L_{Ti,e}}, \ \tau \equiv \frac{Z_{eff} T_e}{T_i}, \ \varepsilon_n \equiv \frac{2L_n}{R} \tag{11}$$

The quasi-linear estimates for the thermal diffusivities in the Weiland model were constructed by estimating the turbulent heat fluxes and then assuming they satisfied a Fick's law (i.e. were conductive). We will distinguish such effective thermal diffusivities which also indirectly account for any convective heat fluxes by referring to them as effective heat diffusivities. The effective ion heat diffusivity obtained in this way is

$$\left(\chi_i^{itg} \right)_{eff} = \frac{1}{\eta_i} \left[\eta_i - \frac{2}{3} - \frac{10}{9} \frac{\varepsilon_n}{\tau} \right] \frac{\gamma^3 / k^2}{\left(\omega_r - \frac{5}{3} \omega_{Di} \right)^2 + \gamma^2} \tag{12a}$$

if parallel ion motion and trapped particle effects are neglected, and is

$$\left(\chi_i^{itg} \right)_{eff} = \frac{1}{\eta_i} \left[\eta_i - \frac{2}{3} - (1 - f_{tr}) \frac{10}{9} \frac{\varepsilon_n}{\tau} - \frac{2}{3} f_{tr} \Delta_i \right] \frac{\gamma^3 / k^2}{\left(\omega_r - \frac{5}{3} \omega_{Di} \right)^2 + \gamma^2} \tag{12b}$$

when they are taken into account. The drift frequencies are calculated from the curvature and grad-B drifts

$$\omega_{Di} = \frac{3kT_i}{eB_\phi R}, \ \omega_{De} = -\frac{3kT_e}{eB_\phi R} \tag{13}$$

and from the density gradients

$$\omega_{*i} = -\frac{kT_i}{eB_\phi L_n}, \ \omega_{*e} = \frac{kT_e}{eB_\phi L_n} \tag{14}$$

the growth rate of the mode is

$$\gamma = \frac{\omega_{*e} \sqrt{\varepsilon_n / \tau}}{1 + k^2 \rho_s^2} \sqrt{\eta_i - \eta_{ith}} \tag{15}$$

the oscillatory frequency of the mode is

$$\omega_r = \frac{1}{2} \omega_{*e} \left[1 - \varepsilon_n \left(1 + \frac{10}{3\tau} \right) - k^2 \rho_s^2 \left(1 + \frac{1 + \eta_i}{\tau} - \varepsilon_n - \frac{5\varepsilon_n}{3\tau} \right) \right] \tag{16}$$

and the quantity Δ_i is

$$\Delta_i = \frac{1}{N}\left\{ \begin{array}{l} \left|\hat{\omega}\right|^2 \left[\begin{array}{l} \left|\hat{\omega}\right|^2 (\varepsilon_n - 1) + \hat{\omega}_r \varepsilon_n \left(\frac{14}{3} - 2\eta_e - \frac{10}{3}\varepsilon_n \right) + \\ \frac{5}{3}\varepsilon_n^2 \left(-\frac{11}{3} + 2\eta_e + \frac{7}{3}\varepsilon_n \right) - \frac{5}{3\tau}\varepsilon_n^2 \left(1 + \eta_e - \frac{5}{3}\varepsilon_n \right) \end{array} \right] \\ + \frac{50}{9\tau}\hat{\omega}_r \varepsilon_n^3 (1 - \varepsilon_n) - \frac{25}{9\tau}\left(\frac{7}{3} - \eta_e - \frac{5}{3}\varepsilon_n \right) \end{array} \right\} \tag{17}$$

where

$$\hat{\omega}_r = \frac{\omega_r}{\omega_{*e}}, \quad \hat{\gamma} = \frac{\gamma}{\omega_{*e}}, \quad \left|\hat{\omega}\right|^2 = \hat{\omega}_r^2 + \hat{\gamma}^2 \tag{18}$$

and

$$N = \left(\hat{\omega}_r^2 - \hat{\gamma}^2 - \frac{10}{3}\hat{\omega}_r \varepsilon_n + \frac{5}{3}\varepsilon_n^2 \right)^2 + 4\hat{\gamma}^2 \left(\hat{\omega}_r - \frac{5}{3}\varepsilon_n \right)^2 \tag{19}$$

A simplification of the Weiland formalism (in which the form for the particle diffusion coefficient is used also for the ion heat diffusivity) is given by the Kalupin et al.[16] estimate

$$\left(\chi_i^{itg}\right)_{eff} = \frac{\rho_i T_e}{0.3 e B_\phi} \left[\left(L_{Ti}^{-1} - \frac{2}{3} L_n^{-1} \right) \frac{1}{\tau R (1 - f_{tr})} - \frac{1}{8}\left(\frac{2}{R} - L_n^{-1} \right)^2 (1 - f_{tr})^{-2} - \frac{20}{9}\frac{1}{\tau^2 R^2} \right]^{1/2} \tag{20}$$

used in transport simulations by the Julich group[16] , where k_{itg} ; $0.3/\rho_i$ has been used to represent the itg modes causing the largest transport in an improved mixing length approximation.

When $R/L_{Ti} > (R/L_{Ti})_{crit}$, or $\eta_i > \eta_{ith}$, the itg modes are unstable and produce transport. However, the transport predicted by Eqs. (8), (9), (12) and (20) does not take into account the predicted[17] damping of the growth rates of these modes by *ExB* shear. The itg modes are predicted to be substantially suppressed by *ExB* flow shear when the *ExB* shearing rate for turbulent eddies

$$\omega_{ExB} \equiv \left| \frac{R B_\theta}{B_\phi} \frac{\partial}{\partial r} \left(\frac{E_r}{R B_\theta} \right) \right| \tag{21}$$

is comparable to or greater than the maximum linear growth rate $\gamma_{\max}^{itg}$ of the mode spectrum[18]. For the itg mode with the greatest transport the wave number is[13] k ; $0.3/\rho_s$, and the maximum growth rate is[13] $\gamma_{\max}^{itg}$; $\frac{0.3 c_s}{(L_{Ti} R)^{1/2}}$ $\left(c_s = \sqrt{T_e/m_i}\right)$. This *ExB* suppression can be represented by the multiplicative shear suppression factor[19,20]

$$F_s^{itg} = \frac{1}{1 + \left(Y_s^{itg}\right)^2}, \qquad Y_s^{itg} = \omega_{EXB} / \gamma_{\max}^{itg} \tag{22}$$

so that the transport rates of Eqs. (8), (9), (12) and (20) are reduced to

$$\chi_i^{itg} = F_s^{itg}\left(\omega_{ExB}\right)\chi_i^{itg} \tag{23}$$

by *ExB* flow shear

An additional magnetic shear [$S_m \equiv (r/q)(dq/dr)$] suppression factor $G(S_m)$ has been introduced empirically into transport simulations to obtain better agreement with experiment[19-22]. Such magnetic shear stabilization could be related to the dependence of the itg thermal diffusivity on magnetic field[23] and/or to the predicted[45] reduction in the heat diffusivity of high radial itg modes with increasing magnetic shear. Thus, the *ExB* flow and magnetic shear-suppressed ion thermal diffusivity due to itg modes can be represented as[19]

$$\overset{\circ}{\chi}_i^{itg} = G(S_m)\chi_i^{itg} = G(S_m)F_s^{itg}\left(\omega_{ExB}\right)\chi_i^{itg} \tag{24}$$

In this work, we follow Ref. 21 in using $G(S_m) = S_m^{-1.8}$ to represent the additional magnetic shear-suppression.

3. *Drift Alfven modes*

Drift Alfven (da) instabilities are driven by collisions and hence become important in the more collisional edge plasma. Numerical modeling[25] indicates that ExB shear alone can not stabilize these modes (low collisionality and a steep pressure gradient are also needed). An analytical model[26] which takes these effects into account yields the expression

$$\chi_i^{da} = \chi_i^{gb}\overline{\overline{\chi}}_\perp\left(\beta_{\mathrm{P}}, \nu_n\right)/\sqrt{\mu} \tag{25}$$

where the ion gyro-Bohm thermal conductivity is $\chi_i^{gb} = \rho_s^2 c_s / L_{pi}$, with $L_{pi} \equiv -p_i/(dp_i/dr)$,

$$\mu = -k_{\mathrm{P}} L_{pi}\sqrt{m_i T_e / m_e T_i}\ ;\ -\frac{L_{pi}}{qR}\sqrt{m_i T_e / m_e T_i} \tag{26}$$

for k_{P} ; $1/qR$, and

$$\overline{\overline{\chi}}_\perp = \left[\frac{\left(1+\beta_n^2\right)^{-3} + \nu_n^2}{1+\beta_n^2 + \nu_n^{4/3}}\right]^{1/2} \tag{27}$$

where

$$\beta_n \equiv \left(\frac{m_i}{m_e}\right)^{1/2}\beta\frac{qR}{L_{pi}},\quad \beta = \frac{n_e T_e}{B^2/2\mu_0},\ \nu_n \equiv \left(\frac{m_i}{m_e}\right)^{1/4}\frac{\left(qRL_{pi}\right)^{1/2}}{\lambda_e} \tag{28}$$

with $\lambda_e = \upsilon_{the}/\nu_{ei}$ being the electron mean free path.

4. *Thermal instabilities*

In the weak ion-electron equilibration limit, local radial thermal instabilities in the edge ion and electron energy balances are decoupled, and the linear growth rates may be written in the general form[27]

$$\gamma = -\frac{2}{3}\left(\chi_0\left(\nu L_T^{-2} + k_r^2\right) + \frac{5}{2}\nu\frac{\Gamma_\perp}{n}L_T^{-1} - \alpha\right) \tag{29}$$

where the first two terms represent the generally stabilizing effect of heat conduction and convection, respectively, with L_T^{-1} = (-dT/dr)/T for the species in question, $\Gamma_\perp$ being the ion or electron particle flux, and ν characterizing the temperature dependence of the underlying thermal conductivity for that species, $\chi_0 \sim T^\nu$. We use $\nu = 2.5$, but the results are relatively insensitive to this value. (There is a similar result in the strong equilibration limi[27].) The α-terms represent the generally destabilizing atomic physics and impurity cooling terms in the respective growth rates for the ions

$$\alpha_i = \frac{5}{2}(\nu-1)\nu_{ion} + \frac{3}{2}\nu_{at}^c\left(\nu - \left[1 + \frac{T_i}{\nu_{at}^c}\frac{\partial \nu_{at}^c}{\partial T_i}\right]\right) - \frac{1}{n}\left(\nu\frac{H_i}{T_i} - \frac{\partial H_i}{\partial T}\right) \tag{30a}$$

and for the electrons

$$\alpha_e = n_z\left(\frac{\nu L_z}{T_e} - \frac{\partial L_z}{\partial T_e}\right) + \nu_{ion}\left\{\frac{5}{2}(\nu-1) + \nu\frac{E_{ion}}{T_e} - \left(\frac{3}{2} + \frac{E_{ion}}{T_e}\right)\frac{T_e}{\nu_{ion}}\frac{\partial \nu_{ion}}{\partial T_e}\right\} - \frac{1}{n}\left(\nu\frac{H_e}{T_e} - \frac{\partial H_e}{\partial T_e}\right) \tag{30b}$$

The terms ν_{ion} and ν_{at} are the neutral ionization frequency in the pedestal region and the frequency of charge-exchange plus elastic scattering events involving 'cold' neutrals that have not previously undergone such an event in the pedestal region. E_{ion} is the ionization energy, and n_z and L_z are the density and radiative emissivity of impurities in the edge pedestal region. H represents any additional heating or cooling in the pedestal.

A mixing length estimate of the transport associated with such thermal instabilities (ti) is

$$\chi_{i,e}^{ti}\ ;\ \gamma_{i,e}k_r^{-2} \tag{31}$$

In the numerical evaluation, we use the neoclassical and paleoclassical values of the ion and electron thermal diffusivities to evaluate the "background" χ_0 in Eq. (29). When the calculated growth rate is negative, the thermal instabilities are not present.

Electron transport

1. Paleoclassical

Callen's model[28] based on classical electron heat conduction along field lines and magnetic field diffusion in which the electron temperature equilibrates within a distance L along the field lines and in which radially diffusing field lines carry this equilibrated temperature with them and thus induce a radial electron heat transport $M\ ;\ L/\pi qR:$ 10 times larger than the resistive magnetic field diffusion rate leads to the following paleoclassical (paleo) expression for the electron heat diffusivity

$$\chi_e^{paleo} = 1.5(1+M)\frac{\eta_P^{nc}}{\eta_0}\nu_e\delta_e^2 \tag{32}$$

Taking L as the minimum of the electron collision mean free path or the maximum half length of the helical field results in

$$M = \frac{1/\pi Rq}{1/1_{\max} + 1/\lambda_e} \tag{33}$$

where

$$\delta_e^2 \nu_e = \frac{1.4x10^3 Z_{eff}}{T_e^{3/2}(eV)}\left(\frac{\ln\Lambda}{17}\right), \quad \delta_e = c/\omega_{pe}, \ ,$$

$$l_{\max} \equiv \frac{\pi R q_*}{\left(\pi \bar{\delta}_e \frac{dq}{d\rho}\right)^{1/2}} = \frac{R\sqrt{\pi q}}{\left(\frac{\delta_e}{a}\left(\frac{1}{q}\frac{dq}{d\rho}\right)\right)^{1/2}},$$

$$\frac{\eta_{\mathrm{P}}^{nc}}{\eta_0} = \left[\frac{\sqrt{2}+Z_{eff}}{\sqrt{2}+13Z_{eff}/4}\right] + \left[\frac{\sqrt{2}+Z_{eff}-\ln(1+\sqrt{2})}{Z_{eff}\left(1+\nu_{*e}^{1/2}+\nu_{*e}\right)}\right]\frac{(1-f_c)}{f_c},$$

$$f_c \ ; \ \frac{\left(1-\varepsilon^2\right)^{-1/2}(1-\varepsilon)^2}{1+1.46\varepsilon^{1/2}+0.2\varepsilon}$$

$$\nu_{*e} = Rq/\varepsilon^{3/2}\lambda_e, \ \lambda_e = \frac{1.2x10^{16}T_e^2(eV)}{n_e Z_{eff}}\left(\frac{17}{\ln\Lambda}\right) \tag{34}$$

The quantity f_c is the fraction of circulating particles, and $f_{tr} = 1 - f_c$ is the trapped fraction. The paleoclassical transport phenomena are always present and are believed to constitute an irreducible minimum level of electron transport[28].

The paleoclassical heat transport is not in the conventional form $q_e = -n_e \chi_e \nabla T_e$ of conductive heat transfer that is used to infer $\chi_e^{\exp}$. An alternative form[29] of the effective paleoclassical thermal diffusivity can be constructed using the paleoclassical heat transport operator in analogy to the procedure used to construct $\chi_e^{\exp}$

$$\left(\chi_{ePB}^{paleo}\right)_{eff} = \frac{P_e^{paleo}(\rho)}{n_e T_e \frac{V'}{\left(\bar{a}\right)^2} a L_{Te}^{-1}} \tag{35}$$

where $\bar{a} = a\left(2\kappa^2/1+\kappa^2\right)$,

$$P_e^{pc}(\rho_i) = -\int_0^{\rho_i} d\rho (1+M)\frac{\partial^2}{\partial\rho^2}\left(V'\frac{D_\eta}{\left(\bar{a}\right)^2}\frac{3}{2}nT\right) \equiv -\int_0^{\rho_i} d\rho (1+M)\frac{\partial^2}{\partial\rho^2}\left(\rho \mathbb{D}_\eta \frac{n}{T^{1/2}}\right) \tag{36}$$

is the radial paleoclassical heat flow through the flux surface at $\rho = r/a$,

$$D_\eta = \frac{1400 Z_{eff}}{T_e^{3/2}}\left(\frac{\ln\Lambda}{17}\right)\frac{\eta_{\mathrm{P}}}{\eta_0} \tag{37}$$

is the magnetic field diffusivity, and $V' = (2\pi a)^2 \kappa R \rho\left(1+\frac{1}{2}\rho\frac{\partial \ln\kappa}{\partial\rho}\right)$.

2. *Electron temperature gradient modes*

The electron temperature gradient (etg) modes are electrostatic drift waves with $k_\perp c_s \le \omega_{pe}$. The threshold electron temperature gradient for the linear destabilization of etg modes has been established from linear toroidal gyrokinetic simulations[11]

$$\left(\frac{R}{L_{Te}}\right)_{\text{crit}} = \max\begin{bmatrix} 0.8\, R/L_{ne}\,, or \\ (1+\tau)\left(1.33+1.91\frac{r}{q^2}\frac{dq}{dr}\right)(1-1.15\varepsilon) \end{bmatrix} \tag{38}$$

For $R/L_{Te} < (R/L_{Te})_{crit}$, the toroidal etg modes are linearly stable, but for $R/L_{Te} > (R/L_{Te})_{crit}$ the modes would be expected to exist and produce transport.

A simple expression for the thermal conductivity due to the etg modes is given by[9]

$$\chi_e^{etg} = 0.13\left(\frac{c_s}{\omega_{pe}}\right)^2 \frac{\upsilon_{the} S_m}{qR}\eta_e(1+\eta_e) \tag{39}$$

where $S_m \equiv (r/q)(dq/dr)$ is the magnetic shear and ω_{pe} is the electron plasma frequency.

The short-wavelength etg modes are not thought to be strongly affected by *ExB* flow shear[19]. However, shear also produces a shift of the drift wave eigenmodes off the rational surface and a twisting of mode structure, which suppresses the turbulent transport due to etg modes[30]. This suppression can be represented by the multiplicative suppression factor[19,30]

$$F_s^{etg} = \frac{1}{1+\left(Y_s^{etg}\right)^2}, \qquad Y_s = \sqrt{\frac{m_i}{T_e}}\left|\frac{R\frac{\partial}{\partial r}\left(\frac{E_r}{RB_\theta}\right)}{\frac{1}{q}\frac{\partial q}{\partial r}}\right| \tag{40}$$

and the shear-suppressed etg mode thermal diffusivity can be represented as

$$\chi_e^{etg} = F_s^{etg}\chi_e^{etg} \tag{41}$$

A recent development by Horton et al.[13] includes the magnetic shear suppression directly in the derivation

$$\begin{aligned} \chi_e^{etg} &= C_e^{es} q^2 \left(\frac{R}{L_{Te}}\right)^{3/2}\left(\frac{\rho_e^2 \upsilon_{the}}{T_e}\right)\left[-\nabla T_e - 1.88\left(\frac{|S_m| T_e}{qR}\right)\left(1+Z_{eff}\frac{T_e}{T_i}\right)\right], \quad 1_{c,e}^{es} \ge \delta_e \\ &= C_e^{es}\left(\frac{c^2}{\omega_{pe}^2}\right)\left(\frac{\upsilon_{the}}{\sqrt{RL_{Te}}}\right), \quad 1_{c,e}^{es} < \delta_e \end{aligned} \tag{42}$$

where C_e^{es} is a parameter, interpreted as the fraction to which the turbulence reaches the unsuppressed level, which must be fitted to match experimental data (Horton, et al.[13] found $C_e^{es} \approx 0.03$ for Tore Supra, and Bateman, et al[31]. use $C_e^{es} \approx 0.06$ in their Multimode transport model), $1_{c,e}^{es} = q\rho_e R / L_{Te}$, and δ_e is the collisionless skin depth.

3. *Trapped Electron Modes*

The principal electron drift instabilities with $k_\perp c_s \le \Omega_i$ arise from trapped particle effects when $\nu_e^* \equiv \nu_e / \left(\upsilon_{the}/qR\right)\varepsilon^{3/2} < 1$. In more collisional plasmas the mode becomes a collisional drift wave destabilized by passing particles. A simple expression for the electron heat diffusivity associated with electron trapping was given by Kadomtsev and Pogutse[32] based on the improved mixing length estimate $\chi \approx \left(\gamma^3/k_{tem}^2\right)/\left(\gamma^2+\omega_r^2\right)$

$$\chi_e^{tem} = \frac{f_{tr}\eta_e\rho_i^2\omega_{*e}^2(\nu_e/\varepsilon)}{\omega_{*e}^2+\left(\nu_e/\varepsilon\right)^2} \tag{43}$$

where $k_{tem} \approx 1/\rho_i$, the value of the tem k-value for which the maximum growth rate occurs, has been used.

Weiland[15] considers a reactive trapped electron mode which is almost symmetric to the itg mode leading to the transport given by Eqs. (12). The improved mixing length quasilinear estimate of the effective electron heat diffusivity of this coupled tem is

$$\left(\chi_e^{tem}\right)_{eff} = \frac{f_{tr}}{\eta_e}\left[\eta_e - \frac{2}{3} - \frac{2}{3}\Delta_e\right]\frac{\gamma^3/k^2}{\left(\omega_r - \frac{5}{3}\omega_{De}\right)^2+\gamma^2} \tag{44}$$

where

$$\Delta_e = \frac{1}{N}\left\{\begin{array}{l} \left|\mathcal{U}\right|^2\left[\begin{array}{l}\left|\mathcal{U}\right|^2\left(\varepsilon_n-1\right)+\mathcal{U}_r\varepsilon_n\left(\frac{14}{3}-2\eta_e-\frac{10}{3}\varepsilon_n\right)+ \\ \frac{5}{3}\varepsilon_n^2\left(-\frac{8}{3}+3\eta_e+\frac{2}{3}\varepsilon_n\right)\end{array}\right] \\ -\frac{50}{9}\mathcal{U}_r\varepsilon_n^3\left(1-\varepsilon_n\right)+\frac{25}{9}\left(\frac{7}{3}-\eta_e-\frac{5}{3}\varepsilon_n\right)\end{array}\right\} \tag{45}$$

and the other quantities are defined above in the section on itg modes.

The tem's are longer wavelength modes coupled to the itg modes and should be suppressed by *ExB* flow shear in the same way as the itg modes, so that the *ExB* shear-suppressed thermal diffusivity due to tem's can be represented as[19]

$$\mathcal{U}\chi_e^{tem} = F_s^{itg}\chi_e^{tem} \tag{46}$$

and the further magnetic suppression is represented as for the itg modes

$$\overset{\circ}{\chi}{}_e^{tem} = G\left(S_m\right)\mathcal{U}\chi_e^{tem} = G\left(S_m\right)F_s^{itg}\left(\omega_{ExB}\right)\chi_e^{tem} \tag{47}$$

4. *Drift Resistive Ballooning Mode*

The drift-resistive ballooning (drb) mode is destabilized by unfavorable curvature on the outboard side of the torus in a collisional edge plasma. Linear stability analysis[33] indicates that the transport associated with these modes can be characterized by a particle

diffusion coefficient scaling $D: \left(2\pi q\right)^2 \rho_e^2 \nu_{ie} \left(R/L_n\right)$ with a proportionality constant equal to the flux surface average of the normalized fluctuating radial particle flux $\langle nV_r \rangle$. Subsequent calculations[34] found robust growth rates of drb modes for the edge parameters of DIII-D and predicted the normalized fluctuating radial particle fluxes for models representative of DIII-D core parameters $\langle nV_r \rangle \approx 0.01\text{-}0.05$. We adopt the form

$$\chi_e^{drb} = 4\frac{R}{L_n}\left(q\rho_e\right)^2 \nu_e \tag{48}$$

with the normalization factor equal to 4 to characterize the transport of electron energy due to drift-resistive ballooning modes, with the caveat that there could well be an additional normalization constant needed. We note that one group of transport modelers[36] calibrated this formula to L-mode data and found a factor of $94\kappa^{-4}$ (instead of 4) should multiply this expression (κ is the elongation), while another group[16] used this expression with the factor of 4.

The *ExB* flow shear suppression for drb modes is represented[19] by the multiplicative factor

$$F_s^{drb} = \frac{1}{1+\left(Y_s^{drb}\right)^2}, \quad Y_s^{drb} = \omega_{ExB}\tau_{drb} = \omega_{ExB}\left(\frac{L_{drb}^2}{\chi_e^{drb}}\right), \quad L_{drb} = 2\pi q\left[\frac{2ne^2\eta_{\mathrm{P}}\rho_i}{m_e\Omega_e\sqrt{2RL_n}}\right] \tag{49}$$

where the expression for the correlation length (turbulence characteristic scale length) L_{drb} is taken from Ref. (36). The *ExB* shear-suppressed thermal diffusivity is then represented as

$$\chi_e^{\mu drb} = F_s^{drb}\chi_e^{drb}. \tag{50}$$

and the additional magnetic shear suppression is represented by

$$\chi_e^{\circ drb} = G\left(S_m\right)\chi_e^{\mu drb} = G\left(S_m\right)F_s^{drb}\chi_e^{drb} \tag{51}$$

5. *Resonant Magnetic Perturbation Diffusion*

When the I-coil is turned on (in DIII-D) there is a resonant magnetic perturbation in the plasma edge in DIII-D. A magnetic field line integration code[37] is used to numerically calculate the magnetic diffusivity D_m across the outer region of the plasma where resonant magnetic perturbations from the DIII-D I-coil are expected to produce a significant level of stochasticity. The magnetic diffusivity of a field line is defined as:

$$D_m = \delta r^2/2L \tag{52}$$

where δr is the total radial displacement, calculated at the outboard midplane, between the starting point of the field line calculation and its end point. Here, L is the total parallel field line length from the starting point to the end point. Since the DIII-D version of the field line integration code calculates trajectories in poloidal flux space (ψ), an average D_m^{ψ} taken over an ensemble of N starting points on a single flux surface is determined on each flux surface based on the diffusion field lines in flux space using:

$$\left\langle D_m^{\psi}\right\rangle = \frac{1}{N}\sum_{j=1}^{N}\delta\psi_j^2\big/2L_j \tag{53}$$

where $\delta\psi_j$ is the total displacement of a single field line in poloidal flux and L_j is its total parallel length. As discussed in Ref. [38], $\left\langle D_m^{\psi}\right\rangle$ is converted to real space variables $\left\langle D_m^{r}\right\rangle$ with units of meters using a geometric factor that accounts for the shape of the flux surface. Then, an average stochastic magnetic electron thermal diffusivity $\left\langle \chi_{e-m}^{r}\right\rangle$ in units of m^2/s is calculated using:

$$\left\langle \chi_{e-m}^{r}\right\rangle = \mathrm{v}_{the}\left\langle D_m^{r}\right\rangle \tag{54}$$

where v_{the} is the electron thermal speed on the starting flux surface. The code is typically set to calculate $N=180$ poloidally distributed, equally spaced, field line trajectories on each flux surface and follows each field line until it either hits a solid surface or makes 200 toroidal revolutions. A field line escape fraction f_{esc}, the ratio of field lines hitting a solid surface to the number of field lines started on each flux surface N, is calculated on each flux surface and a weighted $\left\langle \chi_{e-m}^{r}\right\rangle_w$ is calculated using:

$$\left\langle \chi_{e-m}^{r}\right\rangle_w = f_{esc}\left\langle D_m^{r}\right\rangle \tag{55}$$

C. Evaluation of experimental heat diffusivities

Since the total ion and electron heat fluxes, $Q_{i,e}$, consist of a conductive component $q_{i,e} = -\chi_{i,e} n \nabla T_{i,e} = \chi_{i,e} n T_{i,e} L_{Ti,e}^{-1}$ plus a convective component $5/2\Gamma_{i,e}T_{i,e}$, values for the radial thermal diffusivities can be inferred from the experimental density and temperature profiles using[2-5]

$$\chi_{i,e}^{\exp}(r) = L_{Ti,e}(r)\frac{q_{i,e}(r)}{n_{i,e}(r)T_{i,e}(r)} \equiv L_{Ti,e}(r)\left[\frac{Q_{i,e}(r)}{n_{i,e}(r)T_{i,e}(r)} - \frac{5}{2}\frac{\Gamma_{i,e}(r)}{n_{i,e}(r)}\right] \tag{56}$$

where $L_{Ti,e}^{-1} \equiv -\left(\partial T_{i,e}/\partial r\right)/T_{i,e}$, $Q_{i,e}$ are the total heat fluxes, which satisfy

$$\frac{\partial Q_i}{\partial r} = -\frac{\partial}{\partial t}\left(\frac{3}{2}n_i T_i\right) + q_{nbi} - \frac{3}{2}\left(T_i - T_o^c\right)n_i n_o^c\left\langle \sigma\upsilon\right\rangle_{cx+el} - q_{ie}\ ,\ Q_i\left(r_{sep}\right) = Q_{sepi}^{\exp} \tag{57}$$

and

$$\frac{\partial Q_e}{\partial r} = -\frac{\partial}{\partial t}\left(\frac{3}{2}n_e T_e\right) + q_{nbe} + q_{ie} - n_e n_o\left\langle \sigma\upsilon\right\rangle_{ion} E_{ion} - n_e n_z L_z\ ,\ Q_e\left(r_{sep}\right) = Q_{sepe}^{\exp} \tag{58}$$

and $\Gamma_{i,e} \equiv n_{i,e}\upsilon_{ri,e}$ is the radial particle flux, which satisfies

$$\frac{\partial \Gamma_i}{\partial r} = -\frac{\partial n_i}{\partial t} + n_e n_o\left\langle \sigma\upsilon\right\rangle_{ion} + S_{nb}\ ,\ \ \Gamma_i\left(r_{sep}\right) = \Gamma_{sepi}^{\exp} \tag{59}$$

In these equations, n_o is the recycling or gas fueling neutral density in the edge pedestal (the superscript "c" denotes uncollided "cold" neutrals), $q_{nbi,e}$ is the neutral beam heating, S_{nb} is the neutral beam particle source, q_{ie} is the collisional energy transfer from ions to electrons, $\left\langle \sigma\upsilon\right\rangle_x$ is an atomic physics reaction rate (x=cx+el denotes charge-exchange

plus elastic scattering, $x=ion$ denotes ionization), n_z and L_z are the impurity density and radiation emissivity, and E_{ion} is the ionization potential. The atomic physics data are taken from Ref. 39, and the radiation emissivity is calculated from a fit to coronal equilibrium calculations (taking into account the effect of charge-exchange and recombination in the presence of recycling neutrals) based on the data given in Ref. 40.

The experimental heat diffusivity of Eq. (56) is the proper quantity to compare with theoretical predictions of the actual conductive heat diffusivity, such as the neoclassical prediction of Eq. (1). However, many of the expressions for the heat diffusivities due to turbulence were constructed by dividing the theoretical expression for the total ion or electron heat flux due to turbulence by the corresponding temperature gradient and density (i.e. the total heat flux was effectively assumed to be conductive, and any convective heat flux was neglected). Such theoretical expressions should probably be compared with an effective experimental heat diffusivity constructed in a similar fashion

$$\left(\chi_{i,e}^{\exp}\right)_{eff} = L_{Ti,e}(r)\frac{Q_{i,e}(r)}{n_{i,e}(r)T_{i,e}(r)} \tag{60}$$

This effective quantity should be interpreted as just what it is, a ratio of total heat flux to the product of the density and the temperature gradient, and not attributed any physical significance as a "heat diffusivity".

An integrated modeling code[41] was used to i) calculate particle and power balances on the core plasma in order to determine the net particle and heat outfluxes from the core into the scrape-off layer (SOL), which are input to ii) an extended 2-point divertor plasma model (with radiation and atomic physics) that calculated densities and temperatures in the SOL and divertor and the ion flux incident on the divertor plate, which iii) was recycled as neutral atoms and molecules that were transported through the 2D divertor region across the separatrix to fuel the core plasma.

Equations (57)-(59) were integrated over the edge region to calculate the heat and particle flux profiles, using the experimental density and temperature profiles. The separatrix boundary conditions on the particle and heat fluxes were the "steady-state" experimental values determined from the integrated modeling code. The time derivative terms were evaluated from experimental data to account for plasma heating, etc. The heat and particle fluxes calculated from Eqs. (57)-(59) were then used, together with the experimental density and temperature profiles, to infer the experimental thermal diffusivities from Eq. (56). The details of this procedure and the uncertainties in the resulting experimental thermal diffusivities are described in previous papers[2-5].

D. DIII-D Shots 119436 and 118897

Two DIII-D shots for which detailed data analysis had been previously performed[4,5] were selected for comparison of theoretically predicted and experimentally inferred heat diffusivities. In both shots the experimental data were analyzed over about the outer 15% of the plasma radius, including both the steep-gradient edge pedestal region and the relatively flat density and temperature "flattop" region just inside the edge pedestal. Both shots were lower single null divertor configuration with neutral beam heating.

Shot 119436 was an ELMing H-mode shot with a global steady state phase, which was analyzed. To reduce the influence of any random measurement errors, the time interval between ELMs was divided into 5 time bins, and data was collected from a sequence of inter-ELM time intervals and averaged, as indicated in Figs. 1 and described in detail in Ref. 5. The data in the time bin just before an ELM crash was chosen for the analyses of this paper. The main parameters were B = -1.64 T, I = 0.99 MA, R = 1.77 m, a = .58 m, κ = 1.83. The time 3250 ms was chosen for analysis. At this time the neutral beam power was 4.3 MW, the gas fueling rate was 0 atoms/s, the line average density was $\bar{n} = 4.2\text{x}10^{19}/\text{m}^3$, and the safety factor was $q_{95} = 4.2$. The parameters at the top of the edge pedestal were $n_{ped} = 1.8x10^{19}/m^3, \text{T}^i_{ped} = 731V, T^e_{ped} = 900eV$.

Shot 118897 had an ELM-free L-mode and H-mode phase, both of which were analyzed for this paper. The edge density and temperature measurements for three times in the ELM-free phase of this shot are shown in Figs. 2. The main parameters were B = -1.98 T, I = 1.39 MA, R = 1.71 m, a = .60 m, κ = 1.82. The L-H transition occurred shortly after the time, 1525ms, chosen for analysis of the L-mode. At this time the neutral beam power was 4.45 MW, the gas fueling rate was $6.2\text{x}10^{19}$ atoms/s, the line average density was $\bar{n} = 3.2\text{x}10^{19}/\text{m}^3$, and the safety factor was $q_{95} = 3.52$. The parameters at the top of the edge pedestal were $n_{ped} = 1.16x10^{19}/m^3, \text{T}^i_{ped} = 200eV, T^e_{ped} = 50eV$. The time chosen for the H-mode analysis, 2140 ms, was well after the L-H transition and before the first ELM occurred. At this time the neutral beam power was 2.33 MW, the gas fueling rate was $2.5\text{x}10^{19}$ atoms/s, the line average density was $\bar{n} = 7.7\text{x}10^{19}/\text{m}^3$, and the safety factor was $q_{95} = 3.70$. The parameters at the top of the edge pedestal were $n_{ped} = 8.03x10^{19}/m^3, \text{T}^i_{ped} = 694eV, T^e_{ped} = 524eV$.

The data analysis procedure is described in Refs. 4 and 5. The details of the data interpretation procedure described in the previous section for these shots are also described in Refs. 4 and 5, where uncertainties in the evaluation of thermal diffusivities from the measure density and temperature profiles and the treatment of transisient conditions are also discussed in detail.

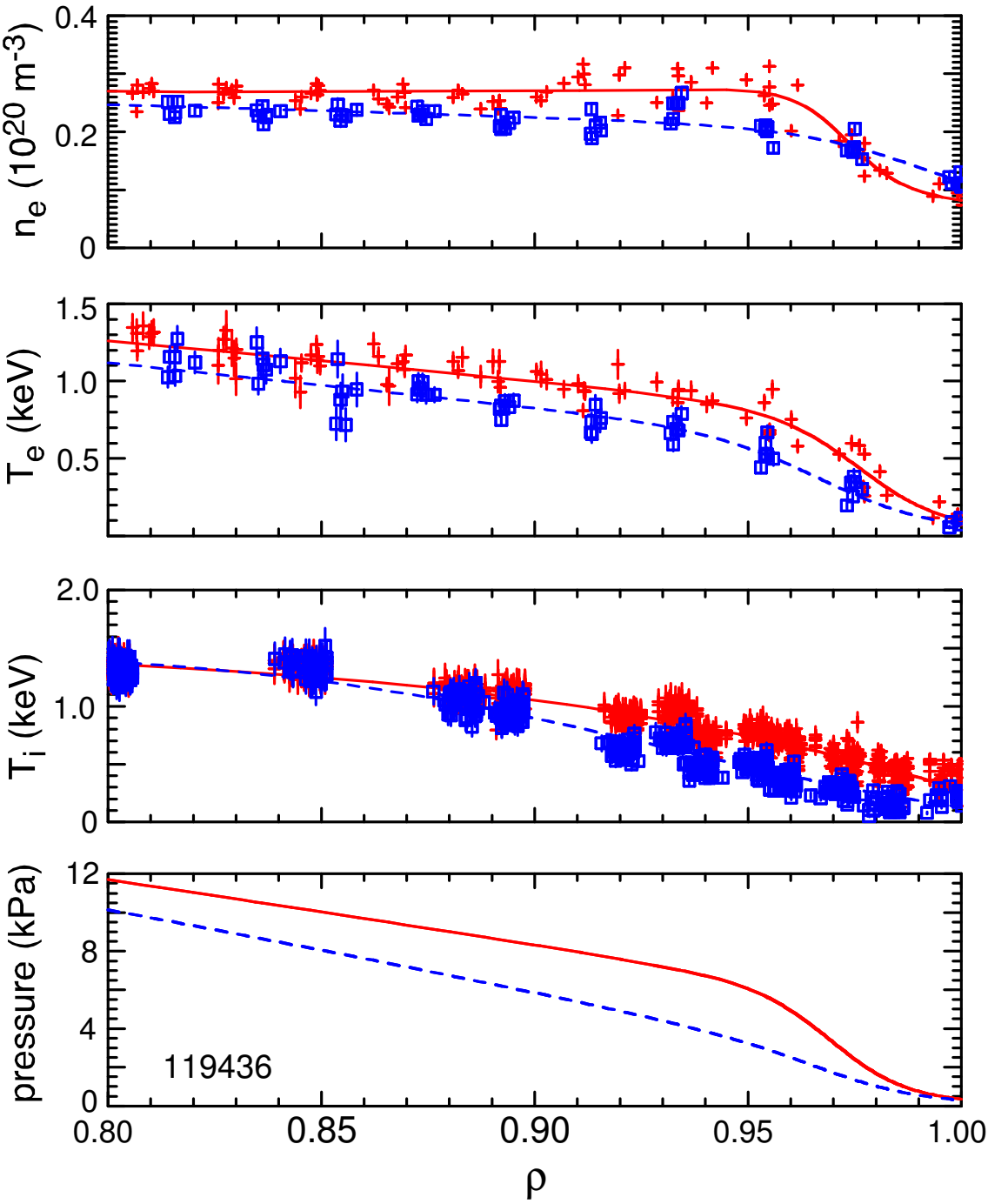

Fig. 1 Density, temperatures and pressure in edge region of DIII-D shot 119436 (squares=data 10-20% after ELM crash, +=data 80-99% after ELM crashes used in the analyses of this paper, dashed line=fit 10-20% after ELM crash, solid line=fit 80-99% after ELM crashes) ρ= normalized radius[5].

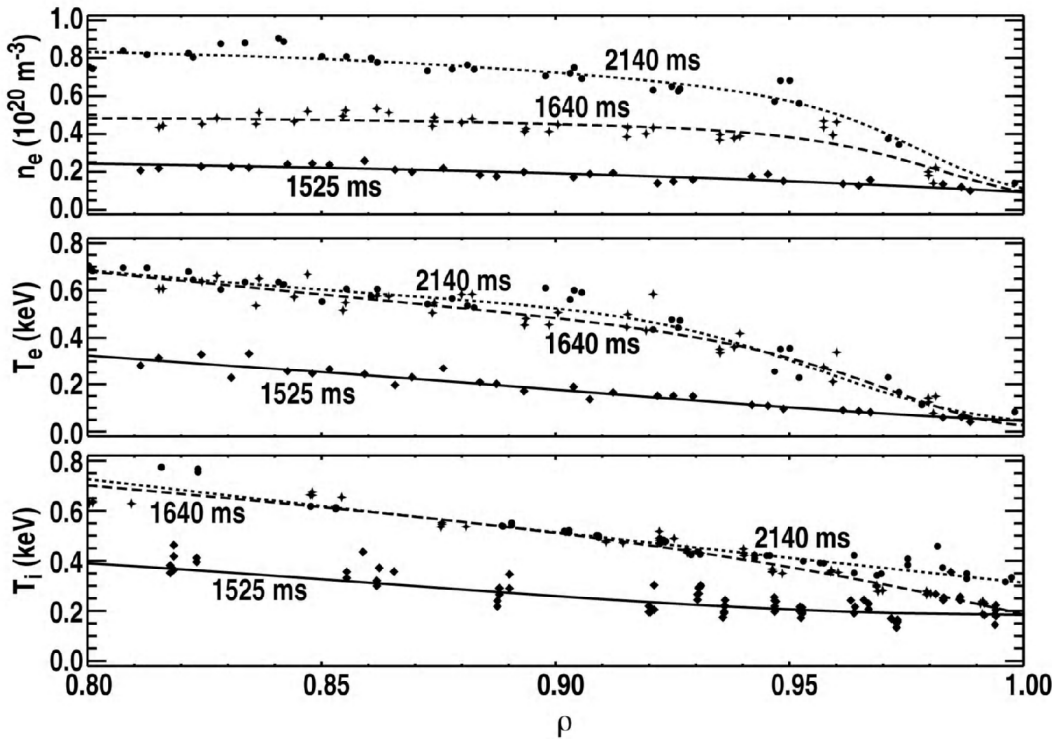

Figure 2. Measured and fitted densities and temperatures in the edge of DIII-D shot 118897 during the ELM-free phase[4]. (L-H transition took place just before 1640 ms).

Comparison of theoretical and experimental heat diffusivities

1. Transport parameters

Various parameters which affect the theoretical transport predictions are shown in Figs. 3. Shot 119436 was the least collisional, with the collisionality parameter ν_{ei}^* varying monotocally from about 0.1 in the inner flattop region (at ρ ; 0.86) to about 3.0 just inside the separatrix (at $\rho = 1$). For the H-mode phase of shot 118897 the corresponding variation in ν_{ei}^* was from about 0.8 to about 20, and for the L-mode phase of shot 118897 the corresponding variation in ν_{ei}^* was from about 1.1 to about 25.

The parameter $\eta_{i,e} \equiv L_n / L_{Ti,e} \equiv (-dn/ndr)/(-dT_{i,e}/T_{i,e}dr)$ is everywhere greater than unity for electrons in both the L- and H-mode phases of shot 118897 and greater than unity for $\rho > 0.94$ in shot 119436, which is sometimes taken as an indication of the instability of etg modes and the presence of etg transport. This parameter for ions is larger than unity (taken as an indication of the existence of itg transport) for the flattop region but smaller than unity for the steep-gradient pedestal region for both the L- and H-mode phases of shot 118897. The behavior of this parameter in shot 119436 is interesting in that the density profile was actually slightly hollow, inside of $\rho \approx 0.94$, leading to $L_n \equiv -n/(dn/dr) < 0$ over the flattop region. This in turn led

to $\eta_{i,e} \equiv L_n / L_{Ti,e} < 0$ over the flattop region, which in turn led to negative heat diffusivities or other unphysical behavior being predicted by some of the theoretical formulas.

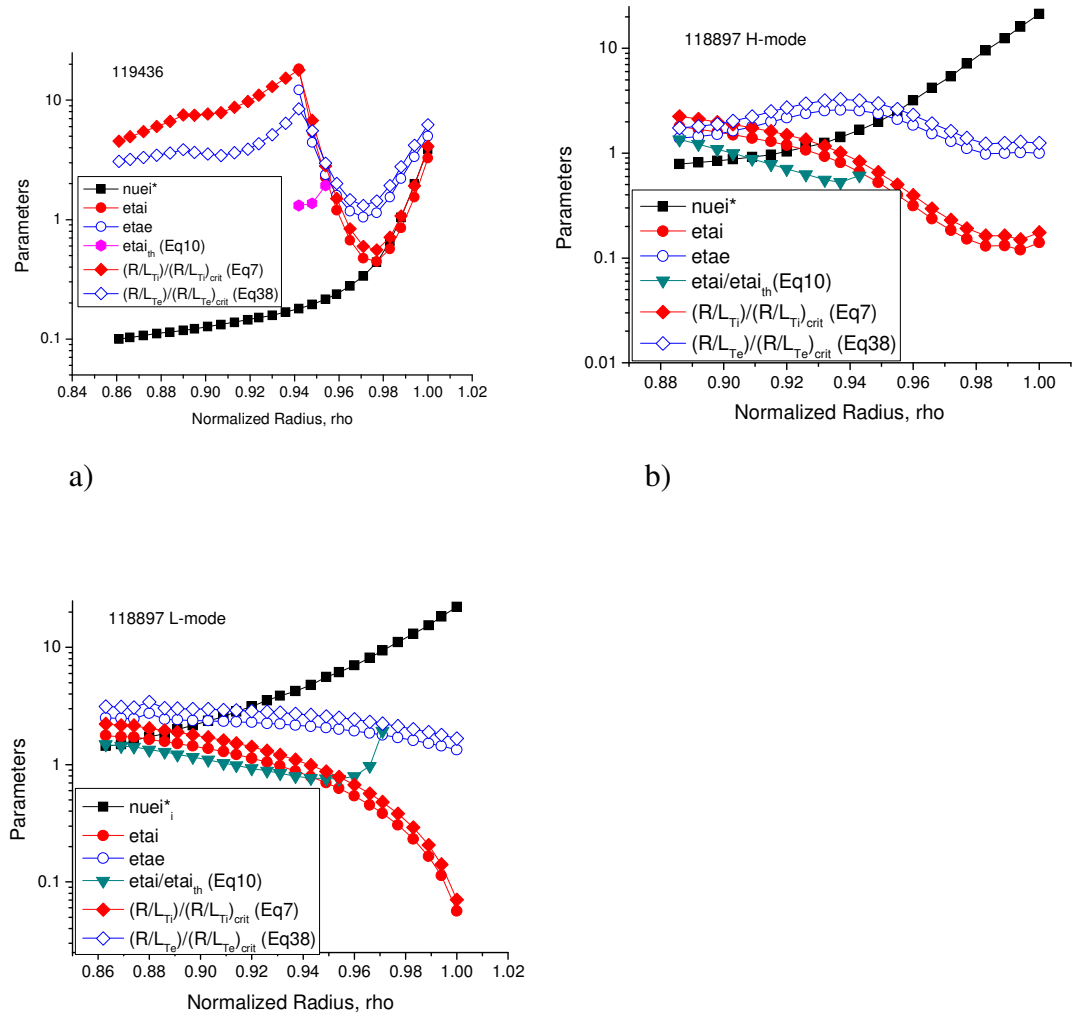

Figure 3 Transport parameters $\nu_{ei}^*, \eta_{i,e} \equiv L_n / L_{Ti,e}, \eta_i / \eta_{ith}, (R/L_{Ti,e}) / (R/L_{Ti,e})_{crit}$ in edge of a) ELMing H-mode shot 119436, b) ELM-free H-mode shot 118897 at 2140ms, c)L-mode shot 118897 at 1525 ms.

The temperature gradient conditions for the onset of etg instabilities (hence the existence of etg transport) given by Eq. (38), $\left(R/L_{Te} > (R/L_{Te})_{crit}\right)$ was satisfied over the entire domain 0.86 < ρ < 1.0 for all three shots. The corresponding condition for the onset of itg instabilities (hence for the existence of itg transport) given by Eq. (7), $\left(R/L_{Ti} > (R/L_{Ti})_{crit}\right)$, was generally satisfied in the flattop region for all shots and just inside the separatrix for shot 119436, but was not satisfied in general in the steep-gradient edge pedestal region.

The evaluation of the instability threshold condition for itg-tem modes in the Weiland model, Eq. (10), yielded essentially the same results as the $\left(R/L_{Ti,e} > \left(R/L_{Ti,e}\right)_{crit}\right)$ criteria for the L- and H-mode phases of shot 118897. However, the evaluation of Eq. (10) for shot 119436 led to negative values for $\rho \geq 0.96$ and for $\rho \leq 0.94$. The negative values of Eq. (10) for $\rho \geq 0.96$ can be interpreted as itg instability for any $\eta_i > 0$, which then makes the prediction of itg instability and transport for $\rho \geq 0.94$ consistent with the $\left(R/L_{Ti} > \left(R/L_{Ti}\right)_{crit}\right)$ prediction for shot 119436. However, for $\rho \leq 0.94$, the hollow density profile leads also to $\eta_i < 0$, making the evaluation of itg instability and the existence of itg and tem transport from Eq. (10) indeterminate for this model in this region.

The profiles of the safety factor and of the radial electrical field are important for the evaluation of theoretical expressions for the magnetic and *ExB* shear, for the evaluation of the orbit squeezing and loss fraction corrections, and for the evaluation of transport coefficients depending on q. Experimental profiles for these quantities are shown in Figs. 4 and 5. The discontinuous fits to the discrete E_r data points introduces spurious structure into the evaluation of dE_r/dr from the experimental data needed for the *ExB* shear correction factor.

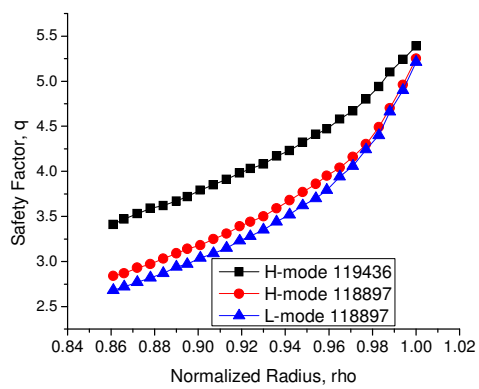

Figure 4 Safety factor in edge plasmas

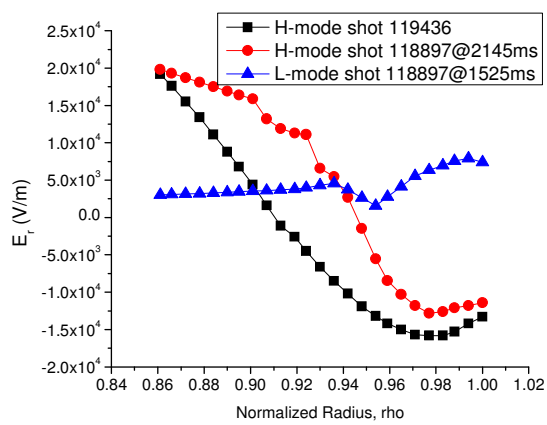

Figure 5 Radial electric field.

2. *Calculation of heat fluxes and inference of heat diffusivities*

The experimental data were used to evaluate the heating and cooling rates and the particle sources in Eqs. (57)-(59) and these equations were integrated inward from experimental separatrix boundary conditions to obtain the total and convective heat fluxes shown in Figs. 6. Details of this procedure are discussed in Refs. 2-5. These heat fluxes were then used, together with the experimental density and temperature data, to evaluate Eqs. (56) and (60) in order to infer the experimental heat diffusivities. We note that a more accurate determination of the experimental time derivatives of density and energy has become available for shot 118897 since Ref. 4 was published, so that the heat fluxes and consequently the inferred experimental heat diffusivities of this paper differ somewhat from those in Ref. 4.

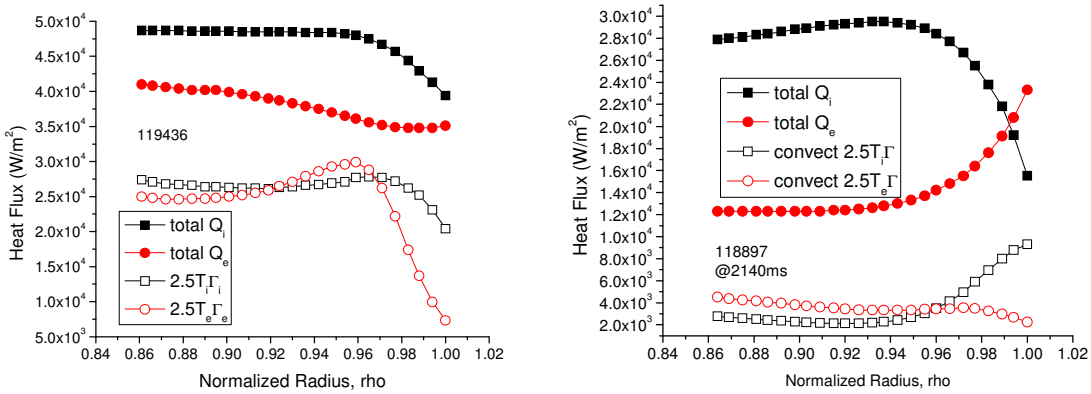

a) b)

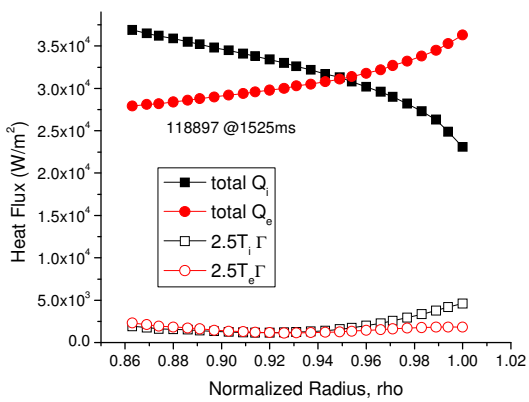

c)

Figure 6 Heat fluxes in DIII-D a) ELMing H-mode shot 119436, b) ELM-free H-mode shot 118897 at 2140ms, c)L-mode shot 118897 at 1525 ms.

As discussed previously, the heat diffusivity is understood as being associated with the conductive heat flux, and Eq. (56) is the consistent relationship for its evaluation. However, since many theoretical expressions for the heat diffusivity are derived by dividing the theoretical prediction for the total heat flux by the temperature gradient (and density), Eq. (60) provides a better quantity for comparison with theory in those cases. In shot 118897 the convective heat flux is relatively small except just inside the separatrix in the H-mode phase, and there is no practical difference between Eqs. (56) and (60), but for H-mode shot 119436, the convective heat flux is substantial over the entire edge region and there is a significant difference between the heat diffusivities inferred from the two equations.

3. Comparison of theoretical and experimental heat diffusivities

A detailed comparison of the predictions of all of the heat diffusivity models of section II with the experimentally inferred heat diffusivities is described in the appendix. This comparison, as it pertains to providing insight as to which heat transport mechanisms are the more promising for explaining the inferred experimental heat

diffusivities, is summarized in this section. When a prediction is shown only over part of the edge region this is because either the existence condition (e.g. Eqs. 7, 10 or 38) is not satisfied, the formula gave unphysical results (e.g. the hollow density profile in the flattop of shot 119436 led to $L_n < 0$ and hence $\eta_{i,e} < 0$, causing predictions of negative heat diffusivities by formulas such as Eq. 39 for etg, Eq. 43 for tem and Eq. 48 for drb), or the evaluation of involved expressions (e.g.. Eqs. 12-19 for itg) simply broke down for the parameters of the plasma edge. These problems are discussed in the appendix.

4. Summary of ion heat diffusivity comparison

A comparison of the ion heat diffusivities predicted by the neoclassical (neo_ch) model, by two of the ion temperature gradient (itg) mode models, and by the drift Alfven (da) model are collected in Figs. 7, where the experimentally inferred heat diffusivities are also shown. Also included is the thermal instability (ti) model prediction for the L-mode phase of shot 118897; the prediction for the H-mode shots was no thermal instability. For shot 119436, two itg mode calculations, Eqs. (8) and (20), are shown, both with *ExB* and magnetic shear suppression. No *ExB* shear suppression is included in the drift Alfven mode calculation (because numerical modeling[25] indicates that it is ineffective) nor, of course, in the neoclassical calculation. It is apparent from Figs. 7a and 7b that some combination of the neoclassical, drift Alfven and the itg heat diffusivities could provide a reasonably good match to the experimental ion heat diffusivity for the two H-mode shots, which suggests that these three ion heat transport mechanisms should receive attention in future investigations. All of the theories substantially underpredict the experimental heat diffusivities in the L-mode shot, except the thermal instability (ti) theory just inside the separatrix where the radiative instability growth rates are the largest.

5. Summary of electron heat diffusivity comparison

A comparison of the electron heat diffusivities predicted by the paleoclassical (paleo) model, by the electron temperature gradient (etg) mode model, by the trapped electron mode (tem) model, and by the drift resistive ballooning mode (drb) model are collected in Figs. 8, where the experimentally inferred heat diffusivities are also shown. The tem and drb heat diffusivities shown for the H-mode shots are *ExB* and magnetic shear suppressed. The paleoclassical prediction is in reasonable agreement with experiment in the flattop region, but overpredicts it in the steep-gradient region, for the H-mode shots (Figs. 8a and 8b). However, the paleoclassical prediction is in excellent agreement with experiment for the L-mode phase of shot 118897 (Fig. 8c). The etg prediction is in reasonable agreement with experiment in both H-mode shots and in the L-mode shot. The tem predictions agree reasonably well in radial profile and magnitude with experiment for the H-mode shots (Figs. 8a and 8b), but substantially underpredict experiment in the L-mode phase of shot 118897 (Fig. 8c). The drb prediction agrees with experiment reasonably well in magnitude but not in radial profile in the steep-gradient edge pedestal region of ELMing H-mode shot 119436 (Fig. 8a), but substantially overpredicts experiment in the same location for the more collisional H-mode phase of shot 118897 (Fig. 8b), and substantially underpredicts experiment in the L-mode phase of

shot 118897 (Fig. 8c). Clearly, the etg, paleoclassical and tem mechanisms should be further investigated for electron transport in the plasma edge.

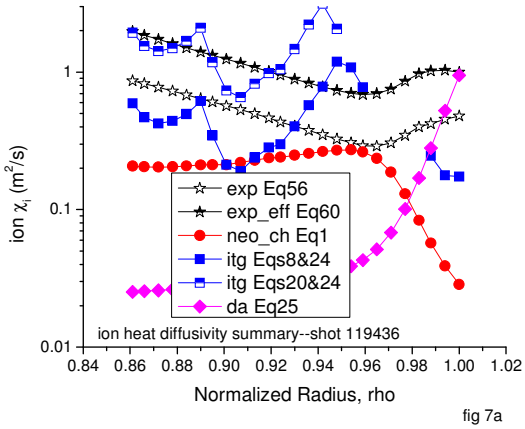

a)

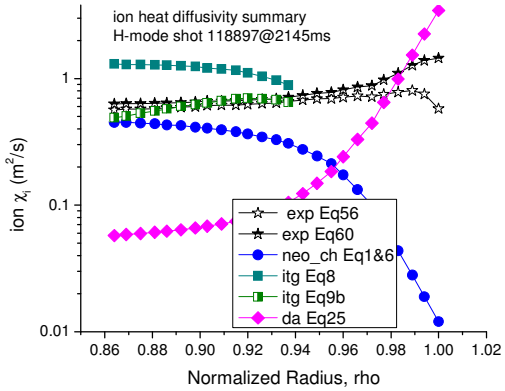

b).

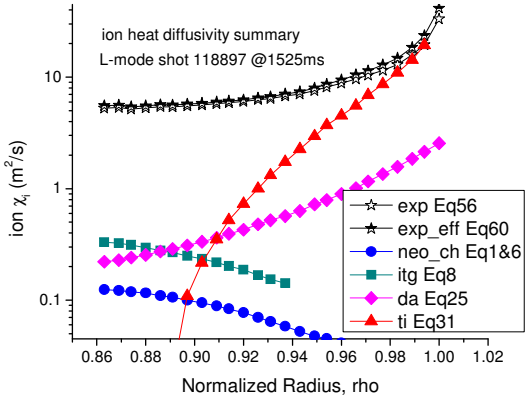

c)

Figure 7 Summary of ion heat diffusivity comparison of theory with experiment for DIII-D a) ELMing H-mode shot 119436, b) ELM-free H-mode shot 118897 at 2140ms, c)L-mode shot 118897 at 1525 ms.

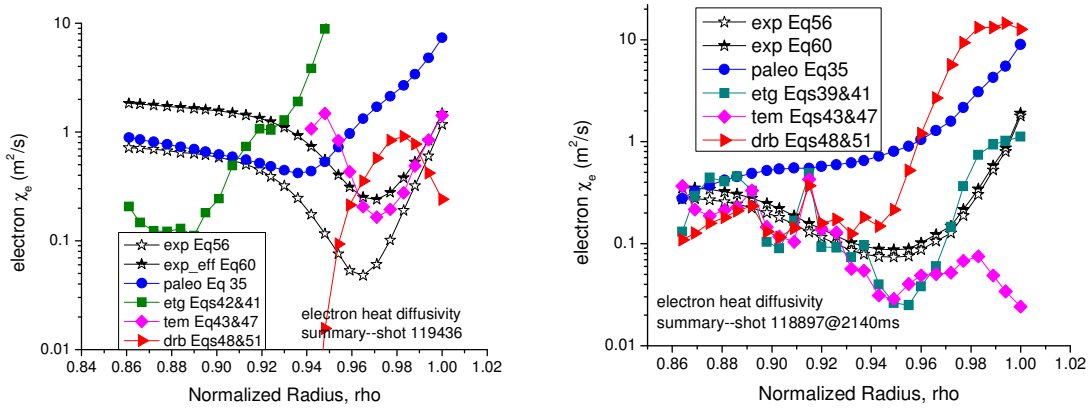

a0 b)

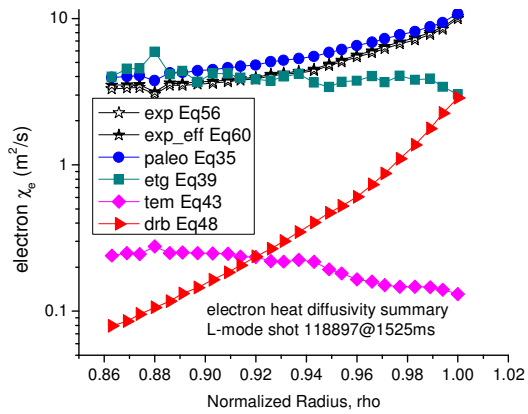

c)

Figure 8 Comparison of theoretical and experimental electron heat diffusivities for DIII-D a) ELMing H-mode shot 119436, b) ELM-free H-mode shot 118897 at 2140ms, c)L-mode shot 118897 at 1525 ms.

E. Summary and conclusions

The predictions of a number of models for the ion and electron heat diffusivity found in the literature and used today in transport codes have been compared with experimentally inferred values of the heat diffusivity for the edge plasma of two H-mode and one L-mode discharges in DIII-D. Models of ion heat diffusivity based on neoclassical, ion temperature gradient, drift Alfven and radiative thermal instability theories, and models of electron heat diffusivity based on paleoclassical, electron temperature gradient, trapped electron, and drift resistive ballooning theories were investigated.

For the L-mode shot, the paleoclassical prediction was in very good agreement with the experimental electron heat diffusivity and the etg prediction was also reasonably good. None of the theoretical predictions for ion heat diffusivity were in agreement with measurements over the entire edge region, althour the radiative thermal instability

prediction just inside the separatrix was in reasonable agreement with the experimental ion heat diffusivity.

For the H-mode shots, the best overall agreement with experiment was found with the itg predictions of ion heat diffusivity. For electron heat diffusivity, the tem prediction was in reasonable agreement for one shot, and the etg predictions was in reasonable agreement for the other.

Acknowledgement

The author expresses his appreciation to the other members of the DIII-D team for the measurement and analysis of the data used in this paper, in particular to Rich Groebner (GA) for providing the fits used in the calculations, for insightful comments on the paper during its development, and for his contributions to the previous development of methodology for experimental interpretation used in this paper. The author is also grateful to several people for taking their time to discuss various aspects of the theoretical models with him: to Jim Callen (Wisconsin) for detailed discussions of his paleoclassical model, to Fred Hinton (GA) for discussion of the neoclassical model, to Glenn Batemen and Alexie Pankin (Lehigh) for discussions of the modeling of various transport mechanisms in the Multi-Mode model, to Jan Weiland (Chalmers) for discussions of his itg/tem model, and to Parvez Gudzar (Maryland) for discussion of his drb model. This work was supported in part by U S Dept. of Energy Grant No. DE-FG02-00-ER54538 with the Georgia Tech Research Corporation.

References

1. J. Luxon, Nucl. Fusion, 42, 614 (2002).
2. W. M. Stacey and R. J. Groebner, Phys. Plasmas, 13, 072510 (2006).
3. W. M. Stacey and T. E. Evans, Phys. Plasmas, 13, 112506 (2006).
4. W. M. Stacey and R. J. Groebner, Phys. Plasmas, 14, 012501 (2007).
5. W. M. Stacey and R. J. Groebner, Phys. Plasmas, 14, 122504 (2007).
6. J. E. Kinsey, R. E. Waltz and J. Candy, Phys. Plasmas, 14, 102306 (2007).
7. C. S. Chang and F. L. Hinton, Phys. Fluids, 25, 1493 (1982).
8. C. S. Chang and F. L. Hinton, Phys. Fluids, 29, 3314 (1986).
9. J. A. Wesson, *Tokamaks,* 2nd ed. (Clarendon Press, Oxford, 1997).
10. K. C. Shaing and R. D. Hazeltine, Phys. Fluids B, 4, 2547 (1992).
11. F. Jenko, W. Dorland and G. W. Hammett, Phys. Plasmas, 8, 4096 (2001).
12. F. Romanelli, W. M. Tang and R. B. White, Nucl. Fusion, 26, 1515 (1986).
13. W. Horton, P. Zhu, G. T. Hoang, T. Aniel, M. Ottaviani and X. Garbet, Phys. Plasmas, 7, 1494 (2000).
14. M. Ottaviani, W. Horton and M. Erba, Plasma Phys. Control. Fusion, 39, 1461 (1997).
15. J. Weiland, *Collective Modes in Inhomogeneous Plasmas*, (Bristol: IOP Publishing) 2000.
16. D. Kalupin, M. Z. Tokar, B. Unterberg, X. Loozen and D. Pilipenko, Nucl. Fusion, 45, 468 (2005).
17. T. S. Halm and K. H. Burrell, Phys. Plasmas, 2, 1648 (1995).
18. P. W. Terry, Rev. Mod. Phys., 72, 109 (2000).

19. A. Y. Pankin, I. Toitsekhovitch, G. Bateman, A. Denestrovski, G. Janeschitz, M. Murakami, T. Osborne, A.H. Kritz, T. Onjun, G. W. Pacher and H. D. Pacher, Plasma Phys. Control. Fusion, 47, 483 (2005).
20. O. V. Zolotukhin, Y. Igitkhanov, G. Pacher, G. Janeschitz and H. Pacher, *28th EPS Conf. on Controlled Fusion and Plasma Physics* (Funchal, Portugal, 2001), IAEA, Vienna, p 677 (2002).
21. G. Janeschitz, G. W. Pacher, O. Zolotukhim, G. Pereverzev, H. D. Pacher, Y. Igitkhanov, G. Strohmeyer and M. Sugihara, Plasma Phys. Control. Fusion, 44, A459 (2002).
22. G. Pacher, H. Pacher, G. Janeschitz, A. Kukushkin and G. Pereverzev, Plasma Phys. Control. Fusion, 46, A257 (2004).
23. M Sugihara, Yu. Igitkhanov, G. Janeschitz, A. Hubbard, Y. Kamada, J. Lingertat, T. H. Osborne and W. Suttrop, Nucl. Fusion, 40, 1743 (2000).
24. T. S. Hahm and P. H. Diamond, Phys. Fluids, 30, 133 (1987).
25. B. N. Rogers, J. F. Drake and A. Zeiler, Phys. Rev. Lett., 81, 4396 (1998).
26. W. Kerner, Contrib. Plasma Phys., 38, 118 (1998).
27. W. M. Stacey, Phys. Plasmas, 6, 2452 (1999).
28. J. D. Callen, Nucl. Fusion, 45, 1120 (2005).
29. J. D. Callen, University of Wisconsin, personal communication (2007).
30. S. Hamaguchi and W. Horton, Phys. Fluids B, 4, 319 (1992).
31. G. Bateman, A. H. Kritz, A. Y. Pankin, T. Onjun, J. E. McElhenny and C. McDonald, Plasma Phys. Control. Fusion, 48, A93 (2006).
32. B. Kadomtsev and O. Pogutse, Nucl. Fusion, 11, 67 (1971).
33. D. R. McCarthy, P. N. Gudzar, J. F. Drake, T. M. Antonsen and A. B. Hassam, Phys. Fluids B, 4, 1846 (1992).
34. P. N. Gudzar, J. F. Drake, D. R. McCarthy, A. B. Hassam and C. S. Liu, Phys. Fluids B, 5, 3712 (1993).
35. G. Bateman, A. H. Kritz, J. E. Kinsey,A. J. Redd and J. Weiland, Phys. Plasmas, 5, 1793 (1998).
36. P. Gudzar, R. G. Kleva, A. Das and P. K. Kaw, Phys. Rev. Lett., 87, 3230 (1997).
37. T.E. Evans, R.A. Moyer and P. Monat, Phys. Plasmas 9, 4957 (2002).
38. L. W. Yan and T. E. Evans, "Stochastic magnetic boundary modeling with large ELM suppression in a high confinement plasma in DIII-D", to appear in J. Nucl. Mater. (2006).
39. W. M. Stacey, E. W. Thomas and T. M. Evans, Phys. Plasmas, 2, 3740 (1995); and 4, 678 (1997).
40. R. Hulse, Nucl. Technol. Fusion, 3, 259 (1983).
41. W. M. Stacey, Phys. Plasmas, 5, 1015 (1998); 8, 3673 (2001); Nucl. Fusion, 40, 678 (2000).

III. IMPLEMENTATION OF THE GTNEUT 2D NEUTRALS TRANSPORT CODE FOR ROUTINE DIII-D ANALYSIS

(Z. W. Friis and W. M. Stacey, *Georgia Tech*; T. D. Rognlien, *Lawrence Livermore National Laboratory;* R. J. Groebner, *General Atomics*)

Abstract

The Georgia Tech Neutral Transport (GTNEUT) code[1,2] is being implemented to provide a tool for routine analysis of the effects of neutral atoms on edge phenomena in DIII-D. GTNEUT can use an arbitrarily complex two-dimensional grid to represent the plasma edge geometry[1]. The grid generation capability built into the UEDGE code[3], which utilizes equilibrium fitting data taken from experiment, is being adapted to produce geometric grids for the complex 2D geometries in the DIII-D plasma edge. The process for using experimental measurements supplemented by plasma edge calculations to provide the required background plasma parameters for the GTNEUT calculation will be systematized once the geometric grid generation is complete.

A. Introduction

In the past, most plasma physicists concentrated their research efforts on the exploration of core plasma, with little attention given to the edge region including the SOL, divertor and pedestal regions. This is now changing because many experiments have indicated that phenomena taking place in the plasma edge are very important for the overall performance characteristics of the confined plasma. Additionally, it has been shown that some of these edge phenomena are greatly influenced by neutral particles. It is for this reason we seek to better understand how neutral particles affect phenomena in the plasma edge.

In order to analyze the affects of neutral atoms on edge phenomena, an accurate but computationally efficient calculation of neutral particle transport in edge plasma is needed. For this purpose, the two-dimensional Georgia Tech Neutral Transport (GTNEUT) code[1] will be used. GTNEUT is a two-dimensional neutral particle transport code based on the Transmission and Escape Probabilities (TEP) method[2], which has been extensively benchmarked against both experiment and Monte Carlo calculations[4-7]. GTNEUT is computationally efficient compared with some of the standard Monte Carlo codes used today.

B. GTNEUT Geometric Input

While the GTNEUT code has many advantages over some of the Monte Carlo based codes, it does have one very big drawback. GTNEUT utilizes a coordinate-free geometry input file called "*toneut*". "Coordinate-free" means that the two dimensional mesh needed to represent a cross section of a Tokamak plasma only requires geometrical data from each cell such as lengths and angles, as well as relative positions of the sides of neighboring cells. The GTNEUT calculation consists of the calculation of the transmission of uncollided fluxes from an incident interface across a region through an exiting interface and the calculation of fluxes of collided particles exiting a region across

a bounding interface as illustrated in the figure below. The interface balances on these various fluxes must be simultaneously solved to determine the fluxes, from which the densities within the region can be computed.

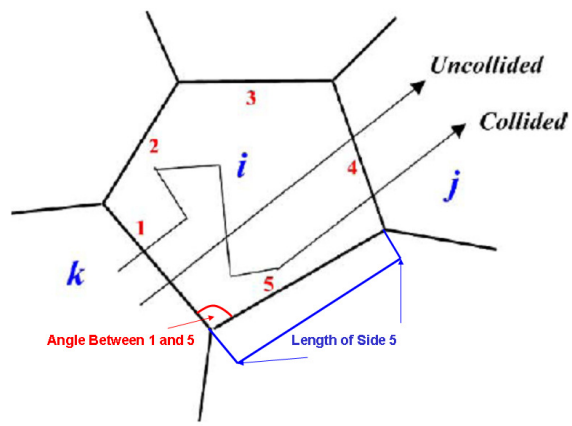

Figure 1: Schematic diagram showing region i and its adjacent regions and the partial currents at the interfaces. [1]

Actual (R,Z) coordinates are not needed and cannot be utilized by GTNEUT itself. Therefore, it can become quite tedious and error prone to manually input such information.

The GTNEUT package does include an automatic grid generator; however, this generator can only create very simple rectangular geometries which are often only used for test cases. For much more complicated geometries, such as a tokamak plasma edge, GTNEUT becomes dependent on the GRID generating capabilities of other codes. In fact, simply obtaining the GTNEUT geometric information for a tokamak plasma becomes a three step process. The first step is obtaining information about the plasma geometry from diagnostics, the second step is generating a mesh from the plasma geometry, and the third step is converting the mesh into a format that GTNEUT can utilize.

C. EFIT

Utilization of the DIII-D EFIT (Equilibrium Fitting) code is the first step in our process. The EFIT code was developed to translate measurements from plasma diagnostics into useful information like plasma geometry by solving the Grad-Shafranov equation. Such measurements are provided from diagnostics such as external magnetic probes, external poloidal flux loops, and the Motional Stark Effect (MSE)[8]. Running the EFIT code is a fairly simple procedure. One simply specifies the experiment number, the initial time slice to be studied, and the number of times to be studied as well as the time interval between each step. Additionally, one must specify which of the different SNAP versions are used.

Table 1:List of different SNAP versions, and their uses[9].

SNAP Version	Use
def	defaulted SNAP file, no edge gradients. For L-mode discharges, break-down error field analysis. Polynomial representation. No edge current.
j	finite edge gradients included in the current representation.
jt	Edge gradients constrained to vanish weakly. For H-mode discharges. Polynomial representation. Edge current is constrained to vanish weakly.
scrape	force-free scrape-off layer and vessel currents included in the fitting.
mses	For L- and H- mode discharges with MSE. Spline representation. Finite edge current allowed.
mse2_j1	MSE plus constrainted edge J.
mses_er	MSE with ER correction for shots later than 91000.

The code takes seconds to run and stores information about the plasma geometry in a number of files called "EQDSK" files. There are several types of EQDSK files, but the ones utilized most often are the AEQDSK and GEQDSK files. The AEQDSK file contains mostly scalar values as well as the global plasma parameters. The GEQDSK file holds most of the information about the flux surfaces and the R and Z positions[10]. Below is the output from a code designed to view the EQDSK files.

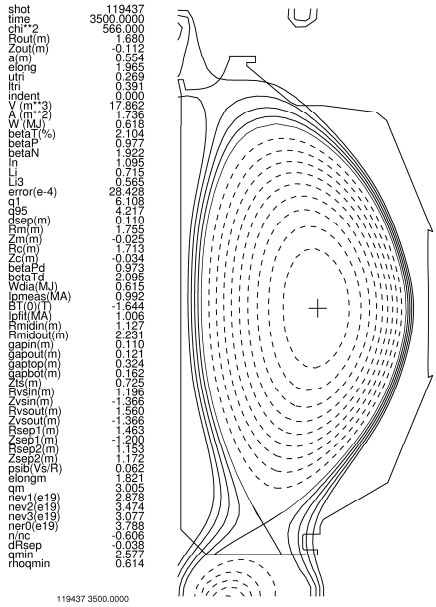

Figure 2: EFIT Data from shot 119437

There are several methods used run the EFIT code and some methods use different locations from where experimental data was obtained. Some methods use the diagnostic data on the MDSplus servers while others uses the data that has been reduced by experimentalist. For example, the diagram below shows two different EFITs for the same shot at the same time. The only difference is how the EFIT was generated. The EFIT equilibrium can be improved by adding extra measurements to the analysis. As the equilibrium is refined by the addition of data, the location of strike points and other divertor geometry may change in small but important ways, from the point of view of edge analysis. It is not clear if there is a "best" strategy for generating equilibria for edge analysis. Ascertaining which EFIT is correct requires collaboration with experimentalist.

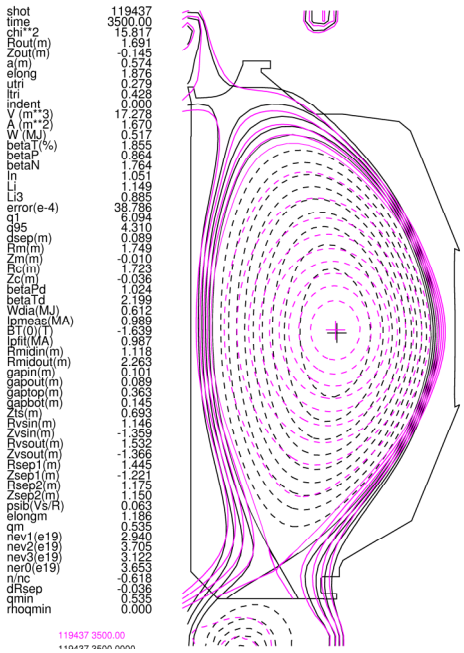

Figure 3 : Overlap of different EFITs for Shot 119437.

D. <u>UEDGE Mesh Generation</u>

Once we have generated the EFIT, the second step in the process is generating the mesh. Manually doing this can take several months. For example, the mesh depicted below was created by hand using a CAD program to calculate the lengths and angles of each cell.

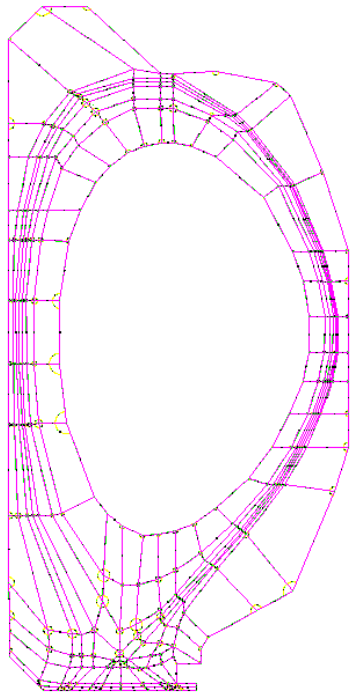

Figure 4: Manually Generated Mesh

While the manual method of grid generation may actually have some advantages such as being able to specify geometries at certain locations in more detail, the process is inherently cumbersome, prone to error, and very tedious. Instead of manually generating the mesh, we have opted to use the UEDGE code's mesh generating capabilities. UEDGE is a very powerful two-dimensional (2D) fluid transport code for collisional edge plasmas. UEDGE can perform a large number of calculations and even be coupled to several Monte Carlo based neutrals codes[3]. However, for now, we are primarily interested in UEDGE's grid generating capabilities.

UEDGE generates meshes using the EQDSK files specified in a previous section. Also, an input file is required to specify how coarse the mesh will be. Of most use to us are the inputs below.

Table 2: Inputs to specify UEDGE grid[3].

Input Name	Purpose
nxleg(1,1)	Number of Poloidal mesh pts from inner plate to x-point
nxcore(1,1)	Number of Poloidal . mesh pts from x-point to top on inside
nxcore(1,2)	Number of Poloidal mesh pts from top to x-point on outside
nxleg(1,2)	Number of Poloidal mesh pts from x-point to outer plate
nysol(1)	Number of Radial mesh pts in SOL
nycore(1)	Number of Radial mesh pts in core

By default, the mesh generator produces orthogonal meshes; however, it can be very useful to generate non-orthogonal meshes. This is especially true if one wants to fit the mesh to the divertor. By altering an input option called "ismmon" and specifying the divertor plate locations in the UEDGE input file, the grid generator will extend the mesh to the divertor producing a nice fit. An example of this can be seen below[3].

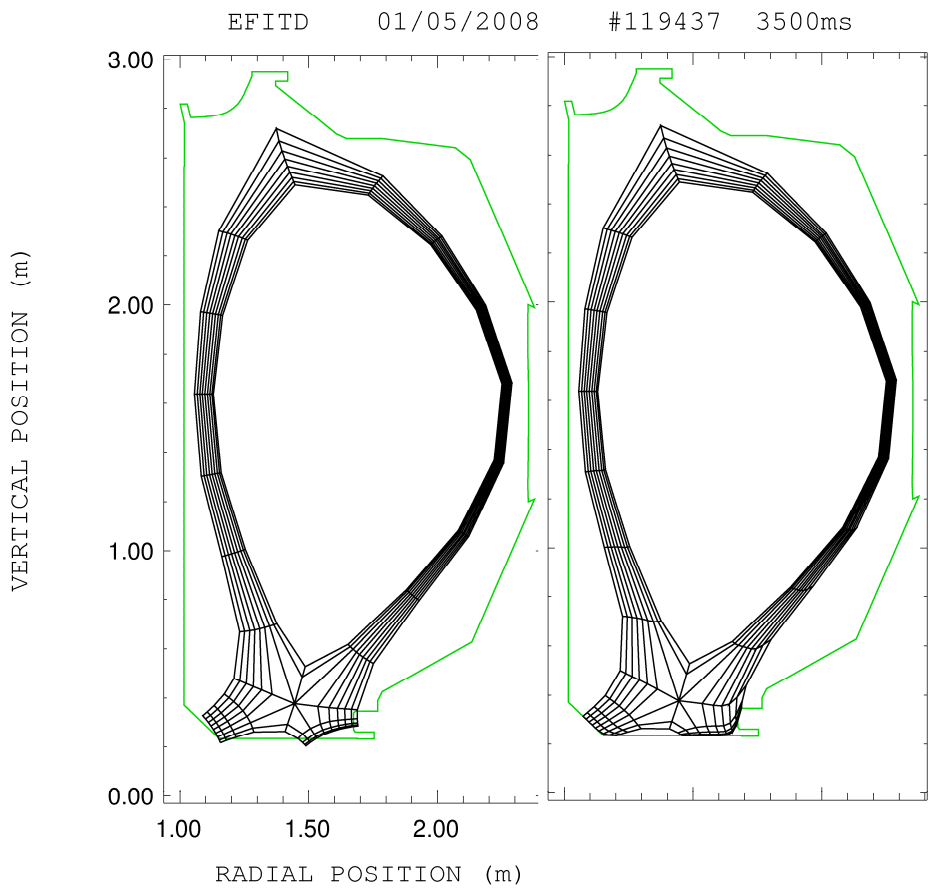

Figure 5: Comparison of Orthogonal and Non-Orthogonal Meshes

Additionally, a full UEDGE run is not required in order to generate the meshes. Typing the following at the UEDGE command prompt will generate a mesh file called *gridue*[3].

call flxrun
call grdrun

The mesh produced by the UEDGE grid generator can be very useful for GTNEUT calculations; however, as seen in the examples above, the grid does not extend to the walls of the confinement vessel. In between the SOL and Wall (which we call the Gap region), it is necessary to extend the UEDGE grid to the wall for the GTNEUT grid.

E. Adaptation of UEDGE Mesh for GTNEUT Input

For simplicity, the most efficient way to do this is simply extending the last layer of cells in the SOL perpendicularly to the wall. Below is an example of what we have done.

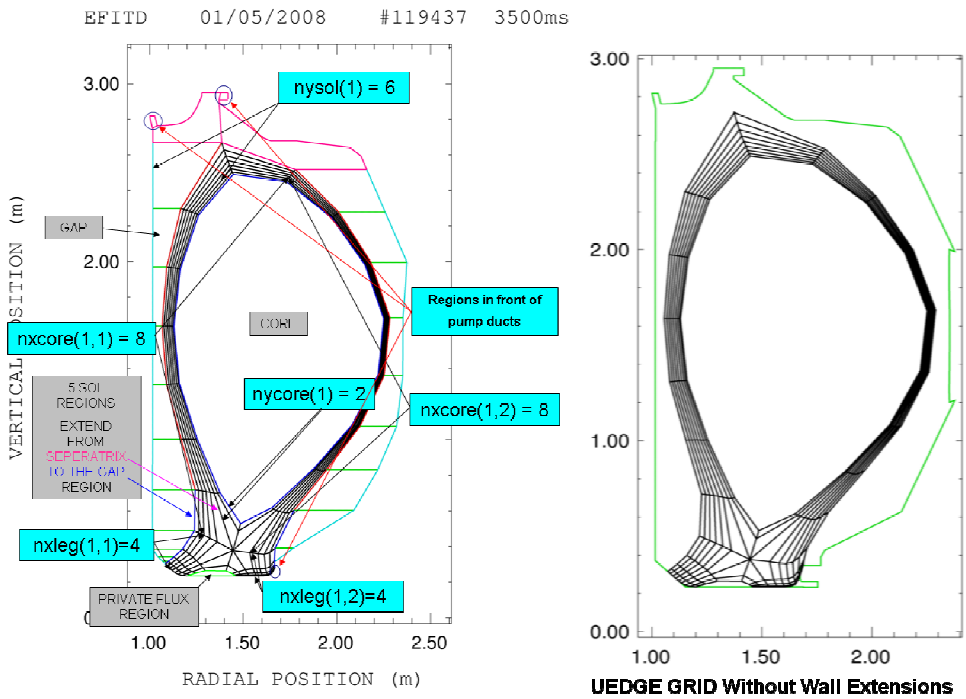

Figure 6: Comparison of UEDGE grid extended to wall.

By, examining what we have done here, we can also see how the UEDGE input file works. Notice there are six SOL regions on the right hand figure (SOL regions are the regions that lie outside of the seperatrix. This was accomplished by setting nysol(1) equal to 6. The left hand figure only has five, plus the Gap region. We have simply redefined the last region of cells. Most of the cells in our grid have four sides. The two main exceptions are the private flux region show in lime green on the left side. It is defined as a function of the UEDGE input file and *gridue* file. Also, the cells shown in magenta at the very top of the vessel may have more than 4 sides. Lastly, the outermost corners of the divertor regions may contain only 3 sides depending on their location with respect to the wall. As of now, this is not a purely automatic grid generating system. One must first plot the grid to make sure errors have not arisen before proceeding.

F. Summary and Conclusions and Present Work

The present version of the UEDGE to GTNEUT grid adaptor is much more efficient and accurate than the manual method. It has been successfully used on discharges 119437 and 119436. It still needs to be tested on other discharges using different EFIT versions. Also, the present version of the adaptor only works for single

lower null discharges. Modifications to work on a single upper null or double null discharge should not be too difficult.

Presently, routines are being added to the adaptor to actually write the GTNEUT input file. This currently exists for the plasma regions between the core and the gap regions. However, proper tracking of the cells is of the utmost importance. We are breaking the grid down into regions as illustrated by various colors in the diagram on the left in Fig. 5 to facilitate this tracking more easily. Additionally, the cells are being numbered in a way that will make assigning temperatures and densities from diagnostics much easier.

References

1. J. Mandrekas, Comp. Physics Commun., 161, 36 (2004).
2. W. M. Stacey and J. Mandrekas, Nucl. Fusion, 34, 1385 (1994).
3. T. D. Rognlien, et al., *User Manual of UEDGE Edge-Plasma Transport Code,* LLNL report (2007)
4. W. M. Stacey, J. Mandrekas and R. Rubilar, Fusion Sci. Technol., 40, 66 (2001).
5. R. Rubiliar, W. M. Stacey, J. Mandrekas, Nucl. Fusion, 41, 1003 (2001).
6. J. Mandrekas, R. J. Colchin, W. M. Stacey, et al., Nucl. Fusion, 43, 314 (2003).
7. D-K. Zhang, J. Mandrekas and W. M. Stacey, Phys. Plasmas, 13, 062509 (2006).
8. http://fusion.gat.com/theory/Efitdef
9. http://fusion.gat.com/theory/Efitsnap
10. http://fusion.gat.com/theory/Efitoutputs

IV. <u>EDGE PEDESTAL STRUCTURE AND TRANSPORT INTERPRETATION</u> (In the absence of or in between ELMs)

W. M. Stacey (Georgia Tech) and R. J. Groebner (General Atomics)

Abstract

- A constraint on the ion pressure gradient is imposed by momentum balance. The constraint involves $V_\theta, V_\phi, E_r, V_r$, etc. and momentum transfer rates, all of which can be obtained from experiment.

- Integration of $\frac{1}{n}\frac{\partial n_i}{\partial r} = \left(\frac{1}{p_i}\frac{\partial p_i}{\partial r}\right)_{mom} - \left(\frac{1}{T_i}\frac{\partial T_i}{\partial r}\right)_{\exp}$ using the experimental $V_\theta, V_\phi, E_r, V_r$, etc., yields density profiles that agree well with the directly measured density profiles.

- This pressure gradient constraint can be rearranged to obtain a "pinch-diffusion" expression for the ion flux, which can be used in the continuity equation to obtain a generalized diffusion theory that conserves momentum.

- A methodology for inferring $\chi_{i,e}^{\exp}$ from measured T and n profiles has been developed and applied to DIII-D, with comparison with theory.

- A methodology for inferring radial transfer rates for toroidal angular momentum from measured V_ϕ profiles has been developed and applied to DIII-D, with comparison with theory.

- A methodology for calculating V_θ has been developed and compared with experimental data from DIII-D.

A. Momentum Balance Constraint on Ion Pressure Gradient

Combining the radial and toroidal components of the momentum balance leads to

$$L_{pi}^{-1} \equiv -\frac{1}{p_i^0}\frac{dp_i^0}{dr} = \frac{V_{ri} - V_{pinch,i}}{D_i}, \quad \text{where} \quad D_i \equiv \frac{m_i T_i \nu_{iI}}{\left(e_i B_\theta\right)^2}\left[\left(1+\frac{\nu_{di}^*}{\nu_{iI}}\right) - \frac{1}{Z_I}\right] \tag{1}$$

and

$$V_{pinch,i} = \frac{\left[-M_{\phi i} - n_i e_i E_\phi^A + n_i m_i \left(\nu_{iI} + \nu_{di}^*\right)\left(f_p^{-1} V_{\theta i} + E_r / B_\theta\right) - n_i m_i \nu_{iI} V_{\phi I}\right]}{n_i e_i B_\theta} \tag{2}$$

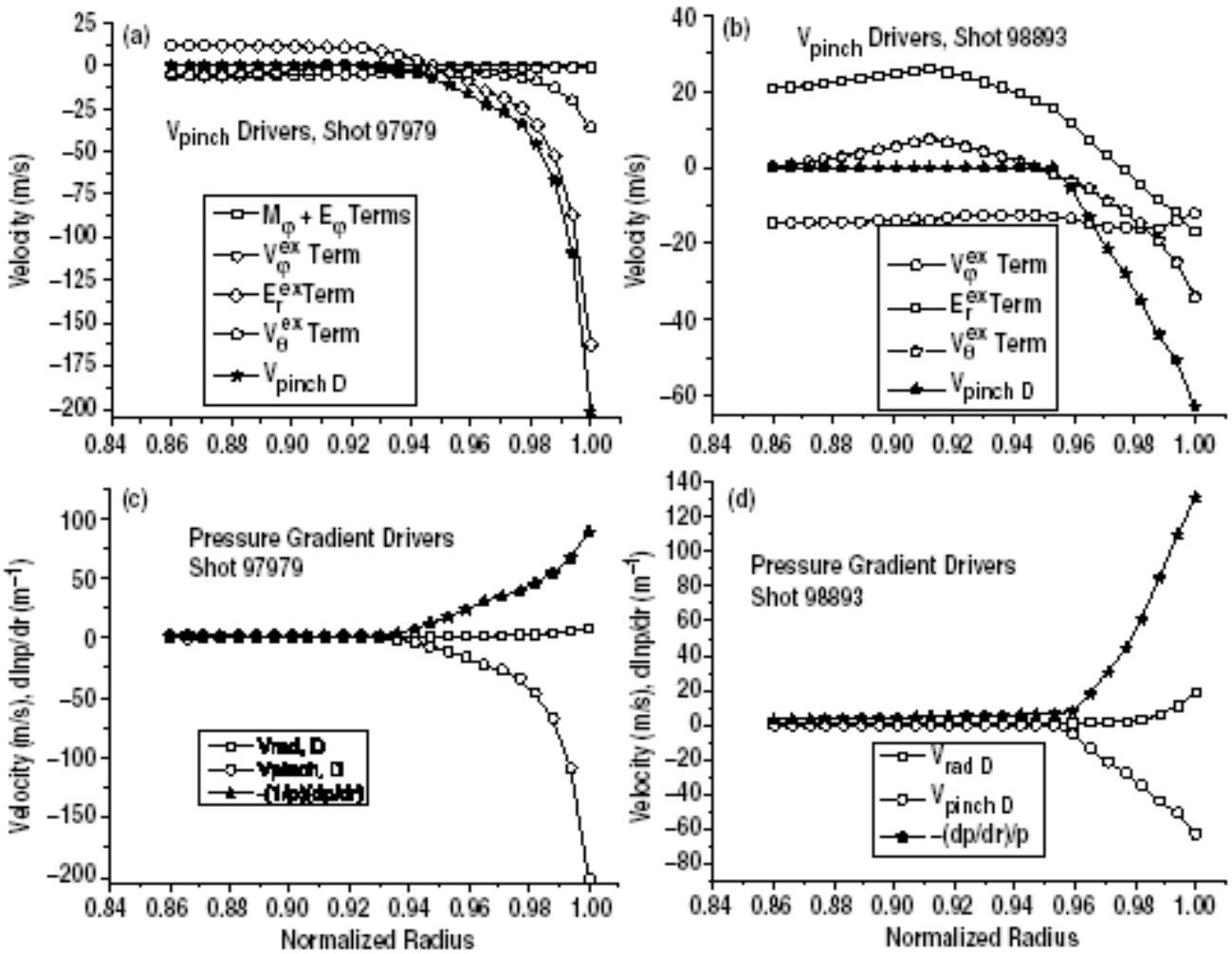

Figure 1 Contribution of the various terms on RHS of Eq. 2 to the pinch velocity (1a and 1b), and contribution of the pinch velocities and radial particle velocity peaking due to ionization of recycling neutrals for two DIII-D H-mode discharges. (PoP, 13, 012513, 2006)

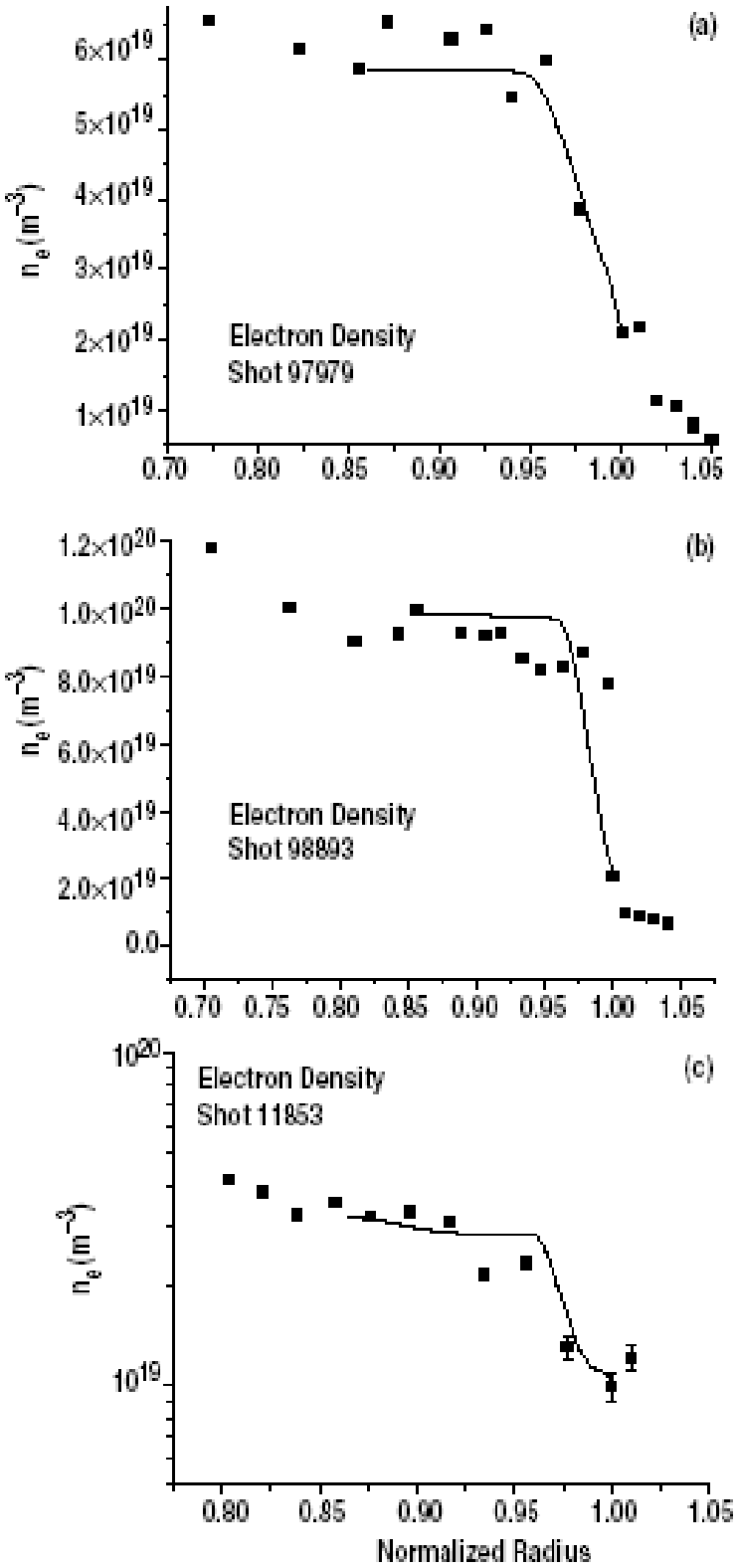

Figure 2 Integration of $-dn_i \Big/ n_i dr = \left[\left(\upsilon_{ri} - \upsilon_{pinch,i}\right) \Big/ D_i\right] - dT_i / T_i dr$ (solid line) compared with directly measured (Thomson scattering) electron densities in three DIII-D H-mode shots.

B. GENERALIZED DIFFUSION THEORY

Rewriting the pressure gradient constraint as a pinch-diffusion relation for the particle flux and substituting into the continuity equation results in a generalized diffusion equation based on momentum and particle balance.

$$-\frac{\partial}{\partial r}\left(D_{jj}\frac{\partial n_j}{\partial r}\right)-\frac{\partial}{\partial r}\left(D_{jk}\frac{\partial n_k}{\partial r}\right)-\frac{\partial}{\partial r}\left(D_{jj}\frac{n_j}{T_j}\frac{\partial T_j}{\partial r}\right)-\frac{\partial}{\partial r}\left(D_{jk}\frac{n_j}{T_k}\frac{\partial T_k}{\partial r}\right)+\frac{\partial\left(n_j\upsilon_{pinch,j}\right)}{\partial r}=S_j \tag{3}$$

where

$$D_{jj}\equiv\frac{m_jT_j\left(\nu_{dj}+\nu_{jk}\right)}{\left(e_jB_\theta\right)^2}\quad,\quad D_{jk}\equiv\frac{m_jT_k\nu_{jk}}{e_je_k(B_\theta)^2} \tag{4}$$

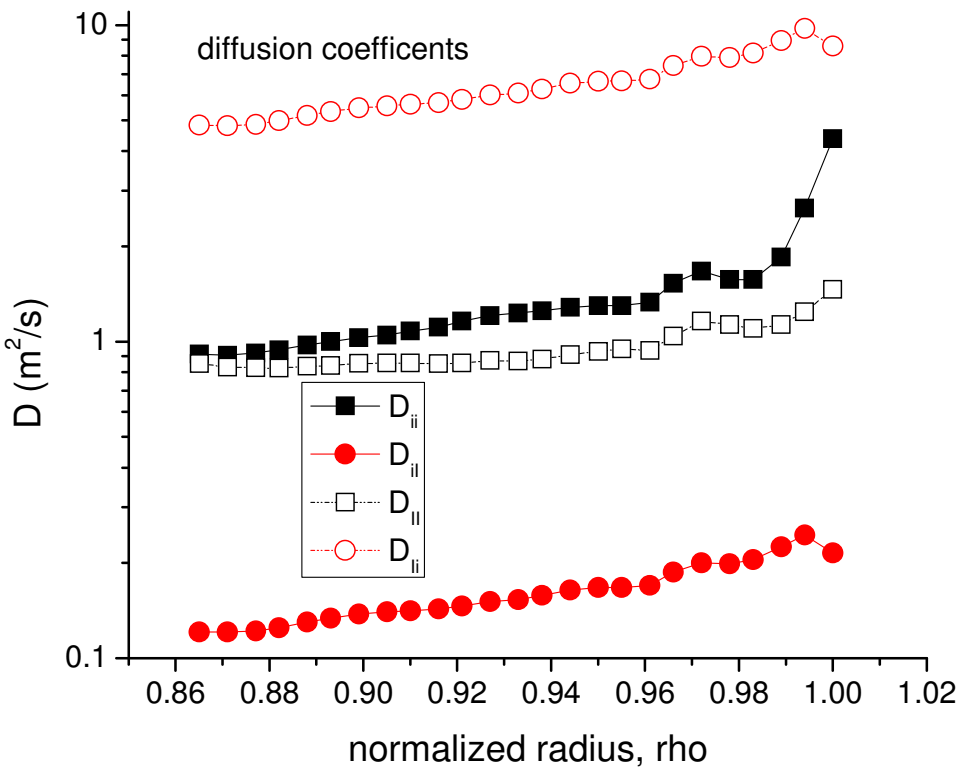

Figure 3 Generalized diffusion coefficients in the edge of DIII-D H-mode shot 92976 (CPP, 48, 94, 2008)

C. INFERRENCE OF EXPERIMENTAL HEAT DIFFUSIVITY

(PoP, 13, 072510, 2006)

FROM DEFINITION OF HEAT CONDUCTION

$$\chi_{i,e}^{\exp}(r) = L_{Ti,e}(r)\frac{q_{i,e}(r)}{n_{i,e}(r)T_{i,e}(r)} \equiv L_{Ti,e}(r)\left[\frac{Q_{i,e}(r)}{n_{i,e}(r)T_{i,e}(r)} - \frac{5}{2}\frac{\Gamma_{i,e}(r)}{n_{i,e}(r)}\right]$$

where $L_{Ti,e}^{-1} \equiv -\left(\partial T_{i,e}/\partial r\right)/T_{i,e}$,

SOLVE FOR HEAT AND PARTICLE FLUXES, USING EXP n & T DATA

$$\frac{\partial Q_i}{\partial r} = -\frac{\partial}{\partial t}\left(\frac{3}{2}n_i T_i\right) + q_{nbi} - \frac{3}{2}\left(T_i - T_o^c\right)n_i n_o^c \langle\sigma\upsilon\rangle_{cx+el} - q_{ie}\ ,\ \ Q_i\left(r_{sep}\right) = Q_{sepi}^{\exp}$$

$$\frac{\partial Q_e}{\partial r} = -\frac{\partial}{\partial t}\left(\frac{3}{2}n_e T_e\right) + q_{nbe} + q_{ie} - n_e n_o \langle\sigma\upsilon\rangle_{ion} E_{ion} - n_e n_z L_z\ ,\ \ Q_e\left(r_{sep}\right) = Q_{sepe}^{\exp}$$

$$\frac{\partial \Gamma_i}{\partial r} = -\frac{\partial n_i}{\partial t} + n_e n_o \langle\sigma\upsilon\rangle_{ion} + S_{nb}\ ,\ \ \Gamma_i\left(r_{sep}\right) = \Gamma_{sepi}^{\exp}$$

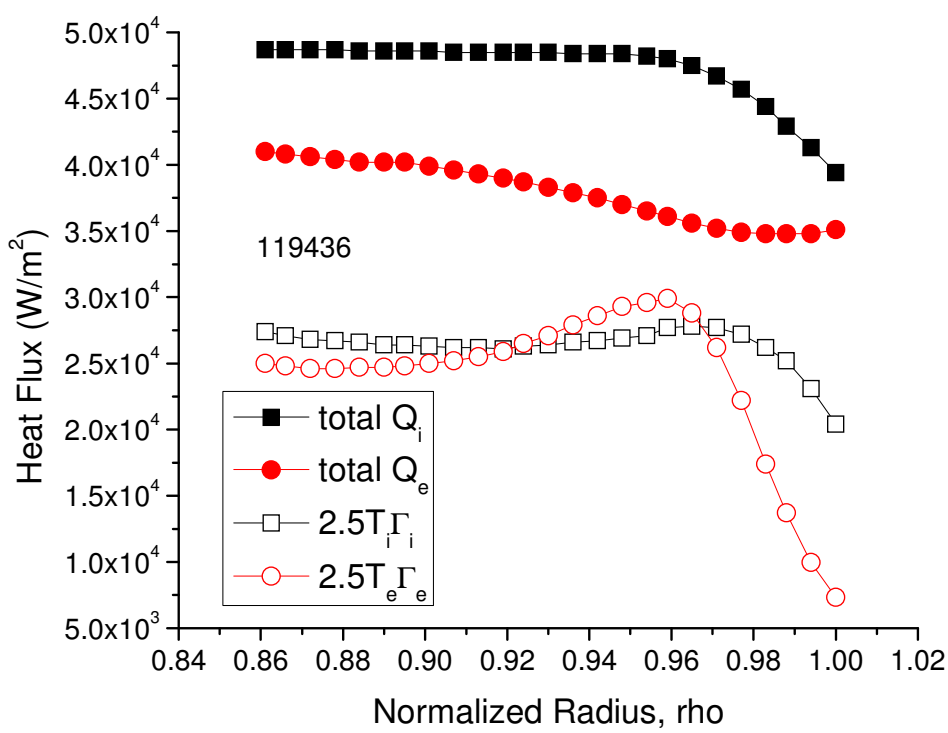

INFERRENCE OF EXPERIMENTAL HEAT DIFFUSIVITY

(PoP, 13, 072510, 2006)

FROM DEFINITION OF HEAT CONDUCTION

$$\chi_{i,e}^{\exp}(r) = L_{Ti,e}(r)\frac{q_{i,e}(r)}{n_{i,e}(r)T_{i,e}(r)} \equiv L_{Ti,e}(r)\left[\frac{Q_{i,e}(r)}{n_{i,e}(r)T_{i,e}(r)} - \frac{5}{2}\frac{\Gamma_{i,e}(r)}{n_{i,e}(r)}\right]$$

where $L_{Ti,e}^{-1} \equiv -\left(\partial T_{i,e}/\partial r\right)/T_{i,e}$,

SOLVE FOR HEAT AND PARTICLE FLUXES, USING EXP n & T DATA

$$\frac{\partial Q_i}{\partial r} = -\frac{\partial}{\partial t}\left(\frac{3}{2}n_i T_i\right) + q_{nbi} - \frac{3}{2}\left(T_i - T_o^c\right)n_i n_o^c \langle \sigma \upsilon \rangle_{cx+el} - q_{ie}\,,\ Q_i\left(r_{sep}\right) = Q_{sepi}^{\exp}$$

$$\frac{\partial Q_e}{\partial r} = -\frac{\partial}{\partial t}\left(\frac{3}{2}n_e T_e\right) + q_{nbe} + q_{ie} - n_e n_o \langle \sigma \upsilon \rangle_{ion} E_{ion} - n_e n_z L_z\,,\ Q_e\left(r_{sep}\right) = Q_{sepe}^{\exp}$$

$$\frac{\partial \Gamma_i}{\partial r} = -\frac{\partial n_i}{\partial t} + n_e n_o \langle \sigma \upsilon \rangle_{ion} + S_{nb}\,,\quad \Gamma_i\left(r_{sep}\right) = \Gamma_{sepi}^{\exp}$$

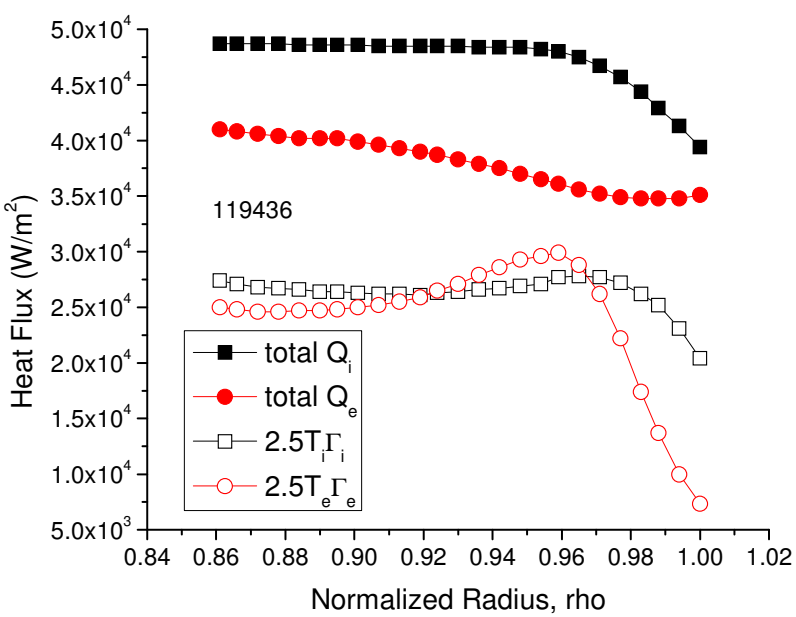

Figure 6a Heat fluxes in DIII-D ELMing H-mode shot 119436

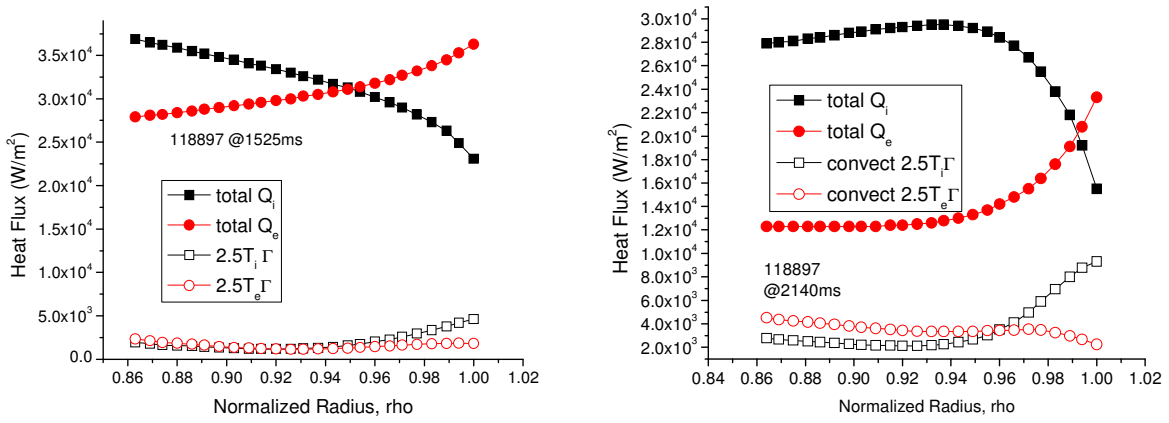

Figure 4 Heat fluxes in L-mode phase @ 1525ms (4a) in the ELM-free H-mode @ 2140ms (4b) of DIII-D shot 118897.

.

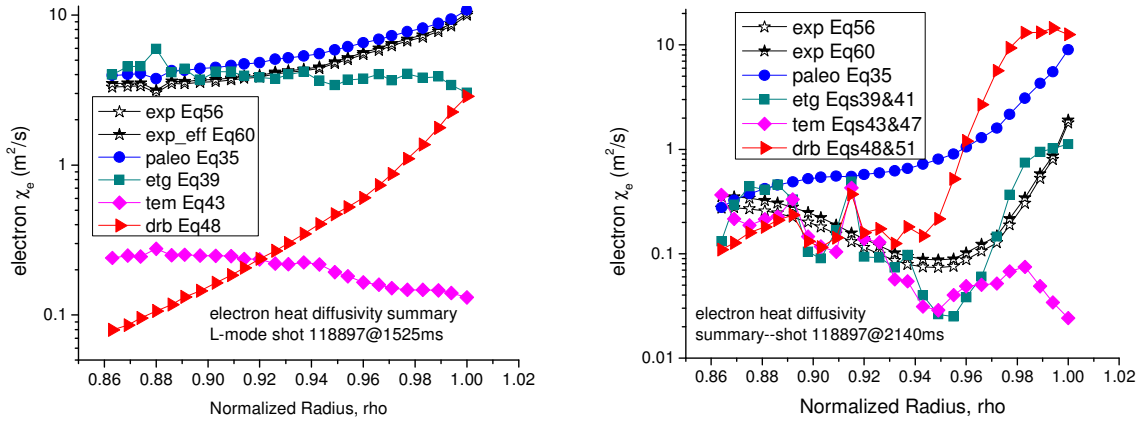

Figure 5 Comparison of theory and experiment for electron heat diffusivity in L-mode (4a) and ELM-free H-mode (4b) phases of DIII-D shot 118897.(Eq. numbers refer to PoP, 15, July 2008).

D. <u>Inferrence of Experimental Toroidal Angular Momentum Transfer Frequencies from Meassured Toroidal Rotation Velocities</u> (PoP, 15, 012503, 2008)

If both the deuterium and carbon rotation velocities could be measured, then their respective toroidal momentum balance equations could be solved "backwards" for their momentum transfer frequencies

$$\nu_{dj} = \nu_{jk}\left[\frac{n_j e_j E_\phi^A + e_j B_\theta \Gamma_{rj} + M_{\phi j}}{n_j m_j \nu_{jk} V_{\phi j}} - \left(1 - \frac{V_{\phi k}}{V_{\phi j}}\right)\right]$$

but since they are not, a perturbation approach is needed.

1) add the tor. mom. equations for the 2 species and define (j= deut, k= carbon)

$$\nu_d^{eff} \equiv \frac{n_j n_j \nu_{dj} + n_k m_k \nu_{dk}}{n_j m_j + n_k m_k} =$$

$$\frac{\left(n_j e_j E_\phi^A + e_j B_\theta \Gamma_{rj} + M_{\phi j}\right) + \left(n_k e_k E_\phi^A + e_k B_\theta \Gamma_{rk} + M_{\phi k}\right) - \{n_j m_j \nu_{dj}\left(V_{\phi j} - V_{\phi k}\right)\}}{(n_j m_j + n_k m_k) V_{\phi k}}$$

2) obtain a zero order estimate ν_{d0} by setting $\left(V_{\phi j} - V_{\phi k}\right) = 0$

3) use ν_{d0} in deuterium tor. mom. equation to solve for

$$\left(V_{\phi j} - V_{\phi k}\right)_0 = \frac{\left(n_j e_j E_\phi^A + e_j B_\theta \Gamma_{rj} + M_{\phi j}\right) - n_j m_j \nu_d^0 V_{\phi k}^{\exp}}{n_j m_j \left(\nu_{jk} + \nu_d^0\right)}$$

4) which can be used in carbon tor. mom. equation to solve for

$$\nu_{dk} = \frac{\left(n_k e_k E_\phi^A + e_k B_\theta \Gamma_{rk} + M_{\phi k}\right) + n_k m_k \nu_{kj}\left(V_{\phi j} - V_{\phi k}\right)_0}{n_k m_k V_{\phi k}^{\exp}}$$

5) which can be used in defininition of $\nu_{deff} \approx \nu_{d0}$ to obtain $\nu_{dj} \approx \nu_{d0}$

Inferred Toroidal Momentum Transfer Frequencies

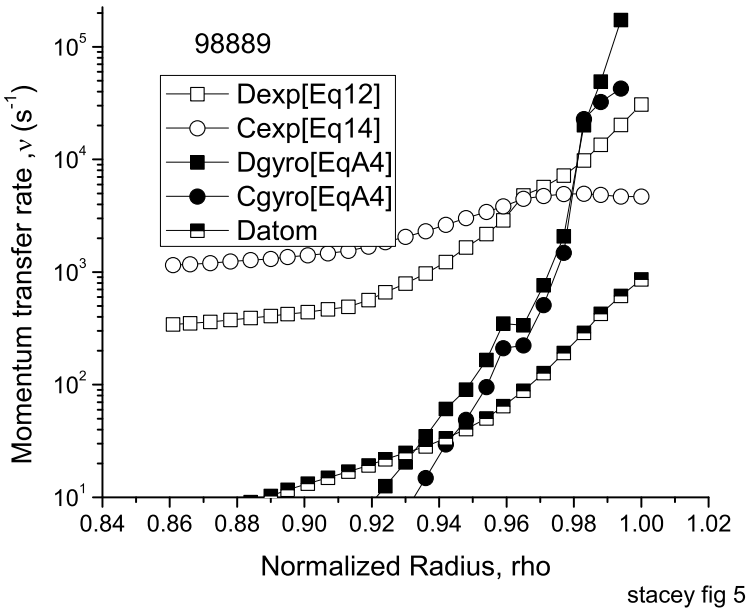

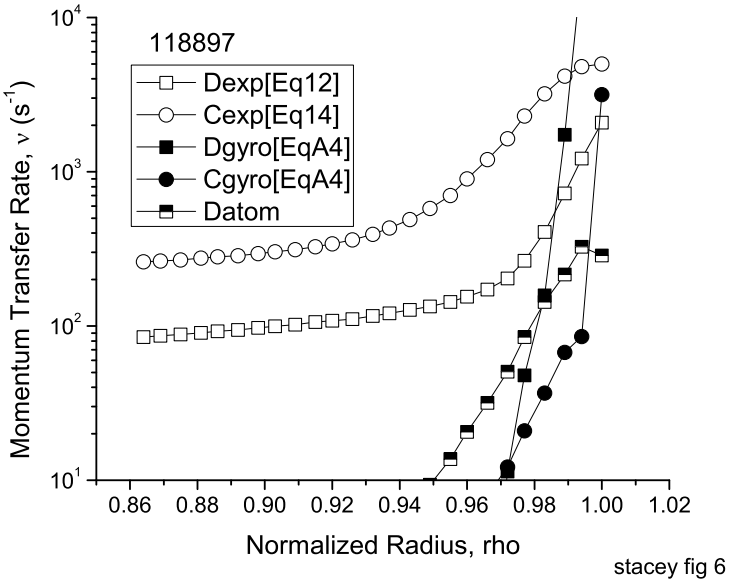

Figure 6 Experimentally inferred toroidal angular momentum transfer frequency averaged over ELMs in H-mode shots 98889 (6a) and in ELM-free H-mode shot 118897 in DIII-D compared with transfer frequencies calculated for neoclassical gyroviscosity and atomic physics effect of recycling neutrals. (Eq. numbers refer to PoP, 15, 012503,2008).

E. POLOIDAL ROTATION

POLOIDAL ROTATION VELOCITIES ARE CALCULATED FROM THE POLOIDAL MOMENTUM BALANCE EQATIONS (PoP, 15, 012501, 2008)

$$n_j m_j \left[\left(V_{\mathrm{j}} \cdot \nabla \right) V_{\mathrm{j}} \right]_\theta + \left[\nabla \cdot \Pi_{\mathrm{j}} \right]_\theta + \frac{1}{r} \frac{\partial p_j}{\partial \theta} - M_{\theta j} + n_j m_j \nu_{jk} \left(V_{\theta j} - V_{\theta k} \right) +$$
$$n_j e_j \left(V_{rj} B_\phi - E_\theta \right) + n_j m_j \nu_{ionj} V_{\theta j} = 0$$

Using a neoclassical parallel viscosity model

$$\left\langle \mathbf{B} \cdot \nabla \cdot \Pi_{\mathrm{P}}^{\mathrm{j}} \right\rangle_{NEO} = \frac{3}{2} \left\langle \eta_{0j} A_{0j}^{\theta} \frac{\partial B_\theta}{\partial \mathrm{l}_\theta} \right\rangle \left[\overline{V}_{\theta j} + \frac{B_\phi K^j T_j L_{Tj}^{-1}}{e_j B^2} \right] + \frac{3}{2} \left\langle \eta_{0j} A_{0j}^{\phi} \frac{\partial B_\theta}{\partial \mathrm{l}_\theta} \right\rangle \overline{V}_{\phi j}$$ **where the stress tensor is**

$$A_{0j}^{\theta} = 2 \left\{ -\frac{1}{3} \left(\frac{\partial V_{\theta j}}{\partial l_\theta} \right) + \left[\left(\frac{1}{R} \right) \frac{\partial R}{\partial l_\theta} + \frac{1}{3} \left(\frac{1}{B_\theta} \right) \frac{\partial B_\theta}{\partial l_\theta} \right] V_{\theta j} \right\} / \overline{V}_{\theta j}$$

$$A_{0j}^{\phi} = 2 f_p R \frac{\partial \left(V_{\phi j} / R \right)}{\partial l_\theta} / \overline{V}_{\phi j}$$

$$\eta_{0j} = n_j m_j \upsilon_{thj} q R f_j \left(\nu_{jj}^* \right) \quad \textbf{with} \quad f_j = \frac{\varepsilon^{-3/2} \nu_{jj}^*}{\left(1 + \varepsilon^{-3/2} \nu_{jj}^* \right) \left(1 + \nu_{jj}^* \right)}$$

leads to a coupled set of eqs for the deuterium and carbon velocities

$$\Psi_{\theta j} \left[-q \Psi_{\phi j} \varepsilon \left(\hbar_j^s + \Phi^s \right) + q^2 f_j f_p \left(1 + \Phi^c + \frac{2}{3} \hbar_j^c \right) + f_p \nu_{jk}^* + f_p \nu_{atj}^* \right]$$
$$- \Psi_{\theta k} \nu_{jk}^* \sqrt{\frac{m_j}{m_k}} f_p = - \Psi_{rj} - q \varepsilon \frac{1}{4} \hbar_j^s - q \varepsilon \Phi_j \left[\frac{1}{4} \left(\Phi^s \right) \right] -$$
$$q^2 f_j f_p \left(\Psi_{\phi j} + P_j' \right) \Phi^c - q \varepsilon \Psi_{\phi j} \left[\left(\Psi_{\phi j} + P_j' \right) \Phi^s + \frac{1}{2} \Psi_{\phi j} \hbar_j^s \right]$$

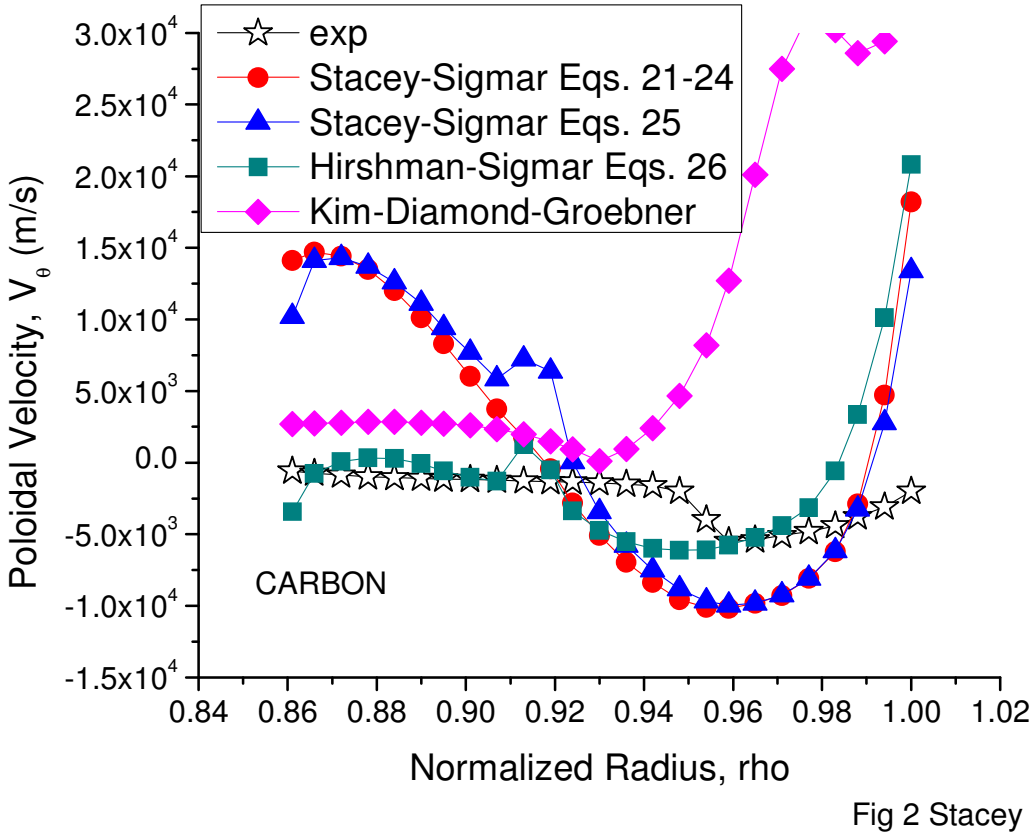

Figure 7 Comparison of calculated and measured carbon velocities in DIII-D shot H-mode 119436. (Eq. numbers refer to PoP, 15, 012501,2008.)

F. CONCLUSIONS

- Momentum balance consistently relates the measured ion pressure gradient with the measured V_ϕ, V_θ, E_r, etc. and the calculated V_r, implying that if we could calculate the $V_\phi, V_\theta, E_r, V_r$ and knew the thermal transport coefficients we would be able to predict the density and temperature profiles in the edge pedestal.

- A generalized diffusion theory which preserves this consistency between pressure gradients and $V_\phi, V_\theta, E_r, V_r$ etc. has been developed and should be used for calculating ion particle profiles in the edge pedestal.

- The simple analytical expressions for thermal diffusivities that are widely used in transport codes do <u>not</u> reliably predict $\chi_{i,e}$ that agree with experimentally inferred values in the edge pedestal, although some of the itg and etg comparisons are promising.

- The radial transfer rate of toroidal angular momentum is much larger than transfer rates calculated from neoclassical gyroviscous theory and from atomic physics, except just inside the separatrix, implying the need to identify other momentum transfer mechanisms in the edge pedestal.

- An extended neoclassical theory predicts V_θ profiles reasonably near to measured profiles, and there is a possibility that a better calculation of the poloidal and radial electric field in the edge pedestal could resolve the present disagreement.

V. HEP BENCHMARKING ACTIVITY

(W. M. Stacey, *Georgia Tech)*

Abstract

A group of people are collaborating in the comparison experimental thermal diffusivities inferred from experimental data measured in the edge pedestal of DIII-D H-mode discharges using different codes. I am providing calculations based on a 1D edge transport code (as described in section II and Ref. 1), Rich Groebner (*General Atomics)* is providing calculations based on the 1.5D transport/MHD code ONE-TWO[2], Tarig Rafiq (*Lehigh*) is providing calculations based on the Multimode transport model in the 1.5D transport/MHD code ASTRA[3], Tom Rognlien (*Lawrence Livermore National Laboratory*) is providing calculations based on the 2D transport code UEDGE[4], and Larry Owen and John Canick (*Oak Ridge National Laboratory*) are providing calculations based on the 2D transport code SOLPS[5]. Jim Callen (*Wisconsin*) is coordinating the activity.

A. <u>1D Transport Calculations</u>

My calculations for the two shots initially being considered by the group are shown in Figs 1 and 2. The edge pedestal plasma density in shot 98889 is about 1/2 of the edge density in shot 118897, as a consequence of which the neutral penetration is much greater for 98889, resulting in charge exchange being the dominant heating/cooling mechanism in the very edge for 98889 and resulting in very different heat flux profiles for the two shots. The inferred experimental chi profiles in the edge are also quite different for the two cases. The calculation procedure is described fairly succinctly in Ref. 1.

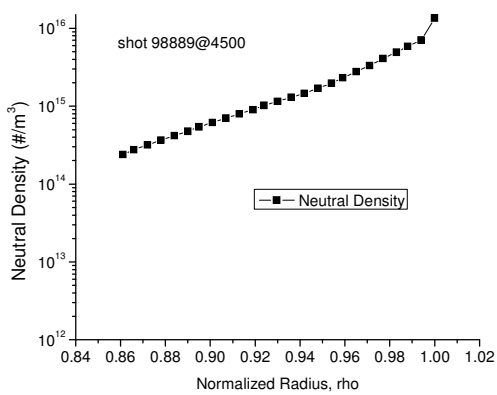

Fig. 1a Neutral Density
Shot 98889@4500

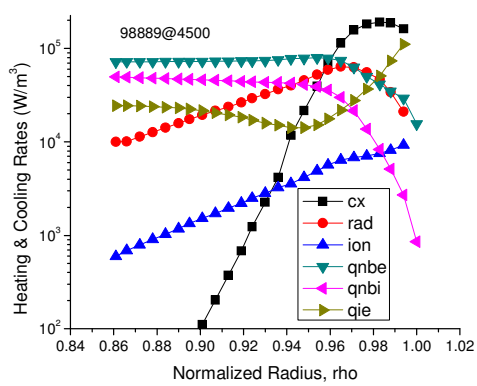

Fig. 1b Heating & Cooling Rates
Shot 98889@4500

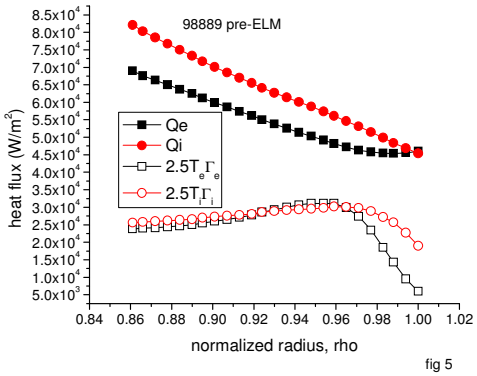

Fig. 1c Total & Convective Heat Fluxes Shot 98889@4500

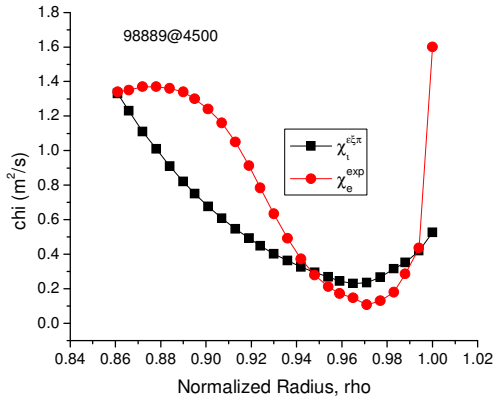

Fig. 1d χ_e & χ_i Experimental Shot 98889@4500

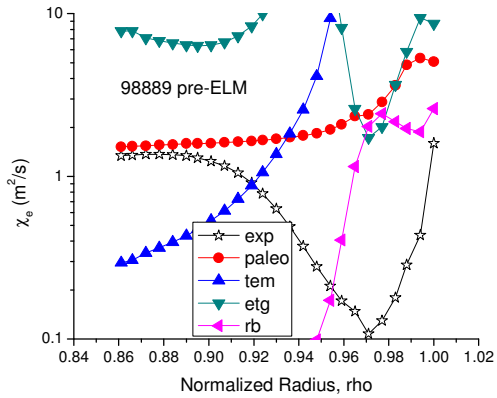

Fig. 1e Electron χ Shot 98889@4500

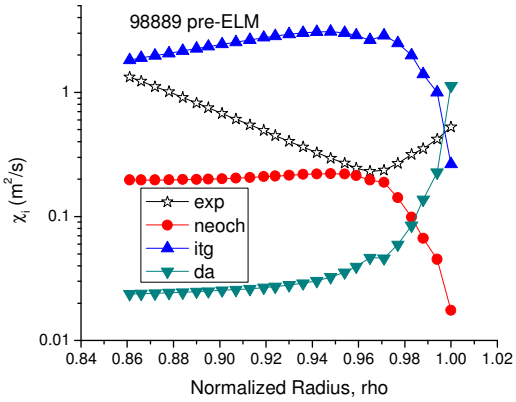

Fig.1f Ion χ Shot 98889@4500

.

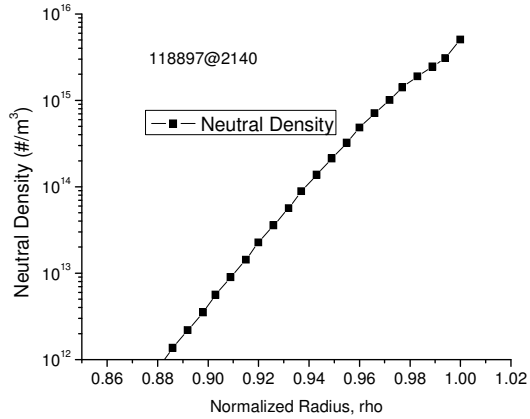

Fig. 2a Neutral Density Shot 118897@2140.

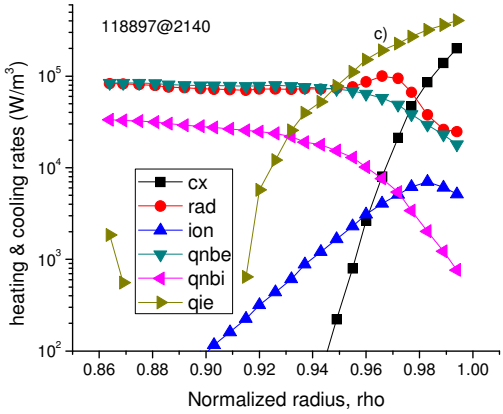

Fig. 2b Heating & Cooling Rates Shot 118897@2140.

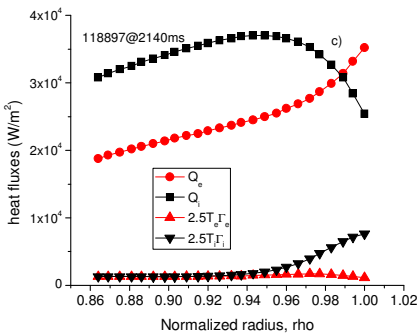

Fig. 2c Total & Convective Heat Fluxes Shot 118897@2140.

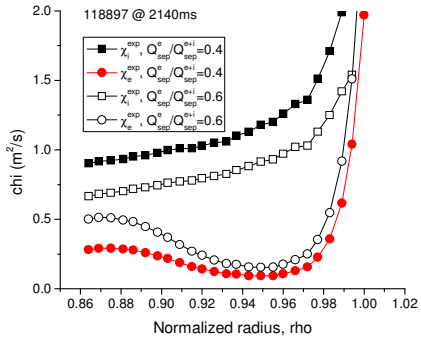

Fig. 2d. χ_e & χ_i Experimental Shot 118897@2140.

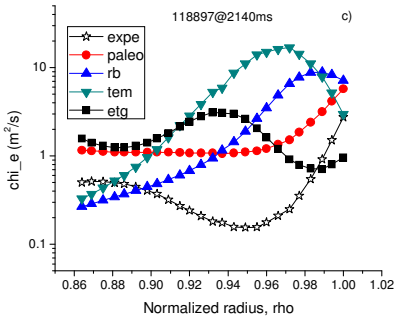

Fig. 2e Electron χ Shot 118897@2140.

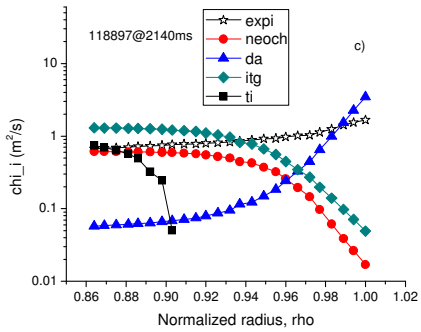

Fig. 2f Ion χ Shot 118897@2140.

B. Applications of the Miller Equilibrium to the Poloidal Variation of Temperature Gradients and Conductive Heat Fluxes

Stimulated by the relatively good agreement between the approximate formulas for the poloidal variation of the conductive heat flux that Callen derived[6] from the Miller equilibrium[7] with the calculations by the 2D codes, this formalism has been developed further, essentially retaining the dependence on triangularity and retaining an arbitrary poloidal location for measured temperature gradient in the Miller equilibrium. The result is an expression for the quantity $G(r,\theta) \equiv q(r,\theta)/\langle q(r)\rangle \equiv \langle L_T(r)\rangle / L_T(r,\theta)$ which relates the local and flux surface averaged conductive heat fluxes or temperature gradient scale lengths.

Miller equilibrium

Miller, et al.[7] derived analytical expressions for an equilibrium flux surface in a plasma as shown in Figure 3 with elongation κ, triangularity δ, and displaced centers $R_0(r)$, where r is

the half-diameter of the plasma along the midplane with center located at distance $R_0(r)$ from the toroidal centerline.

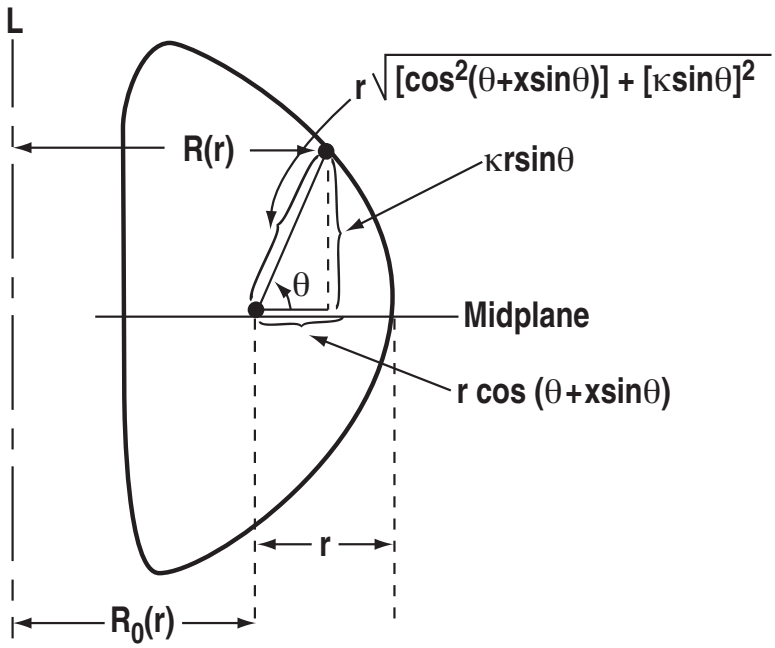

Figure 3 Miller equilibrium parameters

The R and Z coordinates of this plasma are described by[7]

$$R(r) = R_0(r) + r\cos\left[\theta + x\sin\theta\right]$$
$$Z(r) = \kappa r \sin\theta \tag{1}$$

where $x \equiv \sin^{-1}\delta$.

The poloidal magnetic field in such flux surface geometry is[7]

$$RB_p = \left|\nabla\phi\times\nabla\psi\right| = \frac{\partial\psi}{\partial r}\left|\nabla r\right|$$
$$= \frac{\frac{\partial\psi}{\partial r}\kappa^{-1}\left[\sin^2(\theta + x\sin\theta)(1 + x\cos\theta)^2 + \kappa^2\cos^2\theta\right]^{1/2}}{\cos(x\sin\theta) + \frac{\partial R_0}{\partial r}\cos\theta + \left[s_\kappa - s_\delta\cos\theta + (1+s_\kappa)x\cos\theta\right]\sin\theta\sin(\theta + x\sin\theta)} \tag{2}$$

where $s_\kappa = \frac{r}{\kappa}\frac{\partial\kappa}{\partial r}$ and $s_\delta = r\frac{\partial\delta}{\partial r}/\sqrt{(1-\delta^2)}$ account for the change in elongation and triangularity, respectively, with radial location.

The shifted circle model (which leads to the Shafranov shift) yields

$$\frac{\partial R_0}{\partial r} \equiv \Delta' = -\frac{r}{R_0}\left(\beta_p + \frac{1}{2}l_i\right) \tag{3a}$$

and a shifted ellipse model by Lao, et al.[8] yields

$$\frac{\partial R_0}{\partial r} = -\frac{r}{R_0}\left[\frac{2\left(\kappa^2+1\right)}{\left(3\kappa^2+1\right)}\left(\beta_p + \frac{1}{2}l_i\right) + \frac{1}{2}\frac{\left(\kappa^2-1\right)}{\left(3\kappa^2+1\right)}\right] \tag{3b}$$

Flux surface average

The flux surface average (FSA) of a quantity $A(r,\theta)$ in this flux surface geometry is

$$\left\langle A(r,\theta)\right\rangle \equiv \frac{\oint \frac{A(r,\theta)dl_p}{B_p}}{\oint \frac{dl_p}{B_p}} = \frac{\oint A(r,\theta)\, z(r,\theta)\, dl_p}{\oint z(r,\theta)\, dl_p} \tag{4}$$

where

$$z(r,\theta) \equiv \frac{\cos(x\sin\theta) + \frac{\partial R_0}{\partial r}\cos\theta + \left[s_\kappa - s_\delta\cos\theta + (1+s_\kappa)x\cos\theta\right]\sin\theta\sin(\theta + x\sin\theta)}{\left[\sin^2(\theta + x\sin\theta)(1+x\cos\theta)^2 + \kappa^2\cos^2\theta\right]^{1/2} \Big/ \left[R_0(r) + r\cos\left[\theta + x\sin\theta\right]\right]} \tag{5}$$

and the differential poloidal length is (see Fig. 3)

$$dl_p = r\sqrt{\left[\cos^2(\theta + x\sin\theta) + \kappa^2\sin^2\theta\right]}d\theta \tag{6}$$

Equivalent toroidal models

Simple toroidal models are widely used for transport calculations and experimental data interpretation (e.g Ref. 1). The usual flux surface model implicitly assumed in such codes, which will be referred to as the "elliptical" model" is (e.g. Ref. 1) $R = R_0 + r\cos\theta, Z = \kappa r\sin\theta$, $B_p = B_{p0}\Big/\left(1 + \frac{r}{R_0}\cos\theta\right)$. The usual approach is to construct an effective toroidal or cylindrical model that preserves the area of flux surface, which for this model leads to a relation between the effective radius variable $\bar{r}$ of the equivalent torus and the actual radial variable in the horizontal midplane r given in the elliptical model by $\bar{r} = r\sqrt{\frac{1}{2}\left(1+\kappa^2\right)}$.

Such equivalent models should be improved by using instead the Miller equilibrium. The area of the flux surface ψ passing through the midplane radius r is

$$A(\psi) = \oint_{\psi} dl_p \int_0^{2\pi} h_\phi d\phi = 2\pi \oint_{\psi} R dl_p$$
$$= 2\pi r R_0(r) \int_0^{2\pi} \left[1 + \frac{r}{R_0(r)} \cos(\theta + x \sin\theta) \right] \left[\cos^2(\theta + x\sin\theta) + \kappa^2 \sin^2\theta \right]^{1/2} d\theta \tag{7}$$

The area of a cylinder with radial variable $\bar{r}$ is $A_c(\bar{r}) = 2\pi R_0(a) 2\pi \bar{r}$. Equating the two areas and solving for

$$\bar{r} = r \frac{R_0(r)}{2\pi R_0(a)} \int_0^{2\pi} \left[1 + \frac{r}{R_0(r)} \cos(\theta + x\sin\theta) \right] \left[\cos^2(\theta + x\sin\theta) + \kappa^2 \sin^2\theta \right]^{1/2} d\theta \tag{8}$$

defines the radial variable of an equivalent cylinder that preserves the surface area of the Miller equilibrium flux surface.

A comparison calculation was made for a plasma representative of shot 98889 with minor horizontal radius a = 0.583 m, varying triangularity, elongation $\kappa = 1.75$, and major radius $R_0(a) = 1.77m$. The elliptical model predicts for these parameters an effective circular plasma radius $\bar{a} = 0.830\,m$. Evaluation of Eq. (8) with $x = \sin^{-1}\delta$ yields almost the same value of $\bar{a} = 0.817m$ for $\delta = 0$, as shown in Table 1. For non-zero values of the triangularity, the Miller model predicts increasingly smaller equivalent cylindrical radii than the elliptical model to preserve surface area.

Table 1 Effect of triangularity on effective cylindrical radius and $G(a, \theta = 0)$

δ triangularity	$\bar{a}(m)$ Miller equil.	$\bar{a}(m)$ elliptic equil	$G(a,\theta=0)$ Miller equil.	$G(a,\theta=0)$ elliptic equil
0.0	0.817	0.830	1.73	1.43
0.1	0.800	“	1.73	“
0.2	0.784	“	1.73	“
0.3	0.769	“	1.73	“
0.4	0.753	“	1.72	“
0.5	0.739	“	1.71	“
0.6	0.725	“	1.69	“
0.7	0.710	“	1.66	“
0.8	0.696	“	1.62	“
0.9	0.680	“	1.55	“

Interpretation of thermal conductivities from measured temperature gradients

Another application of the Miller equilibrium that immediately comes to mind is in the inference of experimental thermal diffusivities from measured temperature gradients in tokamaks. The measured temperature gradient $(dT/dr)_{\exp}$ pertains of course to the location $\left(r,\theta_{\exp}\right)$ at which the measurement is made (although sometimes it is mapped along flux surfaces to another location such as the outboard midplane at $\left(r,\theta=0\right)$). On the other hand, one-dimensional radial transport codes calculate an average conductive heat flux $<q\left(r\right)>$. In order to use the calculated average heat flux and the local (in θ) measured temperature gradient in the heat conduction relation to infer a measured thermal diffusivity $\chi=-q/n\left(dT/dr\right)\equiv qL_T/nT$, the local temperature gradient scale length must be mapped into an average value over the flux surface

$$\begin{aligned}(L_T)_{\exp} &\equiv -T(dr/dT)_{\exp} \Rightarrow <L_T> = -T\left(dr/dT\right)_{\exp}\left(<dr>/dr\left(\theta_{\exp}\right)\right)\\ &\equiv \left(L_T\right)_{\exp}\left(<dr>/dr\left(\theta_{\exp}\right)\right) = \left(L_T\right)_{\exp}\left(\left|\nabla r\left(\theta_{\exp}\right)\right|/<\left|\nabla r\right|>\right)\end{aligned} \tag{9}$$

From Eq. (2), the local $\left|\nabla r\right|$ may be written

$$\left|\nabla r\left(r,\theta\right)\right| = \frac{\kappa^{-1}\left[\sin^2\left(\theta+x\sin\theta\right)\left(1+x\cos\theta\right)^2+\kappa^2\cos^2\theta\right]^{1/2}}{\cos\left(x\sin\theta\right)+\dfrac{\partial R_0}{\partial r}\cos\theta+\left[s_\kappa-s_\delta\cos\theta+(1+s_\kappa)x\cos\theta\right]\sin\theta\sin\left(\theta+x\sin\theta\right)} \tag{10}$$

Using this in Eq. (4) yields an expression for the FSA value

$$\left\langle\left|\nabla r\left(r\right)\right|\right\rangle = \frac{\int_0^{2\pi}\left[R_0\left(r\right)+r\cos\left(\theta+x\sin\theta\right)\right]\left[\cos^2\left(\theta+x\sin\theta\right)+\kappa^2\sin^2\theta\right]^{1/2}d\theta}{\int_0^{2\pi}F\left(r,\theta\right)\left[R_0\left(r\right)+r\cos\left(\theta+x\sin\theta\right)\right]\left[\cos^2\left(\theta+x\sin\theta\right)+\kappa^2\sin^2\theta\right]^{1/2}d\theta} \tag{11}$$

where

$$F\left(r,\theta\right) = \frac{\cos\left(x\sin\theta\right)+\dfrac{\partial R_0}{\partial r}\cos\theta+\left[s_\kappa-s_\delta\cos\theta+(1+s_\kappa)x\cos\theta\right]\sin\theta\sin\left(\theta+x\sin\theta\right)}{\kappa^{-1}\left[\sin^2\left(\theta+x\sin\theta\right)\left(1+x\cos\theta\right)^2+\kappa^2\cos^2\theta\right]^{1/2}} \tag{12}$$

The FSA value of the temperature gradient scale length, $\left\langle L_T\right\rangle=-\left\langle T/\left(dT/dr\right)\right\rangle$, which is the quantity needed for the inference of experimental thermal diffusivity using the average heat

flux calculated by 1D transport codes, is related to the local value of the temperature gradient scale length, $L_T(\theta) = -T(\theta)/(dT/dr)_\theta$, which is the quantity measured, by

$$\frac{\langle L_T(r)\rangle}{L_T(r,\theta)} = \frac{|\nabla r(r,\theta)|}{\langle|\nabla r(r)|\rangle} \equiv G(r,\theta) \tag{13}$$

For the case $\theta = 0$, corresponding to the outboard midplane location of the measured gradient scale lengths, Eq. (10) reduces to the Shafranov shift correction

$$|\nabla(r,\theta=0)| = \frac{1}{\left(1+\partial R_0/\partial r\right)} \tag{14}$$

A series of calculations was performed for the same plasma model (representative of shot 98889) with minor horizontal radius a = 0.583 m, varying triangularity, elongation $\kappa = 1.75$, and major radius $R_0(a) = 1.77m$, using Eqs. (10)-(13) with $s_\kappa = 0, s_\delta = 0$ and using the elliptical model discussed in the previous section, for which $G(r,\theta=0) = \sqrt{\frac{1}{2}(1+\kappa^2)}$. The results are shown in Table 1. The Miller model predicts values of $G(a,\theta=0)$ that are 10-20% larger than those predicted by the elliptical model.

Neglecting the effect of the radial variation of the elongation and triangularity ($s_\kappa = 0, s_\delta = 0$) and also momentarily neglecting the triangularity ($\delta = 0$), reduces Eq. (13) to a form that more readily exhibits the various factors involved

$$\frac{\langle L_T(r)\rangle}{L_T(r,\theta=0)} = G(r,\theta=0) = \frac{\int_0^{2\pi} \frac{\kappa\left[1+\frac{\partial R_0}{\partial r}\cos\theta\right]}{\left[1+(\kappa^2-1)\cos^2\theta\right]^{1/2}}\left[R_0 + r\cos\theta\right]\left[1+(\kappa^2-1)\sin^2\theta\right]^{1/2} d\theta}{\left[1+\frac{\partial R_0}{\partial r}\right]\int_0^{2\pi}\left[R_0 + r\cos\theta\right]\left[1+(\kappa^2-1)\sin^2\theta\right]^{1/2} d\theta} \tag{15}$$

Prediction of poloidal distribution of conductive heat flux

One-dimensional transport codes calculate an average conductive heat flux, $\langle q\rangle$, over the flux surface. Assuming that the density, temperature and thermal diffusivity are uniform over the flux surface, the poloidal dependence of the conductive heat flux must arise through the poloidal dependence of the radial temperature gradient

$$q(r,\theta) = n(r)T(r)\chi(r)L_T^{-1}(r,\theta) = n(r)T(r)\chi(r)\langle L_T(r)\rangle^{-1} G(r,\theta) \tag{16}$$

The value of $G(r,\theta) \equiv q(r,\theta)/\langle q(r)\rangle \equiv \langle L_T(r)\rangle / L_T(r,\theta)$ calculated from Eqs. (10)-(13) at the separatrix $(r \to a)$ of the shot 98889 model previously described $(\Delta' = -0.25, \kappa = 1.75, r/R = 1/3)$ is plotted in Fig. 4. The bunching of the flux surfaces at the outboard midplane and the elongation at the top and bottom of the plasma account for the distribution.

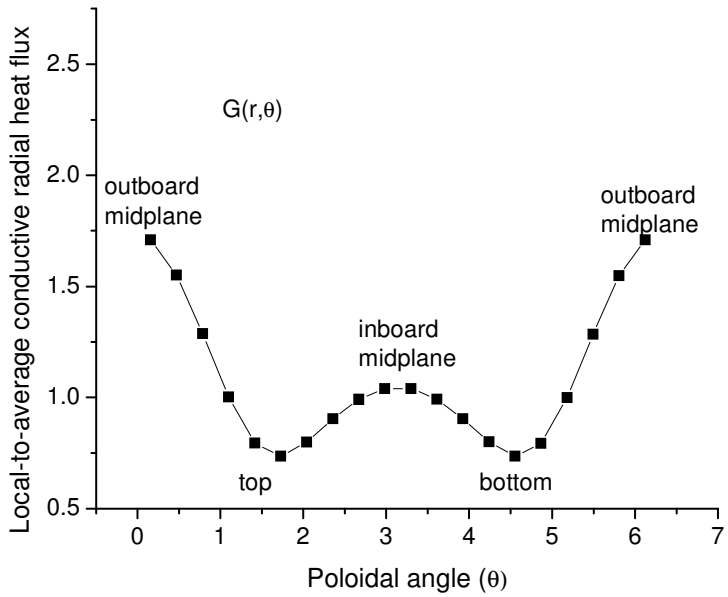

Figure 4 Predicted poloidal distribution of the conductive heat flux at the separatrix for a DIII-D shot 98889 model.

Relation to various HEP benchmarking calculations

The 2D codes (UEDGE[4] and SOLPS[5]) calculate $q(r,\theta_{\exp})$ at the location of the measured temperature gradient $L_T(r,\theta_{\exp})$ directly, and the two quantities can be directly combined to infer the experimental thermal diffusivity $\chi_{\exp} \equiv q(r,\theta_{\exp}) L_T(r,\theta_{\exp}) / nT$.

The 1.5D (2D MHD, 1D transport) codes (ONE-TWO[2] and ASTRA[3]) use the calculated 2D MHD equilibrium to construct an equivalent 1D transport model, from which is calculated a FSA value of $\langle q(r)\rangle$. In order to evaluate the experimental thermal diffusivity, it is then necessary either to map this average heat flux to a local value at the location of the measurement, $q(r,\theta_{\exp}) = G(r,\theta_{\exp})\langle q(r)\rangle$ or equivalently to map the measured value of the temperature gradient to an average value over the flux surface, $\langle L_T(r)\rangle = G(r,\theta_{\exp}) L_T(r,\theta_{\exp})$. In either

case, the resulting expression for the inferred experimental thermal diffusivity is $\chi_{\exp} \equiv G\left(r,\theta_{\exp}\right)\left\langle q\left(r\right)\right\rangle L_T\left(r,\theta_{\exp}\right)/nT$. The 2D MHD calculation in principle uses the quantities necessary to evaluate the mapping function $G\left(r,\theta_{\exp}\right)$. Alternatively, this function can be evaluated from the Miller equilibrium or the simpler elliptical equilibrium.

The 1D codes[1] use an effective cylinder with radius $\bar{r} = r\sqrt{\left(1+\kappa^2\right)/2}$; $1.4r$ (which preserves the surface area of an elliptical equilibrium with elongation κ) to calculate a FSA value of $\left\langle q\left(r\right)\right\rangle$. In this approximation $\left\langle L_T\left(r\right)\right\rangle / L_T\left(r,\theta_{\exp}=0)\right) = \bar{a}/a = \sqrt{\left(1+\kappa^2\right)/2}$; 1.4. Using the improved Miller approximation that retains triangularity dependence, rather than the elliptical approximation, results in an equivalent radius about 7% smaller, hence a heat flux about 7% larger, than with the elliptical approximation. The Miller equilibrium also leads to $\left\langle L_T\left(r\right)\right\rangle / L_T\left(r,\theta_{\exp}=0)\right)$; 1.7 , instead of the elliptical value of 1.4. Thus, using the Miller equilibrium instead of the elliptical equilibrium in the 1D calculations[1] would be roughly estimated to increase the inferred thermal diffusivities $\chi_{\exp} = \left\langle q\right\rangle\left\langle L_T\right\rangle / nT$ by about 30% for the parameters that characterize the benchmark problems. Note that Callen's formula[6] yields a somewhat smaller value of $\left\langle L_T\left(r\right)\right\rangle / L_T\left(r,\theta_{\exp}=0)\right)$; $\sqrt{S(r,\theta=0)} = \sqrt{\frac{2\kappa^2}{\left(1+\kappa^2\right)}\left(1-2\Delta'\right)} = 1.5$.

References

1. W. M. Stacey and R. J. Groebner, Phys. Plasmas, 13, 072510 (2006); 14, 012501 (2007).
2. H. L. St. John, "Equations and Associated Definitions used in ONE-TWO", General Atomics report (2005).
3. J. Kinsey and G. Bateman, Phys. Plasmas, 3, 3344 (1996).
4. T. D. Rognlien, D. D. Ryutov, N. Mattor and G. D. Porter, Phys. Plasmas, 5, 1851 (1999); Contrib. Plasma Phys., 38, 152 (1998); Plasma Phys. Control. Fusion, 47, A283 (2005)
5. V. A. Rozhansky, S. P. Voskoboynikov, E. G. Kaveeva, D. P. Coster and R. Schneider, Nucl. Fusion, 41, 387 (2001);42, 1110 (2002); 43, 614 (2003); Contrib. Plasma Phys., 46,575 (2006).
6. J. D. Callen,"Poloidal Variation of Radial Heat Flow in Tokamak Edge Plasmas" University of Wisconsin report (2008).
7. R. L. Miller, M.S. Chu, J. M. Greene, et al., Phys. Plasmas, 5, 973 (1998).
8. L. L. Lao, S. P. Hirshman and J. Wieland, Phys. Fluids, 24, 1431 (1981).

V. HEP BENCHMARKING ACTIVITY

(W. M. Stacey, *Georgia Tech)*

Abstract

A group of people are collaborating in the comparison experimental thermal diffusivities inferred from experimental data measured in the edge pedestal of DIII-D H-mode discharges using different codes. I am providing calculations based on a 1D edge transport code (as described in section II and Ref. 1), Rich Groebner (*General Atomics)* is providing calculations based on the 1.5D transport/MHD code ONE-TWO[2], Tarig Rafiq (*Lehigh*) is providing calculations based on the Multimode transport model in the 1.5D transport/MHD code ASTRA[3], Tom Rognlien (*Lawrence Livermore National Laboratory*) is providing calculations based on the 2D transport code UEDGE[4], and Larry Owen and John Canick (*Oak Ridge National Laboratory*) are providing calculations based on the 2D transport code SOLPS[5]. Jim Callen (*Wisconsin*) is coordinating the activity.

A. <u>1D Transport Calculations</u>

My calculations for the two shots initially being considered by the group are shown in Figs 1 and 2. The edge pedestal plasma density in shot 98889 is about 1/2 of the edge density in shot 118897, as a consequence of which the neutral penetration is much greater for 98889, resulting in charge exchange being the dominant heating/cooling mechanism in the very edge for 98889 and resulting in very different heat flux profiles for the two shots. The inferred experimental chi profiles in the edge are also quite different for the two cases. The calculation procedure is described fairly succinctly in Ref. 1.

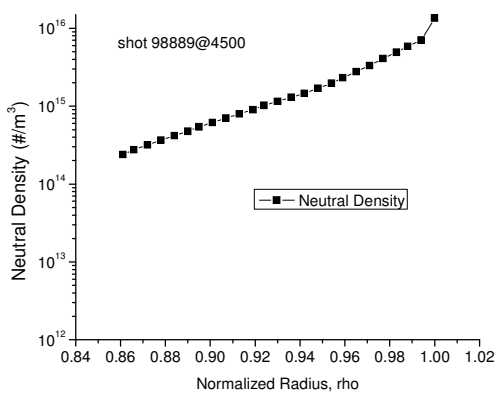

Fig. 1a Neutral Density
Shot 98889@4500

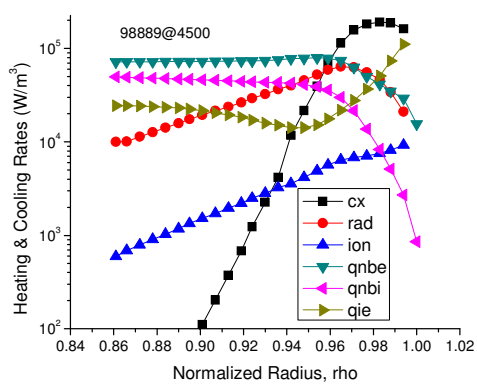

Fig. 1b Heating & Cooling Rates
Shot 98889@4500

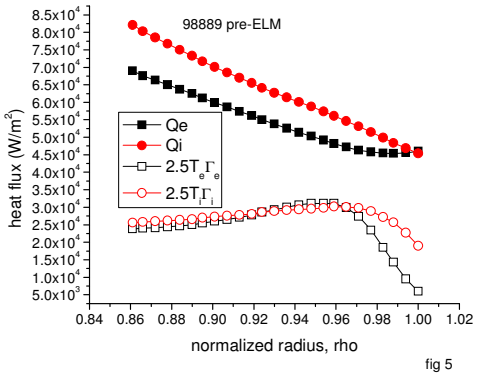

Fig. 1c Total & Convective Heat Fluxes Shot 98889@4500

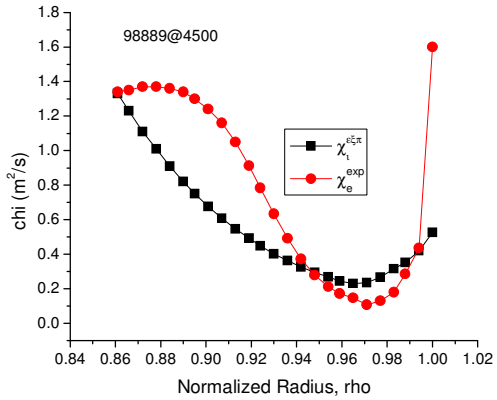

Fig. 1d χ_e & χ_i Experimental Shot 98889@4500

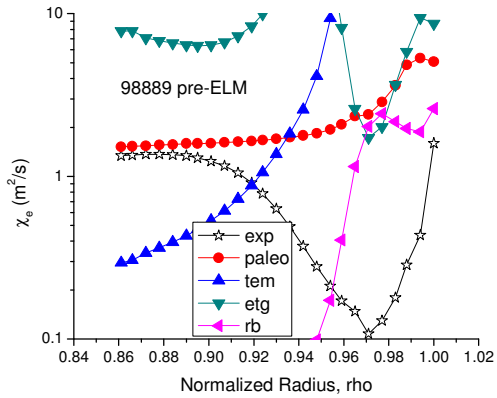

Fig. 1e Electron χ Shot 98889@4500

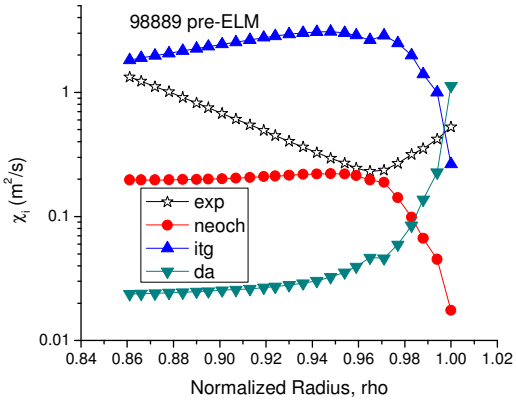

Fig.1f Ion χ Shot 98889@4500

.

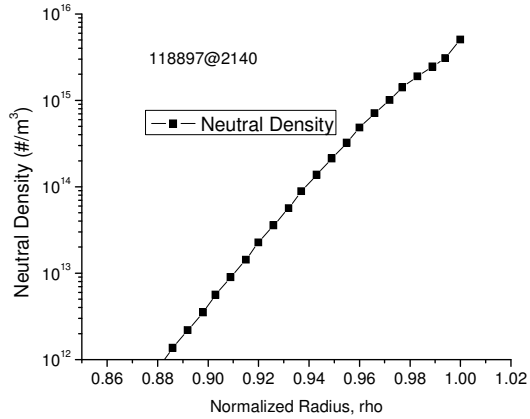

Fig. 2a Neutral Density Shot 118897@2140.

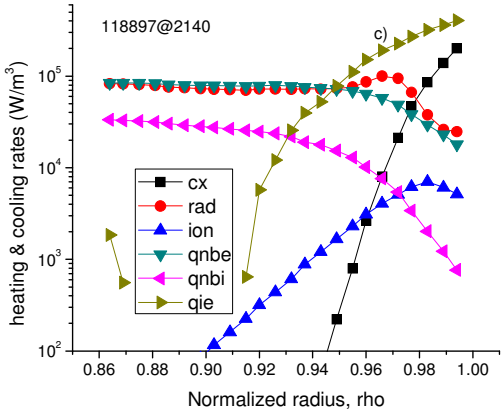

Fig. 2b Heating & Cooling Rates Shot 118897@2140.

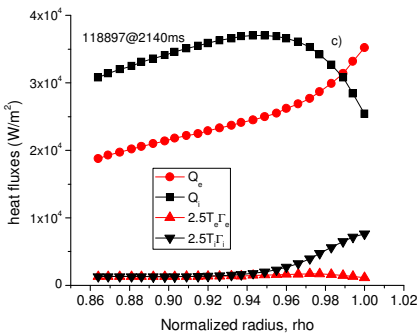

Fig. 2c Total & Convective Heat Fluxes Shot 118897@2140.

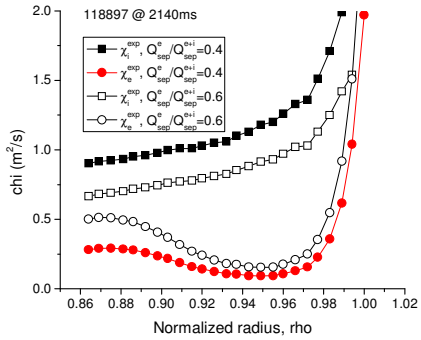

Fig. 2d. χ_e & χ_i Experimental Shot 118897@2140.

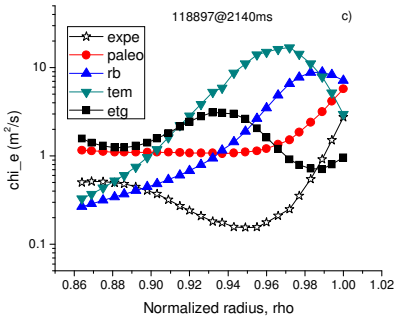

Fig. 2e Electron χ Shot 118897@2140.

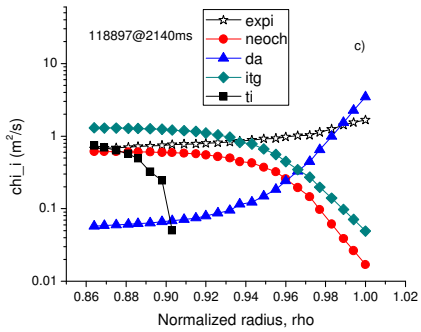

Fig. 2f Ion χ Shot 118897@2140.

B. Applications of the Miller Equilibrium to the Poloidal Variation of Temperature Gradients and Conductive Heat Fluxes

Stimulated by the relatively good agreement between the approximate formulas for the poloidal variation of the conductive heat flux that Callen derived[6] from the Miller equilibrium[7] with the calculations by the 2D codes, this formalism has been developed further, essentially retaining the dependence on triangularity and retaining an arbitrary poloidal location for measured temperature gradient in the Miller equilibrium. The result is an expression for the quantity $G(r,\theta) \equiv q(r,\theta)/\langle q(r)\rangle \equiv \langle L_T(r)\rangle / L_T(r,\theta)$ which relates the local and flux surface averaged conductive heat fluxes or temperature gradient scale lengths.

Miller equilibrium

Miller, et al.[7] derived analytical expressions for an equilibrium flux surface in a plasma as shown in Figure 3 with elongation κ, triangularity δ, and displaced centers $R_0(r)$, where r is

the half-diameter of the plasma along the midplane with center located at distance $R_0(r)$ from the toroidal centerline.

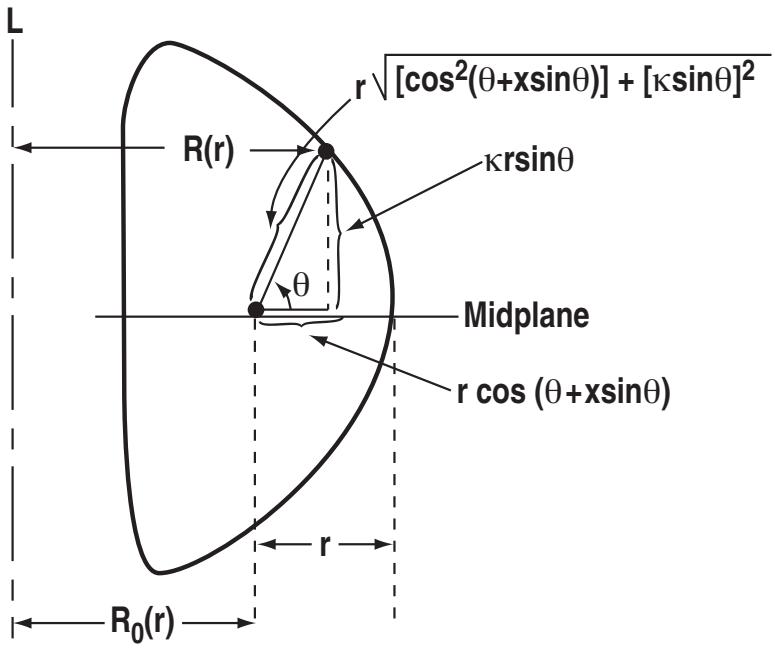

Figure 3 Miller equilibrium parameters

The R and Z coordinates of this plasma are described by[7]

$$R(r) = R_0(r) + r\cos\left[\theta + x\sin\theta\right]$$
$$Z(r) = \kappa r \sin\theta \tag{1}$$

where $x \equiv \sin^{-1}\delta$.

The poloidal magnetic field in such flux surface geometry is[7]

$$RB_p = \left|\nabla\phi\times\nabla\psi\right| = \frac{\partial\psi}{\partial r}\left|\nabla r\right|$$
$$= \frac{\frac{\partial\psi}{\partial r}\kappa^{-1}\left[\sin^2(\theta + x\sin\theta)(1 + x\cos\theta)^2 + \kappa^2\cos^2\theta\right]^{1/2}}{\cos(x\sin\theta) + \frac{\partial R_0}{\partial r}\cos\theta + \left[s_\kappa - s_\delta\cos\theta + (1+s_\kappa)x\cos\theta\right]\sin\theta\sin(\theta + x\sin\theta)} \tag{2}$$

where $s_\kappa = \frac{r}{\kappa}\frac{\partial\kappa}{\partial r}$ and $s_\delta = r\frac{\partial\delta}{\partial r}/\sqrt{(1-\delta^2)}$ account for the change in elongation and triangularity, respectively, with radial location.

The shifted circle model (which leads to the Shafranov shift) yields

$$\frac{\partial R_0}{\partial r} \equiv \Delta' = -\frac{r}{R_0}\left(\beta_p + \frac{1}{2}l_i\right) \tag{3a}$$

and a shifted ellipse model by Lao, et al.[8] yields

$$\frac{\partial R_0}{\partial r} = -\frac{r}{R_0}\left[\frac{2\left(\kappa^2+1\right)}{\left(3\kappa^2+1\right)}\left(\beta_p + \frac{1}{2}l_i\right) + \frac{1}{2}\frac{\left(\kappa^2-1\right)}{\left(3\kappa^2+1\right)}\right] \tag{3b}$$

Flux surface average

The flux surface average (FSA) of a quantity $A(r,\theta)$ in this flux surface geometry is

$$\left\langle A(r,\theta)\right\rangle \equiv \frac{\oint \frac{A(r,\theta)dl_p}{B_p}}{\oint \frac{dl_p}{B_p}} = \frac{\oint A(r,\theta)\, z(r,\theta)\, dl_p}{\oint z(r,\theta)\, dl_p} \tag{4}$$

where

$$z(r,\theta) \equiv \frac{\cos(x\sin\theta) + \frac{\partial R_0}{\partial r}\cos\theta + \left[s_\kappa - s_\delta\cos\theta + (1+s_\kappa)x\cos\theta\right]\sin\theta\sin(\theta + x\sin\theta)}{\left[\sin^2(\theta + x\sin\theta)(1+x\cos\theta)^2 + \kappa^2\cos^2\theta\right]^{1/2} \Big/ \left[R_0(r) + r\cos\left[\theta + x\sin\theta\right]\right]} \tag{5}$$

and the differential poloidal length is (see Fig. 3)

$$dl_p = r\sqrt{\left[\cos^2(\theta + x\sin\theta) + \kappa^2\sin^2\theta\right]}d\theta \tag{6}$$

Equivalent toroidal models

Simple toroidal models are widely used for transport calculations and experimental data interpretation (e.g Ref. 1). The usual flux surface model implicitly assumed in such codes, which will be referred to as the "elliptical" model" is (e.g. Ref. 1) $R = R_0 + r\cos\theta, Z = \kappa r\sin\theta$, $B_p = B_{p0}\Big/\left(1 + \frac{r}{R_0}\cos\theta\right)$. The usual approach is to construct an effective toroidal or cylindrical model that preserves the area of flux surface, which for this model leads to a relation between the effective radius variable $\bar{r}$ of the equivalent torus and the actual radial variable in the horizontal midplane r given in the elliptical model by $\bar{r} = r\sqrt{\frac{1}{2}\left(1+\kappa^2\right)}$.

Such equivalent models should be improved by using instead the Miller equilibrium. The area of the flux surface ψ passing through the midplane radius r is

$$A(\psi) = \oint_{\psi} dl_p \int_0^{2\pi} h_\phi d\phi = 2\pi \oint_{\psi} R dl_p$$
$$= 2\pi r R_0(r) \int_0^{2\pi} \left[1 + \frac{r}{R_0(r)} \cos(\theta + x \sin\theta) \right] \left[\cos^2(\theta + x\sin\theta) + \kappa^2 \sin^2\theta \right]^{1/2} d\theta \tag{7}$$

The area of a cylinder with radial variable $\bar{r}$ is $A_c(\bar{r}) = 2\pi R_0(a) 2\pi \bar{r}$. Equating the two areas and solving for

$$\bar{r} = r \frac{R_0(r)}{2\pi R_0(a)} \int_0^{2\pi} \left[1 + \frac{r}{R_0(r)} \cos(\theta + x\sin\theta) \right] \left[\cos^2(\theta + x\sin\theta) + \kappa^2 \sin^2\theta \right]^{1/2} d\theta \tag{8}$$

defines the radial variable of an equivalent cylinder that preserves the surface area of the Miller equilibrium flux surface.

A comparison calculation was made for a plasma representative of shot 98889 with minor horizontal radius a = 0.583 m, varying triangularity, elongation $\kappa = 1.75$, and major radius $R_0(a) = 1.77m$. The elliptical model predicts for these parameters an effective circular plasma radius $\bar{a} = 0.830\,m$. Evaluation of Eq. (8) with $x = \sin^{-1}\delta$ yields almost the same value of $\bar{a} = 0.817m$ for $\delta = 0$, as shown in Table 1. For non-zero values of the triangularity, the Miller model predicts increasingly smaller equivalent cylindrical radii than the elliptical model to preserve surface area.

Table 1 Effect of triangularity on effective cylindrical radius and $G(a, \theta = 0)$

δ triangularity	$\bar{a}(m)$ Miller equil.	$\bar{a}(m)$ elliptic equil	$G(a,\theta=0)$ Miller equil.	$G(a,\theta=0)$ elliptic equil
0.0	0.817	0.830	1.73	1.43
0.1	0.800	“	1.73	“
0.2	0.784	“	1.73	“
0.3	0.769	“	1.73	“
0.4	0.753	“	1.72	“
0.5	0.739	“	1.71	“
0.6	0.725	“	1.69	“
0.7	0.710	“	1.66	“
0.8	0.696	“	1.62	“
0.9	0.680	“	1.55	“

Interpretation of thermal conductivities from measured temperature gradients

Another application of the Miller equilibrium that immediately comes to mind is in the inference of experimental thermal diffusivities from measured temperature gradients in tokamaks. The measured temperature gradient $(dT/dr)_{\exp}$ pertains of course to the location $\left(r,\theta_{\exp}\right)$ at which the measurement is made (although sometimes it is mapped along flux surfaces to another location such as the outboard midplane at $\left(r,\theta=0\right)$). On the other hand, one-dimensional radial transport codes calculate an average conductive heat flux $<q\left(r\right)>$. In order to use the calculated average heat flux and the local (in θ) measured temperature gradient in the heat conduction relation to infer a measured thermal diffusivity $\chi=-q/n\left(dT/dr\right)\equiv qL_T/nT$, the local temperature gradient scale length must be mapped into an average value over the flux surface

$$\begin{aligned}(L_T)_{\exp} &\equiv -T(dr/dT)_{\exp} \Rightarrow <L_T> = -T\left(dr/dT\right)_{\exp}\left(<dr>/dr\left(\theta_{\exp}\right)\right)\\ &\equiv \left(L_T\right)_{\exp}\left(<dr>/dr\left(\theta_{\exp}\right)\right) = \left(L_T\right)_{\exp}\left(\left|\nabla r\left(\theta_{\exp}\right)\right|/<\left|\nabla r\right|>\right)\end{aligned} \tag{9}$$

From Eq. (2), the local $\left|\nabla r\right|$ may be written

$$\left|\nabla r\left(r,\theta\right)\right| = \frac{\kappa^{-1}\left[\sin^2\left(\theta+x\sin\theta\right)\left(1+x\cos\theta\right)^2+\kappa^2\cos^2\theta\right]^{1/2}}{\cos\left(x\sin\theta\right)+\dfrac{\partial R_0}{\partial r}\cos\theta+\left[s_\kappa-s_\delta\cos\theta+(1+s_\kappa)x\cos\theta\right]\sin\theta\sin\left(\theta+x\sin\theta\right)} \tag{10}$$

Using this in Eq. (4) yields an expression for the FSA value

$$\left\langle\left|\nabla r\left(r\right)\right|\right\rangle = \frac{\int_0^{2\pi}\left[R_0\left(r\right)+r\cos\left(\theta+x\sin\theta\right)\right]\left[\cos^2\left(\theta+x\sin\theta\right)+\kappa^2\sin^2\theta\right]^{1/2}d\theta}{\int_0^{2\pi}F\left(r,\theta\right)\left[R_0\left(r\right)+r\cos\left(\theta+x\sin\theta\right)\right]\left[\cos^2\left(\theta+x\sin\theta\right)+\kappa^2\sin^2\theta\right]^{1/2}d\theta} \tag{11}$$

where

$$F\left(r,\theta\right) = \frac{\cos\left(x\sin\theta\right)+\dfrac{\partial R_0}{\partial r}\cos\theta+\left[s_\kappa-s_\delta\cos\theta+(1+s_\kappa)x\cos\theta\right]\sin\theta\sin\left(\theta+x\sin\theta\right)}{\kappa^{-1}\left[\sin^2\left(\theta+x\sin\theta\right)\left(1+x\cos\theta\right)^2+\kappa^2\cos^2\theta\right]^{1/2}} \tag{12}$$

The FSA value of the temperature gradient scale length, $\left\langle L_T\right\rangle=-\left\langle T/\left(dT/dr\right)\right\rangle$, which is the quantity needed for the inference of experimental thermal diffusivity using the average heat

flux calculated by 1D transport codes, is related to the local value of the temperature gradient scale length, $L_T(\theta) = -T(\theta)/(dT/dr)_\theta$, which is the quantity measured, by

$$\frac{\langle L_T(r)\rangle}{L_T(r,\theta)} = \frac{|\nabla r(r,\theta)|}{\langle|\nabla r(r)|\rangle} \equiv G(r,\theta) \tag{13}$$

For the case $\theta = 0$, corresponding to the outboard midplane location of the measured gradient scale lengths, Eq. (10) reduces to the Shafranov shift correction

$$|\nabla(r,\theta=0)| = \frac{1}{\left(1+\partial R_0/\partial r\right)} \tag{14}$$

A series of calculations was performed for the same plasma model (representative of shot 98889) with minor horizontal radius a = 0.583 m, varying triangularity, elongation $\kappa = 1.75$, and major radius $R_0(a) = 1.77m$, using Eqs. (10)-(13) with $s_\kappa = 0, s_\delta = 0$ and using the elliptical model discussed in the previous section, for which $G(r,\theta=0) = \sqrt{\frac{1}{2}(1+\kappa^2)}$. The results are shown in Table 1. The Miller model predicts values of $G(a,\theta=0)$ that are 10-20% larger than those predicted by the elliptical model.

Neglecting the effect of the radial variation of the elongation and triangularity ($s_\kappa = 0, s_\delta = 0$) and also momentarily neglecting the triangularity ($\delta = 0$), reduces Eq. (13) to a form that more readily exhibits the various factors involved

$$\frac{\langle L_T(r)\rangle}{L_T(r,\theta=0)} = G(r,\theta=0) = \frac{\int_0^{2\pi} \frac{\kappa\left[1+\frac{\partial R_0}{\partial r}\cos\theta\right]}{\left[1+(\kappa^2-1)\cos^2\theta\right]^{1/2}}\left[R_0 + r\cos\theta\right]\left[1+(\kappa^2-1)\sin^2\theta\right]^{1/2} d\theta}{\left[1+\frac{\partial R_0}{\partial r}\right]\int_0^{2\pi}\left[R_0 + r\cos\theta\right]\left[1+(\kappa^2-1)\sin^2\theta\right]^{1/2} d\theta} \tag{15}$$

Prediction of poloidal distribution of conductive heat flux

One-dimensional transport codes calculate an average conductive heat flux, $\langle q\rangle$, over the flux surface. Assuming that the density, temperature and thermal diffusivity are uniform over the flux surface, the poloidal dependence of the conductive heat flux must arise through the poloidal dependence of the radial temperature gradient

$$q(r,\theta)=n(r)T(r)\chi(r)L_T^{-1}(r,\theta)=n(r)T(r)\chi(r)\langle L_T(r)\rangle^{-1}G(r,\theta) \tag{16}$$

The value of $G(r,\theta)\equiv q(r,\theta)/\langle q(r)\rangle\equiv\langle L_T(r)\rangle/L_T(r,\theta)$ calculated from Eqs. (10)-(13) at the separatrix $(r\to a)$ of the model problem previously described $(\Delta'=-0.25,\kappa=1.75,r/R=1/3)$ is plotted in Fig. 4 The curve labeled symmetric uses averaged values $\kappa=1.77,\delta=0.14$ for all values of θ, while the curve labeled asymmetric uses experimental values $\kappa_{top}=1.50,\delta_{top}=0.0$ in the upper half $0\le\theta\le\pi$ and $\kappa=2.32,\delta=0.14$ in the lower half $\pi\le\theta\le 2\pi$.

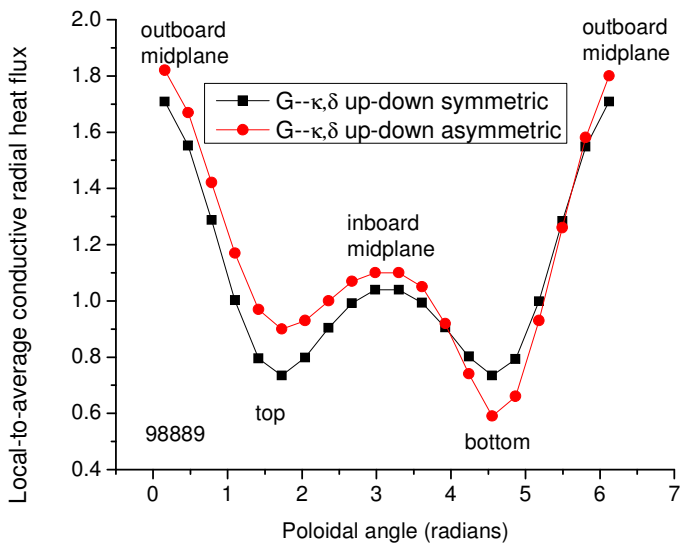

Figure 4 Predicted poloidal distribution of the conductive heat flux at the separatrix for a DIII-D shot 98889 model.

Relation to various HEP benchmarking calculations

The 2D codes (UEDGE[4] and SOLPS[5]) calculate $q(r,\theta_{\exp})$ at the location of the measured temperature gradient $L_T(r,\theta_{\exp})$ directly, and the two quantities can be directly combined to infer the experimental thermal diffusivity $\chi_{\exp}\equiv q(r,\theta_{\exp})L_T(r,\theta_{\exp})/nT$.

The 1.5D (2D MHD, 1D transport) codes (ONE-TWO[2] and ASTRA[3]) use the calculated 2D MHD equilibrium to construct an equivalent 1D transport model, from which is calculated a FSA value of $\langle q(r)\rangle$. In order to evaluate the experimental thermal diffusivity, it is then necessary either to map this average heat flux to a local value at the location of the measurement, $q(r,\theta_{\exp})=G(r,\theta_{\exp})\langle q(r)\rangle$ or equivalently to map the measured value of the temperature gradient to an average value over the flux surface, $\langle L_T(r)\rangle=G(r,\theta_{\exp})L_T(r,\theta_{\exp})$. In either

case, the resulting expression for the inferred experimental thermal diffusivity is $\chi_{\exp} \equiv G\left(r,\theta_{\exp}\right)\left\langle q\left(r\right)\right\rangle L_T\left(r,\theta_{\exp}\right)/nT$. The 2D MHD calculation in principle uses the quantities necessary to evaluate the mapping function $G\left(r,\theta_{\exp}\right)$. Alternatively, this function can be evaluated from the Miller equilibrium or the simpler elliptical equilibrium.

The 1D codes[1] use an effective cylinder with radius $\bar{r} = r\sqrt{\left(1+\kappa^2\right)/2}$; $1.4r$ (which preserves the surface area of an elliptical equilibrium with elongation κ) to calculate a FSA value of $\left\langle q\left(r\right)\right\rangle$. In this approximation $\left\langle L_T\left(r\right)\right\rangle / L_T\left(r,\theta_{\exp}=0)\right) = \bar{a}/a = \sqrt{\left(1+\kappa^2\right)/2}$; 1.4. Using the improved Miller approximation that retains triangularity dependence, rather than the elliptical approximation, results in an equivalent radius about 7% smaller, hence a heat flux about 7% larger, than with the elliptical approximation. The Miller equilibrium also leads to $\left\langle L_T\left(r\right)\right\rangle / L_T\left(r,\theta_{\exp}=0)\right)$; 1.7 , instead of the elliptical value of 1.4. Thus, using the Miller equilibrium instead of the elliptical equilibrium in the 1D calculations[1] would be roughly estimated to increase the inferred thermal diffusivities $\chi_{\exp} = \left\langle q\right\rangle\left\langle L_T\right\rangle / nT$ by about 30% for the parameters that characterize the benchmark problems. Note that Callen's formula[6] yields a somewhat smaller value of $\left\langle L_T\left(r\right)\right\rangle / L_T\left(r,\theta_{\exp}=0)\right)$; $\sqrt{S(r,\theta=0)} = \sqrt{\frac{2\kappa^2}{\left(1+\kappa^2\right)}\left(1-2\Delta'\right)} = 1.5$.

References

1. W. M. Stacey and R. J. Groebner, Phys. Plasmas, 13, 072510 (2006); 14, 012501 (2007).
2. H. L. St. John, "Equations and Associated Definitions used in ONE-TWO", General Atomics report (2005).
3. J. Kinsey and G. Bateman, Phys. Plasmas, 3, 3344 (1996).
4. T. D. Rognlien, D. D. Ryutov, N. Mattor and G. D. Porter, Phys. Plasmas, 5, 1851 (1999); Contrib. Plasma Phys., 38, 152 (1998); Plasma Phys. Control. Fusion, 47, A283 (2005)
5. V. A. Rozhansky, S. P. Voskoboynikov, E. G. Kaveeva, D. P. Coster and R. Schneider, Nucl. Fusion, 41, 387 (2001);42, 1110 (2002); 43, 614 (2003); Contrib. Plasma Phys., 46,575 (2006).
6. J. D. Callen,"Poloidal Variation of Radial Heat Flow in Tokamak Edge Plasmas" University of Wisconsin report (2008).
7. R. L. Miller, M.S. Chu, J. M. Greene, et al., Phys. Plasmas, 5, 973 (1998).
8. L. L. Lao, S. P. Hirshman and J. Wieland, Phys. Fluids, 24, 1431 (1981).

V. HEP BENCHMARKING ACTIVITY

(W. M. Stacey, *Georgia Tech)*

Abstract

A group of people are collaborating in the comparison experimental thermal diffusivities inferred from experimental data measured in the edge pedestal of DIII-D H-mode discharges using different codes. I am providing calculations based on a 1D edge transport code (as described in section II and Ref. 1), Rich Groebner (*General Atomics)* is providing calculations based on the 1.5D transport/MHD code ONE-TWO[2], Tarig Rafiq (*Lehigh*) is providing calculations based on the Multimode transport model in the 1.5D transport/MHD code ASTRA[3], Tom Rognlien (*Lawrence Livermore National Laboratory*) is providing calculations based on the 2D transport code UEDGE[4], and Larry Owen and John Canick (*Oak Ridge National Laboratory*) are providing calculations based on the 2D transport code SOLPS[5]. Jim Callen (*Wisconsin*) is coordinating the activity.

A. <u>1D Transport Calculations</u>

My calculations for the two shots initially being considered by the group are shown in Figs 1 and 2. The edge pedestal plasma density in shot 98889 is about 1/2 of the edge density in shot 118897, as a consequence of which the neutral penetration is much greater for 98889, resulting in charge exchange being the dominant heating/cooling mechanism in the very edge for 98889 and resulting in very different heat flux profiles for the two shots. The inferred experimental chi profiles in the edge are also quite different for the two cases. The calculation procedure is described fairly succinctly in Ref. 1.

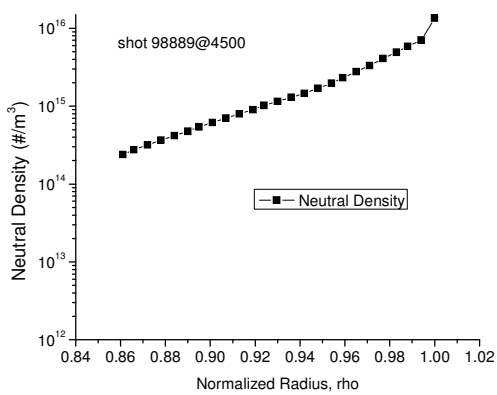

Fig. 1a Neutral Density
Shot 98889@3960

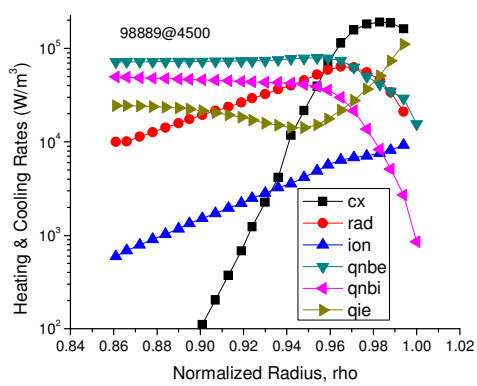

Fig. 1b Heating & Cooling Rates
Shot 98889@3960

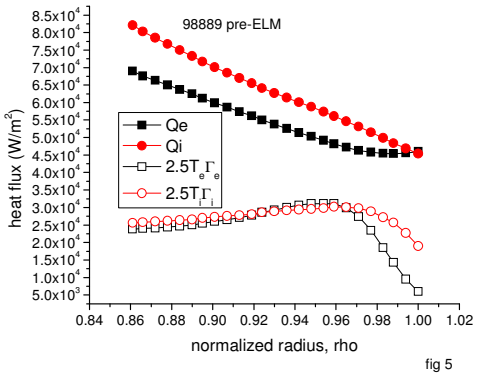

Fig. 1c Total & Convective Heat Fluxes Shot 98889@3960

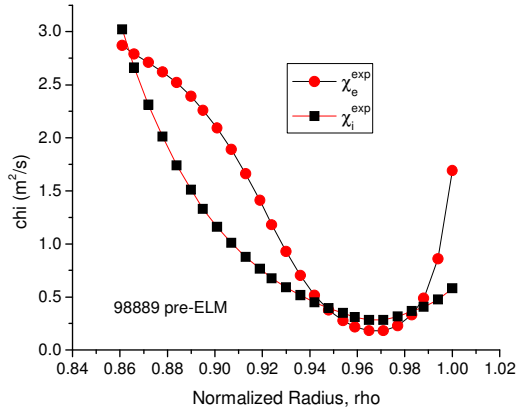

Fig. 1d χ_e & χ_i Experimental Shot 98889@3960

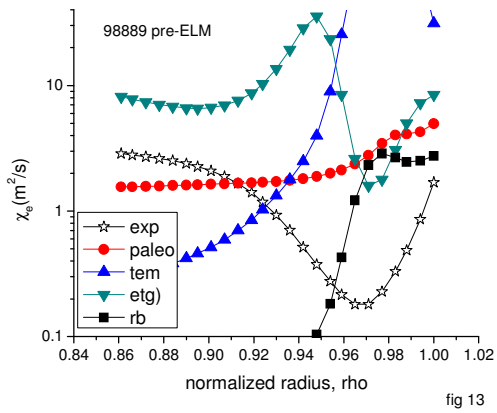

Fig. 1e Electron χ Shot 98889@3960

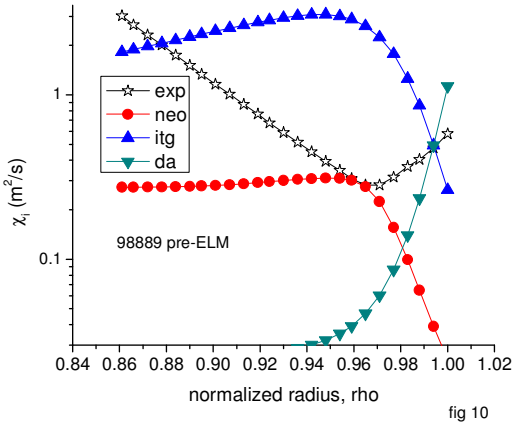

Fig.1f Ion χ Shot 98889@3960

.

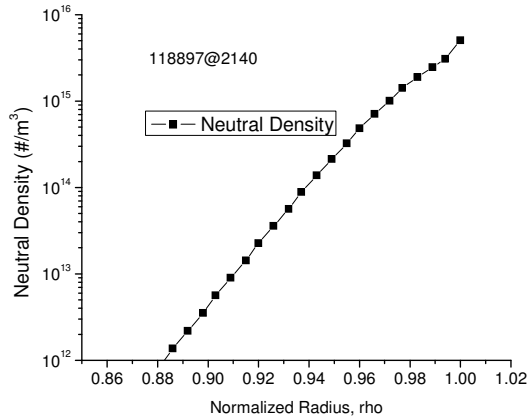

Fig. 2a Neutral Density Shot 118897@2140.

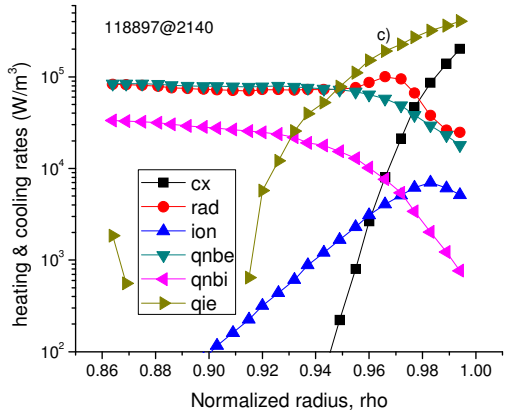

Fig. 2b Heating & Cooling Rates Shot 118897@2140.

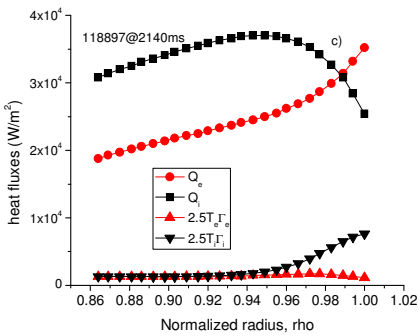

Fig. 2c Total & Convective Heat Fluxes Shot 118897@2140.

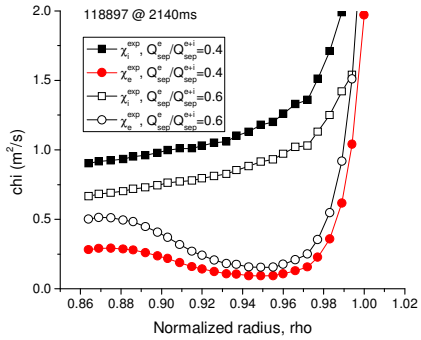

Fig. 2d. χ_e & χ_i Experimental Shot 118897@2140.

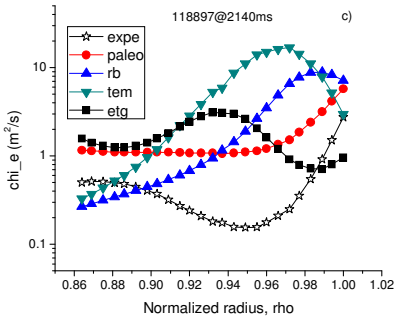

Fig. 2e Electron χ Shot 118897@2140.

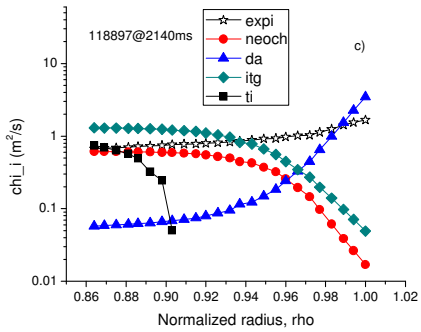

Fig. 2f Ion χ Shot 118897@2140.

B. Applications of the Miller Equilibrium to the Poloidal Variation of Temperature Gradients and Conductive Heat Fluxes

Stimulated by the relatively good agreement between the approximate formulas for the poloidal variation of the conductive heat flux that Callen derived[6] from the Miller equilibrium[7] with the calculations by the 2D codes, this formalism has been developed further, essentially retaining the dependence on triangularity and retaining an arbitrary poloidal location for measured temperature gradient in the Miller equilibrium. The result is an expression for the quantity $G(r,\theta) \equiv q(r,\theta)/\langle q(r)\rangle \equiv \langle L_T(r)\rangle / L_T(r,\theta)$ which relates the local and flux surface averaged conductive heat fluxes or temperature gradient scale lengths.

Miller equilibrium

Miller, et al.[7] derived analytical expressions for an equilibrium flux surface in a plasma as shown in Figure 3 with elongation κ, triangularity δ, and displaced centers $R_0(r)$, where r is

the half-diameter of the plasma along the midplane with center located at distance $R_0(r)$ from the toroidal centerline.

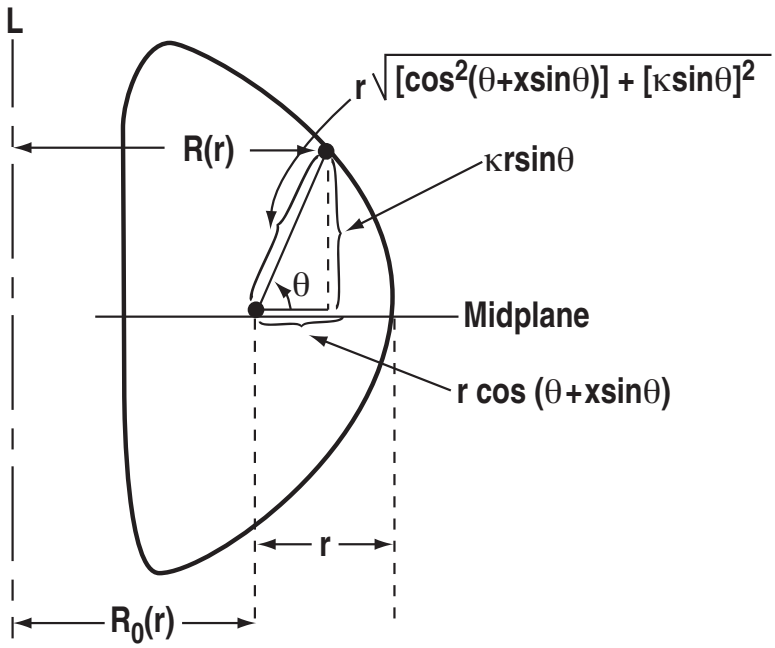

Figure 3 Miller equilibrium parameters

The R and Z coordinates of this plasma are described by[7]

$$R(r) = R_0(r) + r\cos\left[\theta + x\sin\theta\right]$$
$$Z(r) = \kappa r \sin\theta \tag{1}$$

where $x \equiv \sin^{-1}\delta$.

The poloidal magnetic field in such flux surface geometry is[7]

$$RB_p = \left|\nabla\phi\times\nabla\psi\right| = \frac{\partial\psi}{\partial r}\left|\nabla r\right|$$
$$= \frac{\frac{\partial\psi}{\partial r}\kappa^{-1}\left[\sin^2(\theta + x\sin\theta)(1 + x\cos\theta)^2 + \kappa^2\cos^2\theta\right]^{1/2}}{\cos(x\sin\theta) + \frac{\partial R_0}{\partial r}\cos\theta + \left[s_\kappa - s_\delta\cos\theta + (1+s_\kappa)x\cos\theta\right]\sin\theta\sin(\theta + x\sin\theta)} \tag{2}$$

where $s_\kappa = \frac{r}{\kappa}\frac{\partial\kappa}{\partial r}$ and $s_\delta = r\frac{\partial\delta}{\partial r}/\sqrt{(1-\delta^2)}$ account for the change in elongation and triangularity, respectively, with radial location.

The shifted circle model (which leads to the Shafranov shift) yields

$$\frac{\partial R_0}{\partial r} \equiv \Delta' = -\frac{r}{R_0}\left(\beta_p + \frac{1}{2}l_i\right) \tag{3a}$$

and a shifted ellipse model by Lao, et al.[8] yields

$$\frac{\partial R_0}{\partial r} = -\frac{r}{R_0}\left[\frac{2\left(\kappa^2+1\right)}{\left(3\kappa^2+1\right)}\left(\beta_p + \frac{1}{2}l_i\right) + \frac{1}{2}\frac{\left(\kappa^2-1\right)}{\left(3\kappa^2+1\right)}\right] \tag{3b}$$

Flux surface average

The flux surface average (FSA) of a quantity $A(r,\theta)$ in this flux surface geometry is

$$\left\langle A(r,\theta)\right\rangle \equiv \frac{\oint \frac{A(r,\theta)dl_p}{B_p}}{\oint \frac{dl_p}{B_p}} = \frac{\oint A(r,\theta)\, z(r,\theta)\, dl_p}{\oint z(r,\theta)\, dl_p} \tag{4}$$

where

$$z(r,\theta) \equiv \frac{\cos(x\sin\theta) + \frac{\partial R_0}{\partial r}\cos\theta + \left[s_\kappa - s_\delta\cos\theta + (1+s_\kappa)x\cos\theta\right]\sin\theta\sin(\theta + x\sin\theta)}{\left[\sin^2(\theta + x\sin\theta)(1+x\cos\theta)^2 + \kappa^2\cos^2\theta\right]^{1/2} \Big/ \left[R_0(r) + r\cos\left[\theta + x\sin\theta\right]\right]} \tag{5}$$

and the differential poloidal length is (see Fig. 3)

$$dl_p = r\sqrt{\left[\cos^2(\theta + x\sin\theta) + \kappa^2\sin^2\theta\right]}d\theta \tag{6}$$

Equivalent toroidal models

Simple toroidal models are widely used for transport calculations and experimental data interpretation (e.g Ref. 1). The usual flux surface model implicitly assumed in such codes, which will be referred to as the "elliptical" model" is (e.g. Ref. 1) $R = R_0 + r\cos\theta, Z = \kappa r\sin\theta$, $B_p = B_{p0}\Big/\left(1 + \frac{r}{R_0}\cos\theta\right)$. The usual approach is to construct an effective toroidal or cylindrical model that preserves the area of flux surface, which for this model leads to a relation between the effective radius variable $\bar{r}$ of the equivalent torus and the actual radial variable in the horizontal midplane r given in the elliptical model by $\bar{r} = r\sqrt{\frac{1}{2}\left(1+\kappa^2\right)}$.

Such equivalent models should be improved by using instead the Miller equilibrium. The area of the flux surface ψ passing through the midplane radius r is

$$A(\psi) = \oint_{\psi} dl_p \int_0^{2\pi} h_\phi d\phi = 2\pi \oint_{\psi} R dl_p$$
$$= 2\pi r R_0(r) \int_0^{2\pi} \left[1 + \frac{r}{R_0(r)} \cos(\theta + x \sin\theta) \right] \left[\cos^2(\theta + x\sin\theta) + \kappa^2 \sin^2\theta \right]^{1/2} d\theta \tag{7}$$

The area of a cylinder with radial variable $\bar{r}$ is $A_c(\bar{r}) = 2\pi R_0(a) 2\pi \bar{r}$. Equating the two areas and solving for

$$\bar{r} = r \frac{R_0(r)}{2\pi R_0(a)} \int_0^{2\pi} \left[1 + \frac{r}{R_0(r)} \cos(\theta + x\sin\theta) \right] \left[\cos^2(\theta + x\sin\theta) + \kappa^2 \sin^2\theta \right]^{1/2} d\theta \tag{8}$$

defines the radial variable of an equivalent cylinder that preserves the surface area of the Miller equilibrium flux surface.

A comparison calculation was made for a plasma representative of shot 98889 with minor horizontal radius a = 0.583 m, varying triangularity, elongation $\kappa = 1.75$, and major radius $R_0(a) = 1.77m$. The elliptical model predicts for these parameters an effective circular plasma radius $\bar{a} = 0.830\,m$. Evaluation of Eq. (8) with $x = \sin^{-1}\delta$ yields almost the same value of $\bar{a} = 0.817m$ for $\delta = 0$, as shown in Table 1. For non-zero values of the triangularity, the Miller model predicts increasingly smaller equivalent cylindrical radii than the elliptical model to preserve surface area.

Table 1 Effect of triangularity on effective cylindrical radius and $G(a, \theta = 0)$

δ triangularity	$\bar{a}(m)$ Miller equil.	$\bar{a}(m)$ elliptic equil	$G(a,\theta=0)$ Miller equil.	$G(a,\theta=0)$ elliptic equil
0.0	0.817	0.830	1.73	1.43
0.1	0.800	“	1.73	“
0.2	0.784	“	1.73	“
0.3	0.769	“	1.73	“
0.4	0.753	“	1.72	“
0.5	0.739	“	1.71	“
0.6	0.725	“	1.69	“
0.7	0.710	“	1.66	“
0.8	0.696	“	1.62	“
0.9	0.680	“	1.55	“

Interpretation of thermal conductivities from measured temperature gradients

Another application of the Miller equilibrium that immediately comes to mind is in the inference of experimental thermal diffusivities from measured temperature gradients in tokamaks. The measured temperature gradient $(dT/dr)_{\exp}$ pertains of course to the location $\left(r,\theta_{\exp}\right)$ at which the measurement is made (although sometimes it is mapped along flux surfaces to another location such as the outboard midplane at $\left(r,\theta=0\right)$). On the other hand, one-dimensional radial transport codes calculate an average conductive heat flux $<q\left(r\right)>$. In order to use the calculated average heat flux and the local (in θ) measured temperature gradient in the heat conduction relation to infer a measured thermal diffusivity $\chi=-q/n\left(dT/dr\right)\equiv qL_T/nT$, the local temperature gradient scale length must be mapped into an average value over the flux surface

$$\begin{aligned}(L_T)_{\exp} &\equiv -T(dr/dT)_{\exp} \Rightarrow <L_T> = -T\left(dr/dT\right)_{\exp}\left(<dr>/dr\left(\theta_{\exp}\right)\right)\\ &\equiv \left(L_T\right)_{\exp}\left(<dr>/dr\left(\theta_{\exp}\right)\right) = \left(L_T\right)_{\exp}\left(\left|\nabla r\left(\theta_{\exp}\right)\right|/<\left|\nabla r\right|>\right)\end{aligned} \tag{9}$$

From Eq. (2), the local $\left|\nabla r\right|$ may be written

$$\left|\nabla r\left(r,\theta\right)\right| = \frac{\kappa^{-1}\left[\sin^2\left(\theta+x\sin\theta\right)\left(1+x\cos\theta\right)^2+\kappa^2\cos^2\theta\right]^{1/2}}{\cos\left(x\sin\theta\right)+\dfrac{\partial R_0}{\partial r}\cos\theta+\left[s_\kappa-s_\delta\cos\theta+(1+s_\kappa)x\cos\theta\right]\sin\theta\sin\left(\theta+x\sin\theta\right)} \tag{10}$$

Using this in Eq. (4) yields an expression for the FSA value

$$\left\langle\left|\nabla r\left(r\right)\right|\right\rangle = \frac{\int_0^{2\pi}\left[R_0\left(r\right)+r\cos\left(\theta+x\sin\theta\right)\right]\left[\cos^2\left(\theta+x\sin\theta\right)+\kappa^2\sin^2\theta\right]^{1/2}d\theta}{\int_0^{2\pi}F\left(r,\theta\right)\left[R_0\left(r\right)+r\cos\left(\theta+x\sin\theta\right)\right]\left[\cos^2\left(\theta+x\sin\theta\right)+\kappa^2\sin^2\theta\right]^{1/2}d\theta} \tag{11}$$

where

$$F\left(r,\theta\right) = \frac{\cos\left(x\sin\theta\right)+\dfrac{\partial R_0}{\partial r}\cos\theta+\left[s_\kappa-s_\delta\cos\theta+(1+s_\kappa)x\cos\theta\right]\sin\theta\sin\left(\theta+x\sin\theta\right)}{\kappa^{-1}\left[\sin^2\left(\theta+x\sin\theta\right)\left(1+x\cos\theta\right)^2+\kappa^2\cos^2\theta\right]^{1/2}} \tag{12}$$

The FSA value of the temperature gradient scale length, $\left\langle L_T\right\rangle=-\left\langle T/\left(dT/dr\right)\right\rangle$, which is the quantity needed for the inference of experimental thermal diffusivity using the average heat

flux calculated by 1D transport codes, is related to the local value of the temperature gradient scale length, $L_T(\theta) = -T(\theta)/(dT/dr)_\theta$, which is the quantity measured, by

$$\frac{\langle L_T(r)\rangle}{L_T(r,\theta)} = \frac{|\nabla r(r,\theta)|}{\langle|\nabla r(r)|\rangle} \equiv G(r,\theta) \tag{13}$$

For the case $\theta = 0$, corresponding to the outboard midplane location of the measured gradient scale lengths, Eq. (10) reduces to the Shafranov shift correction

$$|\nabla(r,\theta=0)| = \frac{1}{\left(1+\partial R_0/\partial r\right)} \tag{14}$$

A series of calculations was performed for the same plasma model (representative of shot 98889) with minor horizontal radius a = 0.583 m, varying triangularity, elongation $\kappa = 1.75$, and major radius $R_0(a) = 1.77m$, using Eqs. (10)-(13) with $s_\kappa = 0, s_\delta = 0$ and using the elliptical model discussed in the previous section, for which $G(r,\theta=0) = \sqrt{\frac{1}{2}(1+\kappa^2)}$. The results are shown in Table 1. The Miller model predicts values of $G(a,\theta=0)$ that are 10-20% larger than those predicted by the elliptical model.

Neglecting the effect of the radial variation of the elongation and triangularity ($s_\kappa = 0, s_\delta = 0$) and also momentarily neglecting the triangularity ($\delta = 0$), reduces Eq. (13) to a form that more readily exhibits the various factors involved

$$\frac{\langle L_T(r)\rangle}{L_T(r,\theta=0)} = G(r,\theta=0) = \frac{\int_0^{2\pi} \frac{\kappa\left[1+\frac{\partial R_0}{\partial r}\cos\theta\right]}{\left[1+(\kappa^2-1)\cos^2\theta\right]^{1/2}}\left[R_0 + r\cos\theta\right]\left[1+(\kappa^2-1)\sin^2\theta\right]^{1/2} d\theta}{\left[1+\frac{\partial R_0}{\partial r}\right]\int_0^{2\pi}\left[R_0 + r\cos\theta\right]\left[1+(\kappa^2-1)\sin^2\theta\right]^{1/2} d\theta} \tag{15}$$

Prediction of poloidal distribution of conductive heat flux

One-dimensional transport codes calculate an average conductive heat flux, $\langle q\rangle$, over the flux surface. Assuming that the density, temperature and thermal diffusivity are uniform over the flux surface, the poloidal dependence of the conductive heat flux must arise through the poloidal dependence of the radial temperature gradient

$$q(r,\theta)=n(r)T(r)\chi(r)L_T^{-1}(r,\theta)=n(r)T(r)\chi(r)\langle L_T(r)\rangle^{-1}G(r,\theta) \tag{16}$$

The value of $G(r,\theta)\equiv q(r,\theta)/\langle q(r)\rangle\equiv\langle L_T(r)\rangle/L_T(r,\theta)$ calculated from Eqs. (10)-(13) at the separatrix $(r\to a)$ of the model problem previously described $(\Delta'=-0.25,\kappa=1.75,r/R=1/3)$ is plotted in Fig. 4 The curve labeled symmetric uses averaged values $\kappa=1.77,\delta=0.14$ for all values of θ, while the curve labeled asymmetric uses experimental values $\kappa_{top}=1.50,\delta_{top}=0.0$ in the upper half $0\le\theta\le\pi$ and $\kappa=2.32,\delta=0.14$ in the lower half $\pi\le\theta\le 2\pi$.

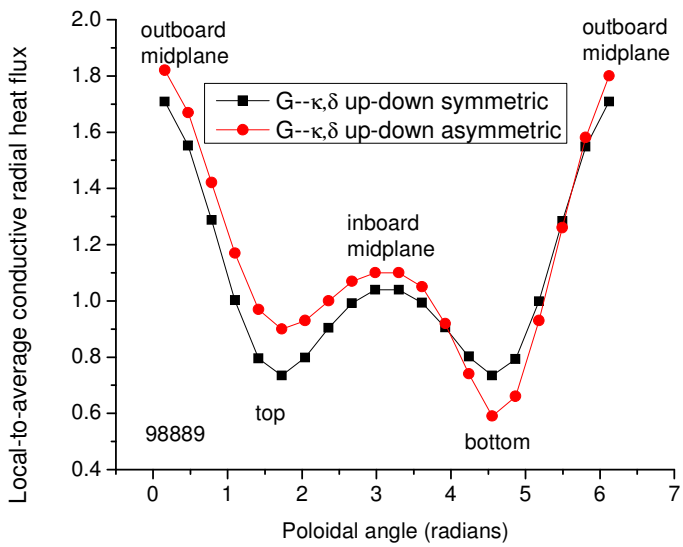

Figure 4 Predicted poloidal distribution of the conductive heat flux at the separatrix for a DIII-D shot 98889 model.

Relation to various HEP benchmarking calculations

The 2D codes (UEDGE[4] and SOLPS[5]) calculate $q(r,\theta_{\exp})$ at the location of the measured temperature gradient $L_T(r,\theta_{\exp})$ directly, and the two quantities can be directly combined to infer the experimental thermal diffusivity $\chi_{\exp}\equiv q(r,\theta_{\exp})L_T(r,\theta_{\exp})/nT$.

The 1.5D (2D MHD, 1D transport) codes (ONE-TWO[2] and ASTRA[3]) use the calculated 2D MHD equilibrium to construct an equivalent 1D transport model, from which is calculated a FSA value of $\langle q(r)\rangle$. In order to evaluate the experimental thermal diffusivity, it is then necessary either to map this average heat flux to a local value at the location of the measurement, $q(r,\theta_{\exp})=G(r,\theta_{\exp})\langle q(r)\rangle$ or equivalently to map the measured value of the temperature gradient to an average value over the flux surface, $\langle L_T(r)\rangle=G(r,\theta_{\exp})L_T(r,\theta_{\exp})$. In either

case, the resulting expression for the inferred experimental thermal diffusivity is $\chi_{\exp} \equiv G\left(r,\theta_{\exp}\right)\left\langle q\left(r\right)\right\rangle L_T\left(r,\theta_{\exp}\right)/nT$. The 2D MHD calculation in principle uses the quantities necessary to evaluate the mapping function $G\left(r,\theta_{\exp}\right)$. Alternatively, this function can be evaluated from the Miller equilibrium or the simpler elliptical equilibrium.

The 1D codes[1] use an effective cylinder with radius $\bar{r} = r\sqrt{\left(1+\kappa^2\right)/2} = 1.4r$ (which preserves the surface area of an elliptical equilibrium with elongation κ) to calculate a FSA value of $\left\langle q\left(r\right)\right\rangle$. In this approximation $\left\langle L_T\left(r\right)\right\rangle / L_T\left(r,\theta_{\exp}=0)\right) = \bar{a}/a = \sqrt{\left(1+\kappa^2\right)/2} = 1.4$. Using the improved Miller approximation that retains triangularity dependence, rather than the elliptical approximation, results in an equivalent radius about 7% smaller, hence a heat flux about 7% larger, than with the elliptical approximation. The Miller equilibrium also leads to $\left\langle L_T\left(r\right)\right\rangle / L_T\left(r,\theta_{\exp}=0)\right) = 1.7$, instead of the elliptical value of 1.4. Thus, using the Miller equilibrium instead of the elliptical equilibrium in the 1D calculations[1] would be roughly estimated to increase the inferred thermal diffusivities $\chi_{\exp} = \left\langle q\right\rangle\left\langle L_T\right\rangle / nT$ by about 30% for the parameters that characterize the benchmark problems. Note that Callen's formula[6] yields a somewhat smaller value of $\left\langle L_T\left(r\right)\right\rangle / L_T\left(r,\theta_{\exp}=0)\right) = \sqrt{S(r,\theta=0)} = \sqrt{\frac{2\kappa^2}{\left(1+\kappa^2\right)}\left(1-2\Delta'\right)} = 1.5$.

References

1. W. M. Stacey and R. J. Groebner, Phys. Plasmas, 13, 072510 (2006); 14, 012501 (2007).
2. H. L. St. John, "Equations and Associated Definitions used in ONE-TWO", General Atomics report (2005).
3. J. Kinsey and G. Bateman, Phys. Plasmas, 3, 3344 (1996).
4. T. D. Rognlien, D. D. Ryutov, N. Mattor and G. D. Porter, Phys. Plasmas, 5, 1851 (1999); Contrib. Plasma Phys., 38, 152 (1998); Plasma Phys. Control. Fusion, 47, A283 (2005)
5. V. A. Rozhansky, S. P. Voskoboynikov, E. G. Kaveeva, D. P. Coster and R. Schneider, Nucl. Fusion, 41, 387 (2001);42, 1110 (2002); 43, 614 (2003); Contrib. Plasma Phys., 46,575 (2006).
6. J. D. Callen,"Poloidal Variation of Radial Heat Flow in Tokamak Edge Plasmas" University of Wisconsin report (2008).
7. R. L. Miller, M.S. Chu, J. M. Greene, et al., Phys. Plasmas, 5, 973 (1998).
8. L. L. Lao, S. P. Hirshman and J. Wieland, Phys. Fluids, 24, 1431 (1981).

VI. SABR FUEL CYCLE ANALYSIS

C. M. Sommer, W. Van Rooijen and W. M. Stacey, Georgia Tech

Abstract

Various fuel cycles for a sodium cooled, subcritical, fast reactor, SABR[1], with a fusion neutron source for the transmutation of light water reactor spent fuel have been analyzed. All fuel cycles were 4-batch, and all but one were constrained by a total fuel residence time consistent with a 200 dpa clad and structure materials damage limit. The objective of this study was to achieve greater than 90% burn up of the transuranics from the spent fuel, consistent with the Advanced Fuel Cycle objectives of DoE[2]. A more detailed account of this work can be found in the MS thesis of the first author[3].

A. SABR spent nuclear fuel transmutation reactor

SABR[1] is a TRU-metal-fueled, sodium cooled, subcritical fast transmutation reactor driven by a D-T fusion neutron source. Figure 1 shows a simplified three dimensional model of the reactor. An annular fission core contains metallic TRU fuel with initial weight percent composition of 40Zr-10Am-10Np-40Pu and maximum nominal operating temperature of 970 K. The core produces 3000MWth (83.3 kWth/kg TRU), with coolant nominal T_{in} = 650 K and T_{out} = 923 K. Reactivity decrease with fuel burnup is offset by increasing the fusion neutron source strength.

The fusion neutron source is surrounded on the outside by an annular fission core. Surrounding the fission core and the plasma there are tritium breeding blankets and several layers of shielding to protect the superconducting magnets that are used for the confinement of the plasma. The tokamak DT fusion neutron source for SABR is described in Ref. 4.

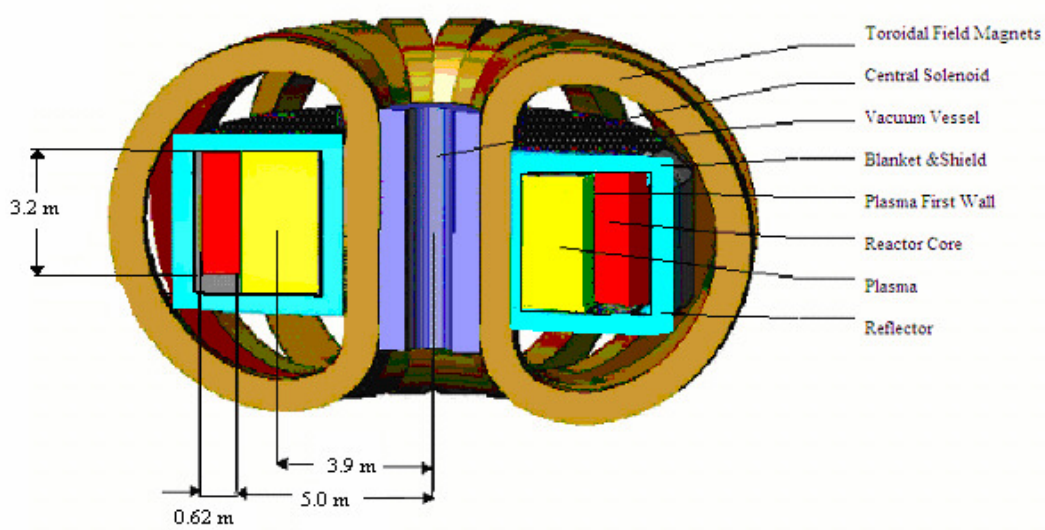

Figure 1: Configuration of SABR

B. Fuel cycle analysis

Five fuel cycle scenarios were investigated. The first two fuel cycle scenarios (A and B) examined the difference between in-to-out and out-to-in fuel shuffling for once-through fuel cycles (in the in-to-out scenario the fresh fuel batch is loaded next to the plasma source and shuffled successively outward, and vice-versa for the out-to-in scenario), and the third scenario (C) examined the effect of a design variation on power flattening. The fourth fuel cycle (D) examined the achievement of greater than 90% TRU burnup in a once-through fuel cycle, assuming the development of an advanced structural material that could withstand the associated radiation damage. Finally, the fifth fuel cycle (E) analysis, which is representative of the reference fuel cycle envisioned for advanced burner reactors (ABRs), examined the achievement of 90% TRU burnup by repeated reprocessing/recyling of the TRU fuel. The calculations for the fuel cycle of SABR were done by employing the TRITON/NEWT[5,6] package from SCALE5.1[7] and the neutronics code EVENT[8]. Cross sections were obtained fron NJOY[9]. A code was written to couple the cross section processing, the neutronics calculation and the depletion calculation in the fuel cycle.

A 4-batch fuel cycle was used in which the fuel resides for one burn cycle (of 750 days) in each of the four annular rings of the core, for a total fuel residence time (equal to 4 burn cycle times) of 3000 days, limited by the radiation damage to the clad and fuel assembly structure corresponding to 200 dpa. A "once-through" fuel cycle (in which "fresh" TRU fuel from SNF is loaded into one of the 4 rings at the beginning of each burn cycle and fuel which has been in residence for 4 burn cycles is removed and sent to a high level waste repository [HLWR]) achieves about 23% burnup (about 8.3 MT of TRU) before the fuel acquires 200 dpa and must be removed. A maximum k_{eff} = 0.95 occurs at beginning of life with fresh TRU fuel in all assemblies. Once such a fuel cycle reaches equilibrium, the values of k_{eff} at beginning and end of cycle (BOC and EOC) are about 0.90 and 0.85, which requires corresponding neutron source strengths in terms of P_{fusion} of about 180 and 240 MW, respectively, to maintain 3000 MWth fission power. The integral decay heat of the discharged fuel over 10^6 years is only reduced by a factor of about 2 (relative to the SNF discharged from LWRs) by such a "once-through" fuel cycle, implying a factor of 2 reduction in repository requirements. This fuel cycle provides a baseline of what can be accomplished without further reprocessing and recycling of the TRU fuel.

When the same 4-batch, 3000 day residence time fuel cycle is used but the fuel removed after 4 burn cycles is reprocessed and the TRU is recycled (together with "fresh" TRU from SNF), only the fission products and a small fraction of the actinides (0.15% Pu and Np, 0.03% Am) are sent to the HLWR after each reprocessing step. For such a "reprocessing" fuel cycle, the values of k_{eff} and P_{fusion} at BOC and EOC are about the same and the TRU burnup rates are slightly larger. The integral decay heat of material placed in a HLWR in such a reprocessing transmutation fuel cycle would be reduced to only 10% of the integral decay heat of the original SNF; i.e. the repository requirement is reduced by a factor of 10. SABR operating with 80% availability could support (i.e. burn the TRU in the discharged SNF of) four 1000 MWe LWRs.

If the 200 dpa radiation damage limit on fuel residence time could be relaxed, then greater TRU burnup could be achieved in a single residence time. A "once-though"

fuel cycle as described in the first paragraph, but now with four 3000 day burn cycles and a fuel residence time of 12,000 days (24.65 yr) was found to burn up 91.2% of the TRU fuel. Once such a fuel cycle reaches equilibrium, the values of k_{eff} at BOC and EOC are about 0.68 and 0.48, which require corresponding neutron source strengths in terms of P_{fusion} of about 433 and 663 MW, respectively, to maintain 3000 MWth fission power. It is feasible to modify the SABR neutron source to produce more than the present P_{fusion} = 500 MW design limit. However, the integral decay heat of the remaining 8.8% of the TRU and the fission products (hence the HLWR requirement) is only reduced by a factor of about 3 relative to SNF discharged from LWRs, and the power was so strongly peaked near the neutron source in such a far subcritical reactor as to make the practical design of such a reactor unattractive.

The reference fuel cycle, in which the TRU fuel was reprocessed, mixed with fresh TRU fuel, and recycled into the reactor (with an "out-to-in" shuffling pattern) after each 24% burnup residence time, achieved greater than 90% TRU burnup after 9 residence times. The fuel ultimately discharged to the high level waste repository (HLWR) was reduced relative to the original spent nuclear fuel (SNF) from which it was produced by 99% in integral decay heat at 100,000 years after discharge. The resulting repository volume required for the millennial storage of the fuel discharged from the SABR was calculated to be 1/130 the volume that would have been required to store the original SNF from which that fuel was made. Detailed properties of this fuel cycle are given in Table 1.

Table 1 Reference fuel cycle parameters

Parameter	Units	Values
Thermal Power	MW	3000
Cycles per Residence Time		4
Burn Cycle Length Time	Days	750
4 Batch Residence Time	Years	8.21
BOC keff		0.900
EOC keff		0.847
BOC Pfus	MW	181
EOC Pfus	MW	241
TRU BOC Loading	MT	36
Power Density	KW/kg	83.3
Power Peaking BOC		1.28
Power Peaking EOC		1.54
TRU Burned per Residence	%	23.6%

TRU Burned per Year	MT/FPY	1.03
TRU Burned per Residence	MT	8.496
SNF Disposed per Year	MT/FPY	103
LWR Support Ratio		4
Average Core Flux Across Cycle	n/cm^2-s	1.47E16
Average Fast (>0.1 MeV) Flux	n/cm^2-s	9.20E15
Fluence per Residence Time	n/cm^2	3.81E24
Fast Fluence per Residence Time	n/cm^2	5.75E15
Hardness of Spectrum	%	62.6%
Heat Load at 100,000 years	W/kg TRU Initial	.00187
Heat Load at 100,000 years SABR Input	W/kg TRU Initial	.127
Integral Heat Load	W/kg TRU Initial	667
Integral Heat Load SABR Input	W/kg TRU Initial	88705
Passes For 90% Burn Up	#	9
Repository Space Gain	Factor	129

C. Conclusions

A 4 batch fuel cycle representative of the ABR's fuel cycle envisioned by GNEP was explored. This 4 batch, 3000 day cycle with repeated reprocessing and recycling of the TRU fuel to achieve greater than 90% burnup of the fuel after 9 recycles. The decay heat to the repository in this cycle would be short term and caused by the fission products. The increase in repository space by a factor of 129 is due to only 1% of the TRU having to be placed in the repository. This fuel cycle is the reference cycle for SABR. It was chosen as the reference cycle, because it meets all of the design criteria: 1) minimizes power peaking, 2) achieves a high transmutation rate and reaches 90% burnup of the TRU, 3) produces enough tritium to maintain self sufficiency, 4) decreases the long term decay heat, 5) and it reduces the repository requirements for spent nuclear fuel by a factor of 10.

References

1. W. M. Stacey, et al., "A TRU-Zr Metal Fuel, Sodium Cooled, Fast Subcritical Advanced Burner Reactor", *Nucl. Technol.*, 162, 53 (2008).

2. DoE Global Nuclear Energy Partnership website http://www.gnep.energy.gov
3. C. M. Sommer, "Fuel Cycle Analysis for SABR", MS Thesis, Georgia Institute of Technology, 2008.
4. J. P. Floyd, et al., "Tokamak Fusion Neutron Source for a Fast Transmutation Reactor", Fusion Sci. Technol., 52, 727 (2007).
5. "Triton: A Two-Dimensional Depletion Sequence for Characterization of Spent Nuclear Fuel," NUREG/CR-200, Rev. 5., Vol. I Section T1, ORNL/NUREG/CSD-2/R7 (2006).
6. "NEWT: A New Transport Algorithm For Two-Dimensional Discrete Ordinates Analysis In Non-Orthogonal Geometries," NUREG/CR-200, Rev. 5.1, Vol. II Section F21, ORNL/NUREG/CSD-2/R7 (2006).
7.. "SCALE5.1: A Modular Code System for Performing Standardized Computer Analyses for Licensing Evaluation," NUREG/CR-0200, Rev. 5.1 (ORNL/NUREG/CSD-2/R5), Vold. I, II, and III, Oak Ridge National Laboratory/U.S. Nuclear Regulatory Commission (2006).
8. C. de OLIVEIRA and A.GODDARD, "EVENT—A Multi-dimensional Finite Element Spherical-Harmonics Radiation Transport Code," Proc. Int. Seminar *3-D Deterministic Radiation Transport Codes*, Paris, France, December 2–3, 1996, Organization for Economic Cooperation and Development (1996).
9. R.E. MACFARLANE & D.W. MUIR. "The NJOY Nuclear Data Processing System, Version 99," Los Alamos National Laboratory (1999

VII. SABR DYNAMIC SAFETY ANALYSIS

T. Sumner, W. M. Stacey and W. Van Rooijen, Georgia Tech

Abstract

A model was developed to simulate the coupled dynamics of a sub-critical fast reactor fueled with transuranics (TRU), a DT tokamak fusion neutron source and the heat removal and secondary systems. Several types of accident initiating events—inadvertent increases in the auxilliary power and fueling sources for the fusion neutron source, inadvertent control rod ejection from the reactor core, loss of flow (LOFA), and loss of heat sink (LOHSA)—were simulated in order to determine the time available to detect accident onset and take corrective action. A more detailed description is presented in Ref. 1.

A. SABR spent nuclear fuel transmutation reactor

SABR[2] is a TRU-metal-fueled, sodium cooled, subcritical fast transmutation reactor driven by a D-T fusion neutron source. Figure 1 shows a simplified three dimensional model of the reactor. An annular fission core contains metallic TRU fuel with initial weight percent composition of 40Zr-10Am-10Np-40Pu and maximum nominal operating temperature of 970 K. The core produces 3000MWth (83.3 kWth/kg TRU), with coolant nominal T_{in} = 650 K and T_{out} = 923 K. Reactivity decrease with fuel burnup is offset by increasing the fusion neutron source strength.

The fusion neutron source is surrounded on the outside by an annular fission core. Surrounding the fission core and the plasma there are tritium breeding blankets and several layers of shielding to protect the superconducting magnets that are used for the confinement of the plasma. The tokamak DT fusion neutron source for SABR is described in Ref. 3.

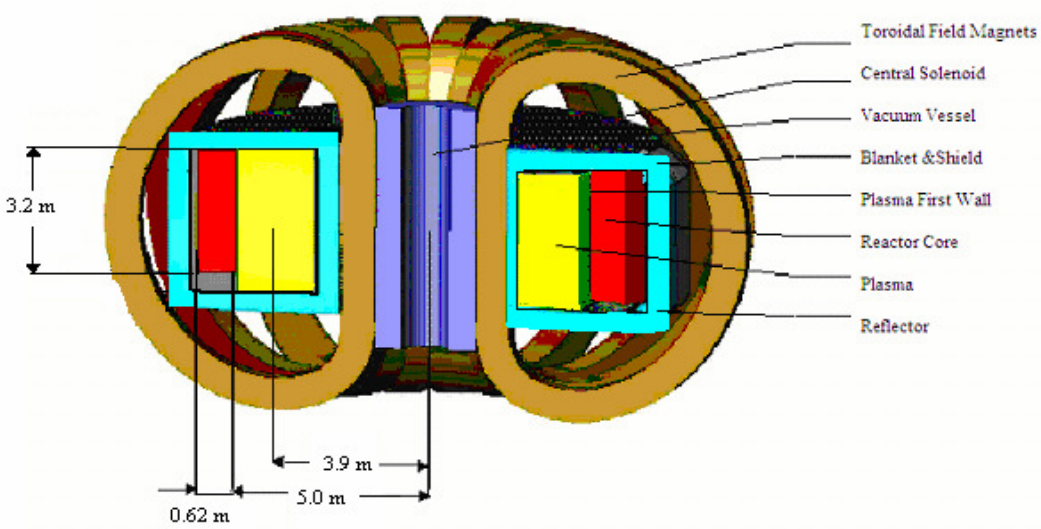

Figure 1: Configuration of SABR

B. Dynamical safety analyses

A Subcritical Advanced Burner Reactor)SABR) fueled with pure TRU (in order to maximize net TRU burnup) presents some safety issues relative to a similar reactor fueled with uranium. The delayed neutron fraction β is smaller for TRU than for U-235, meaning that the reactivity margin to prompt critical is smaller for TRU fueled reactors. The absence of U-238 removes the large negative fuel Doppler reactivity coefficient which limits inadvertent power excursions. Operating subcritical by an amount ρ increases the reactivity margin to prompt critical from β to $\rho+\beta >> \beta$ for SABR. Moreover, the dynamics of a subcritical reactor will differ from those of a critical reactor in several ways; e.g. there does not seem to be an inherent feedback mechanism that would shut off the neutron source if a fission power excursion started, control rod insertion would lead to a lower power operation of the fission reactor, not to complete shutdown, if the neutron source remained on. On the other hand, turning off the neutron source is a very effective way to shut down a subcritical reactor.

A model of the coupled dynamics of the fusion neutron source, the fission core, and the heat removal system has been implemented[1], and some initial simulations of reactor shutdown and of accidents in SABR have been simulated to determine how much time is available to detect an accident and shut down the neutron source before damage would occur (e.g. fuel melt at 1473 k, sodium boiling at 1156 K). Turning off the auxiliary heating power to the fusion neutron source was found to be an effective "scram" mechanism, shutting down the fission reactor within a few plasma energy confinement times, which is about a second. There are inherent "soft" plasma pressure and density limits that will inhibit any inadvertent plasma power excursion (hence neutron source excursion) by spoiling the plasma confinement and thus reducing the plasma power (hence neutron source).

Neutron source excursions

Simulation of neutron source excursions due to inadvertent increases in plasma heating or fueling indicated that the inherent plasma pressure limit (Troyon beta limit or Greenwald density limit) would limit fusion power excursions before fuel melting or sodium boiling occurred in the core, except for one case, as summarized in Tables 1 and 2. (BOL refers to beginning of core life, BOC refers to beginning of equilibrium fuel cycle, and EOC refers to end of equilibrium fuel cycle.). The auxiliary heating power for the fusion neutron source consists of 6 different 20 MW sources. Only when two of these sources are accidently turned on at beginning of core life would there be any core damage if corrective action were not taken.

.

Table 1: Summary of Accidental Plasma Auxiliary Heating Increases

(fuel melts @ 1473 K, sodium boils @ 1156 K)

	BOL	BOC	EOC
Max. Coolant Temperature for 20 MW increase in P_{aux} (K)	1,079	968	952
Max. Fuel Temperature for 20 MW increase in P_{aux} (K)	1,142	1,020	1,002
Max. Coolant Temperature for 40 MW increase in P_{aux} (K)	1,184*	1,003	976
Max. Fuel Temperature for 40 MW increase in P_{aux} (K)	1,259	1,058	1,028

The accidental increase in plasma fueling rate which would produce an increase in the plasma ion density and hence the fusion neutron production rate was simulated…In all cases the Troyon beta limit would be exceeded before the ion density increased enough to cause fuel melting or coolant boiling. Even if the density exceeding the Troyon beta limit did not limit the fusion neutron source excursion, the time between the initiation of the accident and coolant boilng or fuel melting was sufficiently long to enable the accident to be detected and corrective action to be taken.

Table 2: Summary of Accidental Plasma Ion Density Increases

	BOL	BOC	EOC
Allowable Plasma Ion Density Increase Before Coolant Boiling	12%	17%	19%
Time Until Coolant Boiling (seconds)	46	29	27
Allowable Plasma Ion Density Increase Before Fuel Melting	19%	29%	32%
Time Until Fuel Melting (seconds)	14	13	16
Maximum Plasma Ion Density Increase Before Troyon Beta Limit Exceeded	11%	1%	2%

Control rod ejection

Simulation of accidental control rod injection (+9$) in the most reactive condition resulted only in increase in fission power to a new equilibrium, with core temperatures remaining below levels at which either fuel melting or core boiling would occur.

Loss-of-flow-accidents (LOFAs)

Simulation of LOFAs indicate that a flow reduction of about 50% can be tolerated in SABR without turning off the neutron source, and that even with an unrealistic 100% loss of flow in the core there is about 24 seconds to shut off the neutron source before fuel melting occurs. The fuel and coolant maximum temperatures are plotted for 50, 65 and 80% loss-of-flow accidents in Figs. 2 and 3.

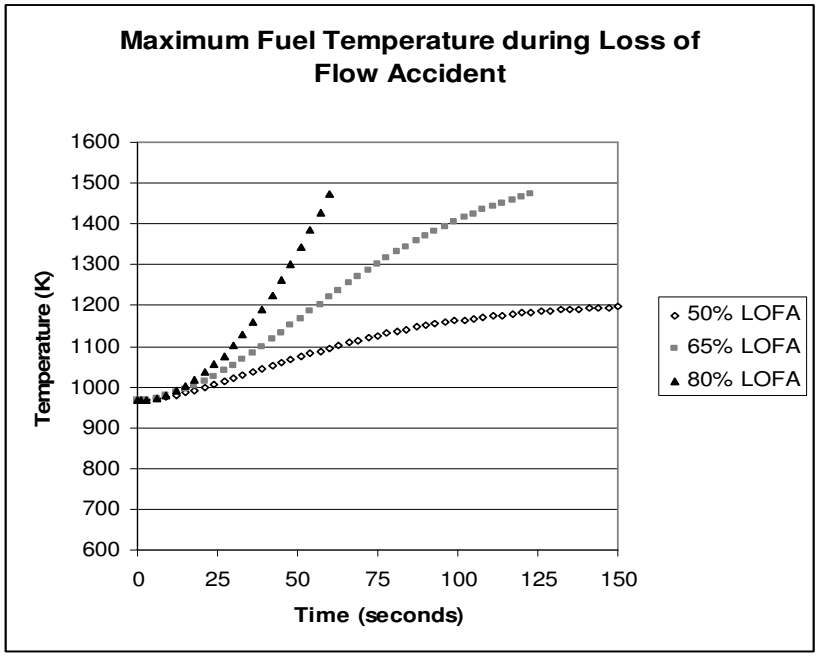

Figure 2: Maximum Fuel Temperature during Loss of Flow Accident at BOL (Fuel melting at 1473 K)

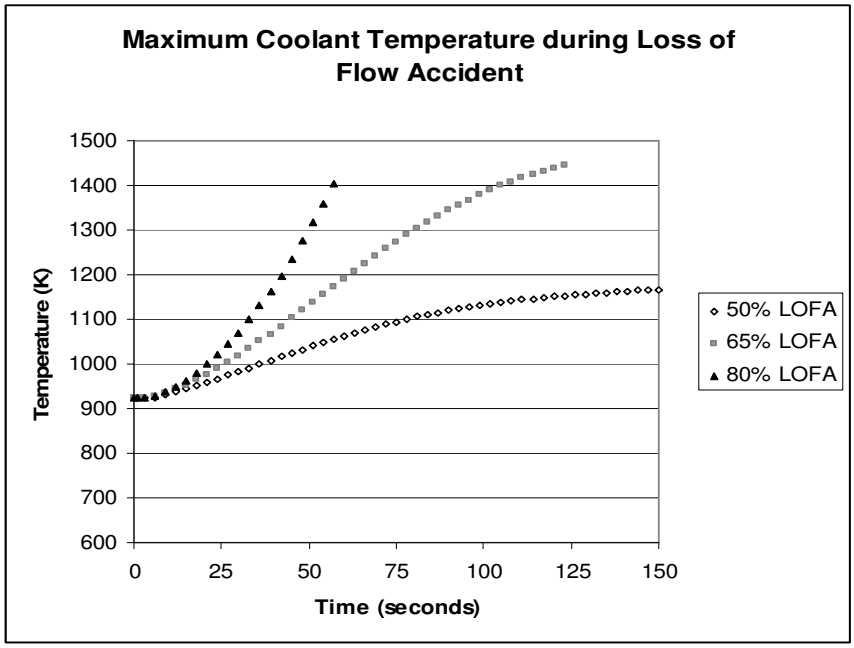

Figure 3: Maximum Coolant Temperature during Loss of Flow Accident at BOL (sodium boiling at 1156 K)

Loss-of-heat-sink-accidents

Simulation of LOHSAs indicate that up to about 33% loss of sodium heat transfer to the heat exchanger can be tolerated before boiling occurs and that even then about a minute is available to detect this accident and turn off the neutron source; as long as heat transfer to the heat exchanger remains above 30% of nominal the decay heat can be removed without damage to the fuel. The detailed results of the LOHSAs simulations are summarized in Table 3.

Table 3: Loss of Heat Sink Accident Summary

	BOL	BOC	EOC
Maximum Heat Sink Loss Before Coolant Boiling	33%	36%	36%
Time Until Coolant Boiling (seconds)	65	70	78
Maximum Heat Sink Loss Before Fuel Melting	47%	53%	54%
Time Until Fuel Melting (seconds)	77	87	86
Maximum Heat Sink Loss for which Decay Heat can be Fully Removed.	70%	70%	70%
Time Until Coolant Boiling for 70% LOHSA (seconds)	10	11	11
Time Until Fuel Melting for 70% LOHSA (seconds)	17	21	22

C. Conclusions

Possible transients occurring in SABR can be placed into two different categories. The first category of transients is accidents affecting SABR's neutron population in the fission core. Due to operation very close to the Troyon Beta Limit, SABR is safe against accidental increases in the plasma ion fueling rate and plasma auxiliary heating. SABR is also safe from any accidental control rod ejections due to the large subcriticality.

The second category of transients is those affecting SABR's heat removal systems---Loss of Flow, Heat Sink and Power Accidents. In all of these accidents, there are at least 10 seconds to respond to an initiating event by turning off the plasma auxiliary heating. The 10 second for 100% loss of flow is probably not enough time to react by turning off the plasma auxiliary heating but this accident is the absolute worst case scenario and does not take into account natural circulation or secondary coolant loop flow coast down times. In more realistic accident scenarios, there are many tens of seconds up to a couple minutes for taking corrective measures before the coolant begins to boil and the fuel begins to melt. This required reaction time is implies the need for careful monitoring of the temperature and power levels in the reacto, but it should be sufficient time for reactor operators to take action. After the plasma is shut down, if the coolant flow rate and heat sink capability continue to decrease, back-up pumps and heat exchangers must be turned on to remove the power produced by decay heat.

Because of the large positive sodium voiding and lack of ^{238}U in the TRU fuel, SABR has a positive reactivity feedback. Due to this positive reactivity feedback and decay heat production, SABR will fail in the absence of external counter measures during severe accidents in the heat removal system. The subcritical nature of the reactor, however, provides a considerable margin of safety for dealing with this positive reactivity feedback during transients. The immediate risk that all accidents pose can be diminished if the fusion neutron source is rapidly shut down, leaving only decay heat to deal with. Because back-up and auxiliary pumps and heat exchangers will be responsible for providing sufficient heat removal in extreme cases, SABR requires further design of the primary, intermediate and secondary coolant loops so that a more in depth analysis can determine if the reactor is in fact safe from the worst case accident scenarios. Further work also should include separate systems dedicated to removing decay heat. However, for all accidents suggested in this study, there are viable options for preventing permanent damage to the reactor that make SABR, with additional design, a potential second generation Advanced Burner Reactor for minimizing the amount of Spent Nuclear Fuel that must be stored in High Level Waste Repositories.

References

1. T. S. Sumner, "Dynamical Safety Analysis of SABR", MS Thesis, Georgia Institute of Technology, 2008.
2. W. M. Stacey, et al., "A TRU-Zr Metal Fuel, Sodium Cooled, Fast Subcritical Advanced Burner Reactor", *Nucl. Technol.*, 162, 53 (2008).
3. J. P. Floyd, et al., "Tokamak Fusion Neutron Source for a Fast Transmutation Reactor", Fusion Sci. Technol., 52, 727 (2007).